PSO4105 Final Report

Biomass Cofiring in Suspension-Fired Power Plants

Contributing Authors:
Søren Lovmand Hvid [1]
Helle Junker [1]
Ejvind Larsen [1]
Stefan Røikjær [1]
Kim Kokholm [1]

Søren Knudsen Kær [2]
Steve Berg [2]

Larry Baxter [3]
Chunyang Wu [3]
Hong Lu [3]

1: Dong Energy
2: Aalborg University
3: Brigham Young University

Prepared	Søren Lovmand Hvid, 21 March 2008
Checked	Helle Junker, 28 April 2008
Accepted	Helle Junker, 28 April 2008
Approved	Helle Junker, 28 April 2008

Doc. no. 362169
Replaces doc. no. 280164
Project no. T013856

Table of Contents

List of Figures

List of Tables

i. Preface

The current project was initiated in 2002 with the objective of developing tools to assist in the successful introduction of a larger biomass share in power production. The modeling environment considered appropriate to address the engineering needs was CFD analysis tools, and a fundamental project priority was therefore to develop CFD models capable of describing coal-biomass co-combustion in suspension fired boilers. In addition, it was envisaged that a less complex tool would be needed for preliminary engineering purposes. This “Engineering model” was to be based on a largely empirical foundation. Unfortunately, the engineering model development had to be aborted and the project focus kept on CFD model development and validation.

Development of modeling tools, based on a mathematical description of the relevant physics and chemistry, has to be based on several levels of investigations ranging from more fundamental laboratory experiments to full scale applications. In the current project, laboratory experiments were carried out to produce datasets of high quality with which to validate CFD models. A progression of projects has been initiated during the past years, which feed into this development strategy. PSO projects 4881 (primarily sub-projects 4805 and 4806) and PSO project 7333, all currently under way, are all formulated directly to further the development strategy, but several other projects contribute to the final objective of the current project. Amongst these are the following PSO projects:

- PSO project 6515 (Dust firing) has generated valuable data in several areas related to combustion of biomass, such as ignition properties, fuel characterization, burn-out data as well as many practical properties relevant to combustion systems.
- PSO project 3149 (NG-Straw co-firing) where combustion tests were carried out in full scale at Fynsværket unit 3 accompanied by CFD analysis
- PSO project 4792 (Biomass Grate Firing – The “Joint Project”) where substantial fundamental CFD validation work has been carried out with relevance to suspension firing as well.

The results and findings of PSO project 4105 as well as other relevant projects are included in the model development carried on in PSO projects 4881 (4805 and 4806) and 7333. These projects contribute to the overall objectives in the following main areas:

- PSO 4805: Investigation of channel formation[1] in a suspension fired boiler experimentally and by use of CFD analysis.
- PSO 4806: Lab-scale investigation of “dual burner head” operation, where coal and biomass (straw) are not mixed but fed individually to the (low-NO_x, swirl stabilized) burner. This project focuses on NO_x formation and destruction mechanisms and burner technology.
- PSO 7333: Full-scale data collection within a co-fired flame, comprising measurements of temperature, gas-phase composition and particle composition. CFD model development and validation.

---

[1] Channel formation is the term used to describe the wake of an individual burner in a burner array, which due to lack of adequate mixing may be persistent throughout the furnace and convective passes of the boiler.

- Several Ph.D.-projects carried out at Brigham Young University, Aalborg University and The Technical University of Denmark with focus both on fundamental aspects of combustion under very controlled conditions as well as laboratory-scale measurements replicable of full-scale systems.

ii. Summary

Background

Biomass co-firing has developed into a biomass utilization technology of considerable scale in Denmark involving boilers of different designs, different fuel types, and use of a variety of technologies such as low-NO_x burners, advanced steam cycles, over-fire air systems, etc. The development of improved modeling tools will allow both better understanding of existing co-firing processes and offers potential improvement of future processes without the need for extensive trial and error approaches.

The modeling tools available for prediction of combustion behavior of pulverized fuels do not adequately cover the characteristics of biomass-derived fuels for suspension combustion. The long-term objective for the R&D activities on co-firing is to develop a modeling tool that allows us to predict all necessary performance information and explore potential problem areas when co-firing different biomass fuels in suspension-fired power plants. The modeling tool should predict combustion behavior such as burn out rates, flame stability, and emission rates. Based on predicted flue gas composition and fuel analysis, corrosion issues should be evaluated, and models for prediction of slagging and fouling should also be included as well as models for prediction of fly ash and bottom ash composition.

Objectives

The objectives of this project are to:

1. Investigate coal-biomass co-firing details on a small pilot scale combustor, including quantitative data collection suited for validation of predictive combustion models
2. Develop and demonstrate CFD-based models that adequately describe the behavior of biomass combustion in a suspension-fired unit.
3. Use the tools developed to demonstrate their ability to assess the performance of a suspension-fired facility.

A major product of this project is an experimentally validated computational fluid dynamics (CFD) based modeling tool adapted to accommodate biomass co-firing combustion features. The CFD tool is able to predict deposit accumulation, particle conversion, fly ash composition, temperatures, velocities, and composition of furnace gases.

Main findings & conclusions

Pilot-scale facilities provide meaningful data for interpreting biomass-coal cofired near-burner conditions on the basis of detailed composition measurements and modeling. This project enhances the understanding of biomass combustion performance in the near-burner region, especially flame structure, major species profiles and NO formation. Spatial concentration profiles of seven gas species, CO, CO_2, O_2, NO, HCN, and NH_3, were collected with intrusive sampling methods using two commercial state-of-the-art analyzers and a specially designed gas sampling probe. Combustion tests included nine separate fuels or fuel blends. Spatial

profiles of major species from biomass cofiring provide detailed indications of flame structure and dynamics. All the tests were conducted under overall fuel-lean conditions.

The experiments provide a database that defines flame structure, chemistry, and aerodynamics for a wide variety of coal and biomass fuels and blends. High- and moderate-sulphur coals (Pittsburg #8 and Blind Canyon) and herbaceous and woody biomass (straw and sawdust) and blends of these fuels form the suite of fuels and blends tested. Advanced instrumentation and other engineering improvements increase experimental efficiency, reducing the time necessary for the completion of one case from several months to less than three weeks.

CFD modeling with commercial software, FLUENT^{TM}, predicts velocity and temperature information. Flow patterns were predicted and analyzed under both cold-flow and hot-flow conditions in the BFR (Burner Flow Reactor). A 3-D CFD model simulates the swirl-generator cold-flow exit velocities. Experimental velocity data under non-reacting conditions collected in the project generally follow the trends from CFD predictions. The predictions immediately following the swirl-generator were adopted to define the inlet for the axisymmetric combustion model. Reacting flow data collected previously in the same reactor compare less favorably with predictions with possible inconsistencies in both. The CFD predictions are more comprehensive and highly resolved for most analyses.

In addition to the axisymmetric species spatial profiles (maps) and CFD predictions, two data analysis methods, stoichiometric ratio maps and 1-D normalized mole fractions, quantify flame structure, major species profiles, and flow dynamics.

Analysis of NO formation is provided through comparison of CO, NO, NH_3, and HCN profiles, supplemented with CHEMKIN calculations.

The major conclusions drawn from this project include:

Low-grade fuel combustion in the swirl-stabilized burner

Under the conditions studied, all low-grade fuel combustion in the swirling flow burner develops a stabilized combustion zone near the inlet followed by a relatively flat reacted-gas zone. Under overall fuel-lean conditions, intrusive measurements reveal the existence of a transient fuel-rich eddies. The existence of an instantaneous fuel-rich region is evident by the detection of HCN/NH_3 and high amounts of CO in the swirling flow region even though the average O_2 concentration is greater than zero. Notably, no region exists in any test in which average O_2 concentrations are zero. The data sets collected are generally repeatable and consistent, and provide excellent validation criteria for future development of comprehensive combustion models.

CFD simulation of low-grade-fuel combustion

Grid-independent, high-order modeling approaches provide reasonable predictions of gas-phase velocity and temperature and have limitations in predicting species. With a proper modeling strategy, the results verify the existence of the reverse flow region close to the inlet under both cold-flow and hot-flow operating conditions. In the wall-confinement region (in the water-cooled quarl), the flow can be predicted with little error. In the swirling-flow, fully developed region, the small shift of the flow axis from the reactor geometric axis can’t be predicted with an axisymmetric code or, in the absence of any asymmetric boundary or inlet conditions, by a fully 3-D code.

Biomass firing and cofiring compared to coal combustion in swirling flows

Predictions show that there are no dramatic qualitative changes in flow patterns in the swirling flow during biomass tests compared to coal test, though details differ. All flows show centerline and corner recirculation zones that stabilize the flame near the burner outlet. However, biomass combustion in swirling flows has an expanded combustion region resulting from more particle penetration and high volatile yield. The small and dry biomass particles (compared to commercial biomass fuels) penetrate the flame further into reactor to complete devolatilization and oxidation. High-volatile yields contribute to the larger and more intense fuel-rich (CO-laden) regions.

NO formation from the cofiring cases

In the gas species 1-D and axisymmetric profiles, NO follows a similar pattern to that of CO_2, indicating that NO formation is more mixing limited than kinetically controlled under the conditions studied. Combustion of sawdust shows significant lower NO production on an energy basis primarily because of its low nitrogen content.

Biomass and coal have different stable NO_x precursors. HCN is the prevailing fuel-NO_x intermediate in coal flames, and NH_3 is predominant in the straw and possibly sawdust flames. The form of nitrogen impacts NO formation mechanisms and emission concentration. Biomass generates more NH_3 and less HCN than coal, and the dominance of NH_3 in biomass combustion increases the amount of fuel-N converted to NO under swirling flow conditions. Kinetic calculations show that NH_3 is more thermally stable than HCN in the combustion region and more reactive within the flame fronts. Both HCN and NH_3 show similar conversion efficiency to NO in the reacted-gas region.

1. Task 1: Generation of fundamental data

The overall objectives of Task 1 are to generate a range of fundamental experimental data that are important to the development and validation of the models and to investigate the influence from cofiring on burner operation (stability, flow patterns etc.)

1.1 Subtask 1.1: Fuel characterization

This research provides, among other things, species composition maps (NO, NO_2, HCN, NH_3, O_2, CO, CO_2, and SO_2) as functions of position during a series of coal, biomass, and coal-biomass cofiring experiments. Both the coal and biomass fuels selected for these experiments exhibit widely differing properties, both within a fuel type and between fuel types. Nevertheless, they represent a small fraction of the potential number of fuel combinations.

Straw is a widely available herbaceous biomass fuel that has relatively high nitrogen content compared with many wood-derived fuels. It is a reasonably representative example of rapidly grown herbaceous material, large quantities of which exist as agricultural residues, with similar materials such as switchgrass proposed as energy crops.

Clean wood biomass has proved to be an ideal candidate for energy production by cofiring in current PC facilities. Sawdust is a common ligneous biomass fuel with low nitrogen content relative to coal and most herbaceous materials, and represents a high-quality wood-based fuel.

In terms of ash management properties during combustion, straw typically exhibits high ash, high alkali, high chlorine, and high silica contents relative to wood. However, wood has high calcium concentrations (as percent of ash). These two fuels cover the range of both fuel types (herbaceous and ligneous) and nitrogen contents likely to be encountered in commercial application.

Two typical commercial coals in the United States, Blind Canyon and Pittsburgh 8, appear in the current cofiring research. Blind Canyon represents a typical low-sulfur, low-moisture, sub bituminous to bituminous coal used principally in the western US. Pittsburgh 8 represents a high-sulfur, low-moisture, high-energy content, low-oxygen, bituminous coal in common use in the Eastern and Midwestern US. These coals span most fuel properties ranges among coals commonly used in US and international power plants.

Table 1 The physical properties of the fuels used in the current project.

	Straw	Sawdust	Blind Canyon	Pittsburgh 8
Ash	7.52	0.39	11.42	9.10
Moisture	5.87	5.46	3.06	1.65
<u>Ultimate analysis (wt %, daf)</u>				
Carbon	44.4	48.9	70.3	83.2
Hydrogen	5.72	6.18	5.46	5.32
Sulfur	0.12	0.11	0.54	2.89
Nitrogen	0.91	0.35	1.54	1.64
Oxygen (difference)	48.9	44.5	22.2	6.95
Heating value (MJ/kg, daf)	15.9	18.0	27.8	31.2
Average particle size (μm)	475	345	70	70

Proximate and ultimate analysis data for the fuels appear in Table 1. Coal and biomass analyses were performed with a LECO CHNS-932 elemental analyzer and oxygen content was obtained by difference, as is customary. All fuels were prepared (milled and size classified) prior to the tests. One consequence is that all contained less moisture when analyzed that would be typical in commercial operations. Both biomass fuels were prepared and shipped from Denmark.

Table 2 reports the proportional feed rate for nine tests using combinations of the four fuels. The high biomass to coal mass ratio, 70:30, represents the upper limit of common commercial biomass cofiring fractions. Measured fuel and air feed rate parameters appear in Table 3. The initial feed rates were measured at stand-by state, that is, without firing any fuel or primary air flow but by metering fuel from the feeder into a weigh cell. The actual feed rate occasionally deviates from these settings for many reasons. The feed rates listed in the table were calculated from a carbon balance based on measured CO, and CO_2 concentrations (on a dry basis) in the exhaust of the reactor rather than the calibrated feeder results as the former is a more accurate measure of feed rate. Unlike the solid fuel feed rates, the measured air flows are robust and accurate, as was verified through the preliminary natural gas combustion tests and by calibration with a traceable flow meter.

Table 2 Experiment layout for the tests with different fuels and their mass ratios.

Test ID	S	70S30BC	50S50BC	BC	SD	70SD30BC	70SD30P	70S30P	P
Straw	1	0.7	0.5					0.7	
Sawdust					1	0.7	0.7		
Blind Canyon		0.3	0.5	1		0.3			
Pittsburgh 8							0.3	0.3	1

Table 3 The set-up feed rate of fuel and air flow rates under the test conditions.

Test ID	Biomass feed rate (kg/hr)	Coal feed rate (kg/hr)	Primary air feed rate (kg/hr)	Secondary air feed rate (kg/hr)	Ratio of primary to secondary feed rates	Equivalence ratio
S	20.74		15	150	0.100	0.64
70S30BC	14.7	6.55	8	145	0.055	0.89
50S50BC	10	10	8	153	0.052	0.90
BC		12.3	11	140	0.079	0.77
SD	19.7		7.3	115	0.063	0.90
70SD30BC	15.6	6.55	15	150	0.100	0.90
70SD30P	15.6	6.47	15	135	0.111	0.92
70S30P	14.7	6.47	15	135	0.111	0.93
P		12	15.4	115	0.134	0.92

The fuel particle size distributions in this project appear in Figure 1, as measured using a Coulter Counter. Straw has the largest average particle size (475 micron), larger than that of sawdust (370 micron). These values are much smaller than commercial fuels, which are on the order of several millimeters or even centimeters in the longest dimension. Both coals considered have an average particle size of 70 micron.

Several other particle properties relevant to this investigation appear in Table 4. Many of these deal with chemical reactivity issues and are important primarily for modeling purposes while others represent important physical or chemical differences independent of model predictions. For example, sawdust has a volatile content of 95% (mass basis), which is slightly higher than that of straw (90%), Pittsburgh 8 (60%) and Blind Canyon coal (50%). Wood generally has a slightly higher volatile content than herbaceous materials, and both are much higher than coal. These differences play a role in the overall NO_x formation and other aspects of this project, as discussed below. The devolatilization, heterogeneous reaction, and overall burning kinetics come mainly from separate investigations, most significantly from the PhD work of Hong Lu (Lu, 2006) that proceeded in parallel with this investigation. His work demonstrates a pronounced impact of particle shape and size on overall conversion time: effects either ignored or only partially incorporated in current computational fluid dynamics codes.

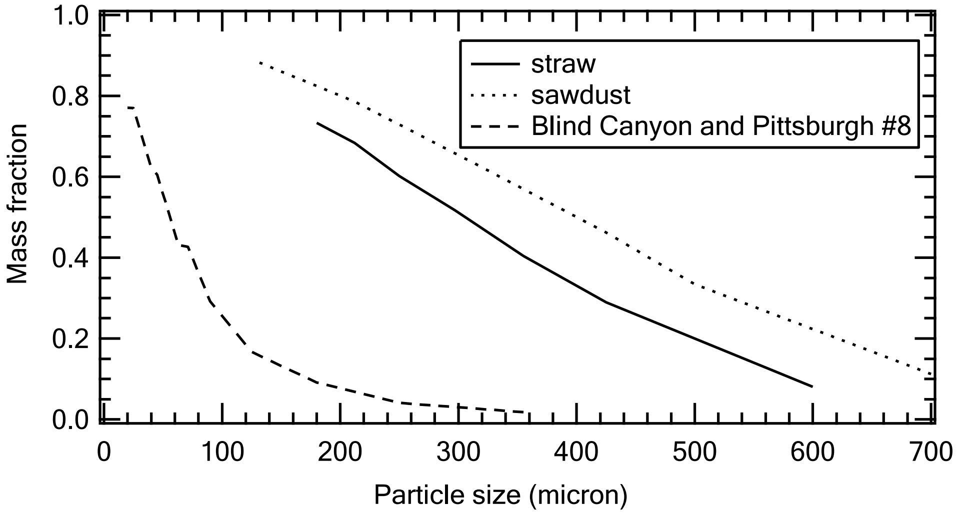

Figure 1 Fuel particle size distributions used in this investigation.

These fuel properties differ from those in commercial systems in a few systematic ways. The fuel preparation occurred long before combustion and lead to drier, smaller, and more uniformly sized biomass fuels than would be the case in most commercial cofiring applications. The straw chlorine and alkali contents, while higher than those of coal, were low compared to typical straws from either Denmark or the US, largely because of a wet growing season in Denmark. The biomass particle aspect ratios are both smaller and more uniform than is typical for commercial operation, mainly because of the careful preparation procedures. However, the biomass particles are still far from spherical. The experiments using these fuels occur in a relatively large laboratory facility, but it is still small compared to commercial facilities, requiring the particle sizes and moisture contents to decrease to generate realistic flames.

Some of these model parameters are largely irrelevant for biomass particles. For example, the heterogeneous char combustion kinetics have no significant influence on the predicted particle burning rates. Biomass char particles generally are so large that they burn under diffusion-controlled conditions. In these experiments, even the coal char combustion is substantially diffusion controlled.

Table 4 Parameters selected and inputs in the combustion modeling.

	Blind Canyon	Pittsburgh 8	Straw	Sawdust
Rosin Rammler particle size distribution				
Spread parameter	1.14	1.14	2.76	1.19
d_{min} (μm)	20	20	120	160
d_{max} (μm)	350	350	720	650
$d_{average}$ (μm)	70	70	475	370
Shape factor	1	1	0.2	0.2
Density (kg/m^3)	1300	1300	700	700
Thermal conductivity (W/m K)	0.0454	0.0454	0.0454	0.0454
Latent heat	0	0	0	0
Vaporization temperature (K)	300	300	300	300
Volatile fraction (%)	50	40	90	95
Binary diffusivity (m/s^2)	0.0005	0.0005	0.0005	0.0005
Particle emissivity	0.8	0.8	0.8	0.8
Particle scattering factor	0.6	0.6	0.6	0.6
Linear swelling coefficient	1.1	1.1	0.56	0.56
Burnout stoichiometric ratio (%)	1.33	1.33	2.67	2.67
Combustion fraction	50	60	10	5
CPD model parameters				
P_0	0.49	0.62	1	1
C_0	0	0	0.15	0.15
$\sigma+1$	5.1	4.5	3	3
Mw_{c1}	36	24	81	81
Mw_s	359	294	22.67	22.67
Mass diffusion-limited rate constant	5.00E-12	5.00E-12	5.00E-12	5.00E-12
pre-exponential factor	0.917	0.917	0.917	0.917
Activation energy (J/kg-mol)	1.08e8	1.08e8	1.08e8	1.08e8

The biomass properties give rise to commercially important behaviors that are quite complex. NO_x emission is one example. A detailed chemical kinetic analysis shows that the NO intermediates dominantly generated during biomass combustion (mostly NH_3) are more thermally stable at temperatures up to about 1800 K than are those generated during coal combustion (mostly HCN). The oxidation kinetics of both species are very similar. This could lead to higher NO generation efficiency and hence higher NO from biomass than from coal. However, the larger volatile release from biomass creates a larger fuel-rich region in the combustor where NO formation is suppressed and NO destruction is enhanced. This could lead to lower NO generation during biomass combustion than during coal combustion for a given amount of intermediate. These opposite trends combine with complex aerodynamics/mixing, temperature histories, and kinetics to yield overall NO conversions that may be either higher or lower during cofiring than one would expect based on fuel nitrogen content of the two fuels alone.

Effluent NO emissions illustrate the complex nature of NO formation in these tests. The most relevant fuel properties of several fuel blends investigated experimentally appear in Table 5. Combustion tests for each of these coal-biomass blends produced both detailed species composition maps and effluent NO concentrations. Figure 2 compares the experimentally measured effluent NO concentrations with those predicted based on interpolating between the measured values for the pure components of the blends. If the measured and interpolated values are the same, blending leads to no non-linear interaction in the NO formation between the fuels. To the extent they are not the same, NO emissions either increase or decrease relative to what would be expected based on pure fuel compositions. As is seen, both increased and decreased NO formation occurs, primarily because of complexities such as those mentioned above. However, lower NO than anticipated occurs more often than higher NO. It is also certain that aerodynamic/mixing, heat loss, and other effects can profoundly affect these results.

The general conclusions regarding fuel properties and their implications on cofiring are:

1. Biomass generally is less spherical, larger, more moist, less dense, and has lower heating value than coal
2. Biomass generally produces more volatiles and shrinks significantly more during devolatilization than coal (coal actually slightly swells)
3. Biomass chars commonly burn at diffusion-controlled rates compared to coals, where reaction kinetics sometimes influences burning rates. However, diffusion-controlled burning rates depend significantly on particle size and shape even though they do not depend on heterogeneous kinetic reaction rate parameters.
4. Biomass fuels generally produce more NH_3 and less HCN than do coals, with these differences leading to generally higher fuel-N to NO conversion efficiencies, all else being equal. However, all else is rarely equal when comparing biomass and coal combustion. While conversion efficiencies are commonly higher for biomass fuels, actual NO concentrations may be either higher or lower, depending on mixing, temperature, and other issues. Therefore, overall NO formation during biomass and biomass-coal cofiring may be higher or lower than during coal combustion, though a well operated system more commonly leads to lower rather than higher NO.

Table 5 Composition and thermal properties inputs during the cofiring PDF calculations.

	50S50BC	70S30BC	70SD30BC	70S30P	70SD30P
Element mole fraction (daf)					
C	0.376	0.343	0.355	0.368	0.380
H	0.441	0.447	0.459	0.443	0.455
N	0.007	0.006	0.004	0.006	0.004
O	0.177	0.204	0.182	0.183	0.161
Net calorific value (MJ/kg)	21.8	19.4	20.9	20.6	22.1
Heat capacity (J/kg K)	1100	1100	1100	1100	1100

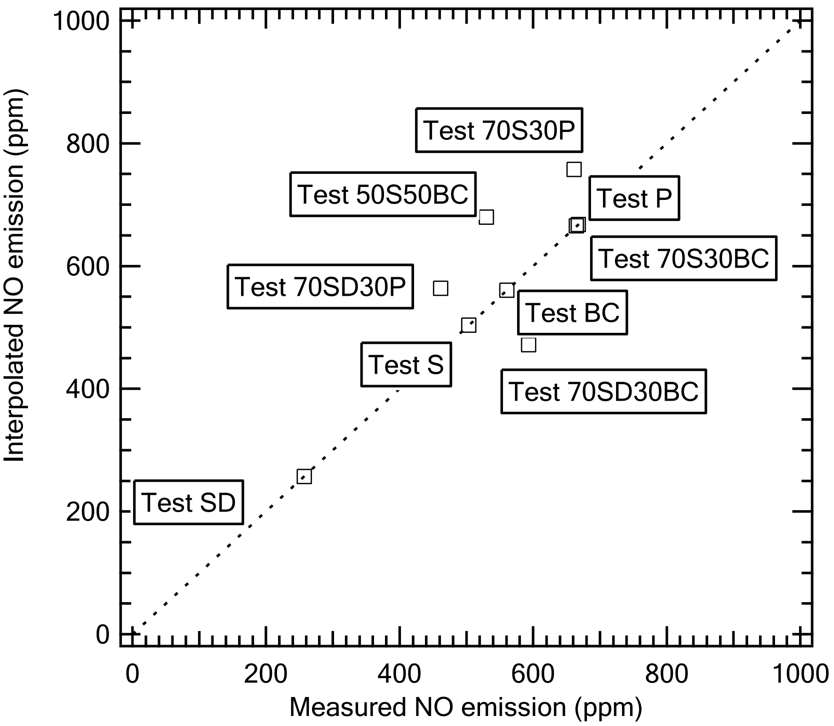

Figure 2 The relation between the measured and the interpolated NO emissions (mole fraction on a 3% excess O_2 basis) in the present project.

The analysis above describes how well biomass NO emissions from cofired fuels relate to those of the pure components of the blend. A separate question is how biomass NO formation relates to coal NO formation, or more to the point, whether biomass fuels convert fuel nitrogen more or less efficiently to NO compared to coals. Since biomass produces more NH_3 and less HCN than does coal, and since the thermal stabilities of these intermediates differ (though the oxidation reaction kinetics and NO yields are similar), there exists the potential for different nitrogen to NO conversion efficiencies. This discussion involves three NO-related parameters. The effluent NO emissions, the effluent NO emissions per unit fuel energy, and the conversion efficiency of fuel nitrogen to NO. These terms are first mathematically defined, followed by a discussion of the results.

NO emissions on an energy basis can be defined based on NO molar/volumetric concentrations as follows

$$Y'_{NO} = \frac{N_{NO} MW_{NO}}{\sum M_i H_i} \qquad \textbf{Eqn 1.1}$$

where N_{NO} is the molar flux of NO (mol/hr) at the exhaust, as calculated from:

$$N_{NO} = [(\sum M_i + M_{air})/MW_{mixture}]y_{NO,exhaust} \qquad \textbf{Eqn 1.2}$$

where the symbols are defined as follows:

M_i and M_{air}: the feed rates (kg/hr) of fuel i and air, respectively;

H_i : the lower heating value (as received; MJ/kg) of fuel i ;

$MW_{mixture}$ and MW_{NO} : the molecular weight of exhaust gas mixture (assumed to be 29 g/mol) and NO, respectively.

$y_{NO,exhaust}$: the measured exhaust NO volume fractions;

Y'_{NO} : the amount of NO produced per unit energy of fuel, a more meaningful number from an environmental performance standpoint than the amount of NO produced per unit of flue gas produced, especially when fuel heating values vary as widely as is the case between coal and biomass.

The last term is defined as

$$Y''_{NO} = \frac{Y'_{NO}}{\sum M_i x_{N,i}} \qquad \textbf{Eqn 1.3}$$

where $x_{N,i}$ is the nitrogen mass fraction of fuel i . This parameter represents the amount of NO produced per unit nitrogen in the fuel. Assuming all NO is generated from fuel nitrogen, which is approximately correct for essentially all nitrogen-containing solid fuels, larger values of this parameter indicate greater fuel nitrogen conversion per unit heat produced.

The normalized emissions of all the tests appear in Table 6. The table shows that Pittsburgh 8 has the highest value of $Y_{NO,3\%O_2}$ (668 ppm), higher than straw (561 ppm), which is higher than that of Blind Canyon (504 ppm). Sawdust has the lowest fuel-N content (0.35%, wt, daf) and shows the lowest NO emissions (257 ppm). Cofiring biomass with coal does not necessarily reduce NO emissions on the 3% excess O_2 basis (the basis sometimes used by EPA, among others, for regulations). Two straw cofiring cases, Test 70S30BC and Test 70S30P, show a high $Y_{NO,3\%O_2}$ (665 and 661 ppm, respectively) close to that of pure Pittsburgh 8. Cofiring sawdust with Blind Canyon also increases NO emission compared to that from the pure coal test. Only Test 50S50BC and Test 70SD30P demonstrate a reduction in NO emission compared to the respective pure coal tests.

Table 6 NO emissions in the reacted-gas region during current project

Test ID	$Y_{NO,3\%O_2}$ (ppm)	Y'_{NO} (10^{-2} kg/MJ)	Y''_{NO} (10^{-2} kgNO/MJ/kgN)
S	561	4.07	2.47
70S30BC	664	3.89	1.91
70S30P	661	4.16	1.97
50S50BC	530	2.79	1.32
SD	257	1.47	2.26
70SD70P	461	2.51	1.72
70SD30BC	593	3.13	2.27
P	668	4.44	2.52
BC	504	3.32	2.04

Resulting NO emissions on an energy basis indicate that sawdust is once again the lowest NO emitter (1.47e-2 kg/MJ), with its Y'_{NO} less than one half that of other fuels, and its cofiring cases with Pittsburgh 8 drops the emission level by nearly 50%, and a decrease of 18% was achieved when cofiring with Blind Canyon. Because of the relatively high fuel-N content, straw shows a high NO emission close to Pittsburgh 8 and higher than Blind Canyon, and its cofiring cases studied can only achieve a reduction of around 25% (Test 50S50BC) at most.

In the higher mass fraction cofiring test with Blind Canyon, NO emission (3.89 e-2 kg/MJ, Test 70S30BC) is even higher than the pure coal test (3.32e-2 kg/MJ).

With respect to yield (Y''_{NO}), the pure biomass tests have the highest NO yields, followed by the pure coal tests, and cofiring can effectively reduce NO emissions. For example, Test 50S50BC has a nearly 40% reduction of NO yields compared to that of Test S on this basis. All cofiring tests were found have lower Y''_{NO} values than their respective pure fuels tests, and this reveals that cofiring can be a potentially feasible method to reduce NO yields on bases of both energy and fuel-N input.

These data show the complexity associated with NO emissions. For example, sawdust produced about half as much NO as the next lowest pure-fuel NO emitter as measured by concentration in the flue gas normalized for dilution. If normalized by fuel heating value, sawdust is still the lowest emitter. When NO per unit energy per unit fuel nitrogen content is considered, sawdust is among the highest emitters of NO. The biomass fuels generally have higher nitrogen conversion efficiencies to NO than coal, regardless of whether the actual NO concentrations are relatively high (straw) or low (sawdust). However, fuel properties alone don’t account for all of the variation, as indicated by comparing the interpolated vs. measured values for the blends.

1.2 Subtask 1.2: Generation of Pilot Data

The objective for this subtask is to establish fundamental understanding of the combustion and deposition behavior during biomass cofiring using the Burner Flow Reactor at BYU and to generate validation data for the sub models describing fuel reaction, flue gas composition as well as deposit formation rates and composition.

Deliverables from this subtask include a unique and comprehensive set of experimental data that will be used for sub model development and validation. The data obtained in the burner flow reactor will develop insight useful in producing both of the models as well as provide valuable information for comparison with the models. The burner flow data will also provide a data set demonstrating trends that will be used for burner design (in Subtask 4.1). Thus, a major issue in this subtask is to design, fabricate, and test additional burner(s) to be used in the burner flow reactor. This new burner should be capable of co-firing coal and biomass and methane and biomass. Part of this task includes coordinating the design with cold flow testing to be done in Denmark.

Swirling flow combustion is widely applied in power generation industry for its sustained operation stability and optimal NO_x emission reduction performance. It has been a subject of intensive experimental and numerical modeling investigations (Zhang & Nieh, 2000). The ultimate purpose of swirling flow combustion research is to provide optimal burner design to minimize NO_x emissions with high combustion efficiency (Widmann, Charagundla, & Presser, 1999).

Fuel-NO_x accounts for over 90% of the NO_x formed during low-grade fuels (coal and biomass) combustion in industrial facilities (Pershing and Wendt 1977) (Dayton 2002). Most work in the past on gas-phase fuel-nitrogen conversion has focused on HCN and NH_3, since they are the dominant NO_x precursors in combustion facilities.

The formation of NOx precursors are found possibly dependent on the forms of nitrogen in the parent fuels through laboratory experiments. Devolatilization of bituminous coals produces mainly HCN, while more NH_3 evolves from lower rank coals and biomass (Leppalahti 1995). This is because the fuel-nitrogen in coal exists in the form of unsaturated cyclic nitrogen compounds (Nelson, Buchley and Kelly 1992). Biomass nitrogen resides dominantly in acyclic molecules such as derivatives of amine, amide, and amino acids (Marschner 1990). Based on the bond analysis between the possible nitrogenous products and the compounds in the parent fuels, NH_3 should be dominant precursors during biomass combustion (Wu 2006).

Comprehensive experiment data sets of major gas species profiles are necessary for the understanding of the influence of flow dynamics on the gas phase chemistry, and provide evaluation of comprehensive swirling flow combustion models. Because of the difference of research nature of most previous pulverized fuel experimental study, these complete data sets are very limited for biomass (Ballester, et al. 2005). There has been no report of HCN and NH_3 data sets in the near-burner region from co-firing tests. The current project is aimed at providing profiles of HCN and NH_3 from swirling flow biomass co-firing tests and analyzing the possible difference in the reactivity between HCN and NH_3 with kinetics calculations.

1.2.1 Experimental Facilities

The following sections describe the experimental facility and operating conditions used to obtain experimental data of co-fired coal and straw.

Reactor

The Burner Flow Reactor (BFR) is an axisymmetric, 0.2 MW, pulverized fuel, vertical-fired reactor distinguished by its swirling flow.

As depicted in Figure 3 (illustration from (Tree and Clark 2000)), fuel and primary air flow through the primary inlet, and secondary air passes through a swirl-generator before entering the reactor. Each of six sections of the BFR is 40 cm in height with an internal diameter of 75 cm, minimizing the wall confinement on the flame. With a total height of 240 cm, the BFR simulates the operation of one burner region of full-size boilers.

The optical windows in each section extend nearly the full height of the section for fine resolution of flame in the axial direction, providing ample accessibility for use of non-intrusive/intrusive diagnostic probes, visual observation, and photography (Tree and Clark 2000).

Gas sampling apparatus

HCN and NH_3 were measured with an online-FT-IR analyzer, which also measures CO, CO_2, and NO. Under current experimental settings, the analyzer has a minimum detection limit of NH_3 of about 2 ppm, and HCN of 0.5 ppm. NH_3 measurements are calibrated with NIST-traceable calibration gas samples, while the HCN calibration relies on a theoretical spectra database provided with the analyzer.

A separate online gas analyzer continuously quantifies O_2 (galvanic cell), NO (chemiluminescence), CO (ND-IR), and CO_2 (ND-IR). This analyzer has a built-in pump with a constant operating output (0.4 L/min), acting as the drawing of the gas samples.

HCN and NH_3 are extremely soluble in water at room temperature. Diluting its gas mixture with inert species can lower the condensing point of steam. A nitrogen-quenched, water-cooled gas-sampling probe was designed and constructed for the current project. During measurements of HCN and NH_3, the diluting N_2 flow rate through the sampling probe was set at 0.3 L/min to prevent steam from condensing.

A heated gas path was included in the sampling system. The line comprises stainless steel tubing wrapped with heating tapes, with a temperature above 100 °C.

A cyclone was designed and built into the sampling system to separate larger particles from the main gas flow. A fine particle filter downstream further cleans the sample.

At the sample end of the probe, an optical port in the particle collection cup provided confirmation that steam did not condense. If water appeared in the cups, sampling was terminated and adjustments were made such as changing the cooling water flow rate or increasing the N_2 flow rate.

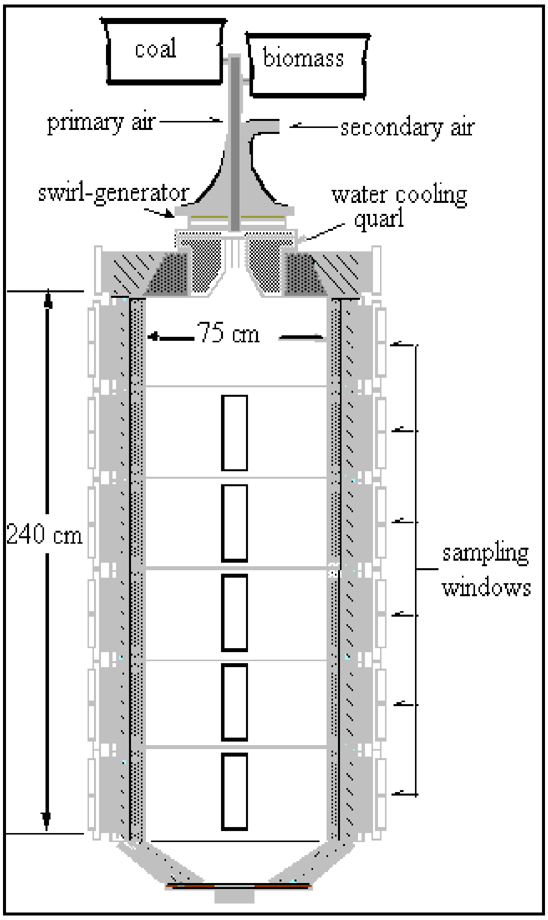

Figure 3. Burner Flow Reactor.

1.2.2 Fuels and Operating Conditions

Straw is a widely available herbaceous biomass fuel that has relatively high nitrogen content compared with many wood-derived fuels. Blind Canyon represents a typical low-sulphur, low-moisture, high-energy content, sub bituminous to bituminous coal used principally in the western US. The fuel properties are listed in Table 7. All fuels were prepared (milled and size classified) prior to the tests. All tests in this project involve blended fuels fed through a single fuel inlet, although separate hoppers metered the fuels with variable speed augers.

All tests were operated under fuel-lean conditions with a swirl number of 1.0. The high biomass to coal mass ratio, 70:30, in co-firing tests represents the upper limit of common commercial biomass co-firing fractions. Calibrated fuel and air feeding rate parameters listed in Table 8, which were calculated from a carbon balance based on measured O_2, CO, and CO_2 concentrations in the exhaust of the reactor.

Table 7 Fuel physical properties

	Straw	Blind Canyon
Ash	7.52	11.42
Moisture	5.87	3.06
Carbon *(wt %, daf)*	44.39	70.25
Hydrogen *(wt %, daf)*	5.72	5.46
Sulphur *(wt %, daf)*	0.12	0.54
Nitrogen *(wt %, daf)*	0.91	1.54
Oxygen (difference) *(wt %, daf)*	48.86	22.21
Heating value (kJ/kg, daf)	15.93	27.78
Average particle size (µm)	475	70

Table 8 The set-up feeding rate of fuel and air flow rates under the test conditions

Test ID	Biomass feed rate (kg/hr)	Coal feed rate (kg/hr)	Primary air feed rate (kg/hr)	Secondary air feed rate (kg/hr)	Ratio of primary to secondary feed rates	Equivalence ratio
S	20.74		15	150	0.100	0.64
70S30BC	14.7	6.55	8	145	0.055	0.89
50S50BC	10	10	8	153	0.052	0.90
BC		12.3	11	140	0.079	0.77
SD	19.7		7.3	115	0.063	0.90
70SD30BC	15.6	6.55	15	150	0.100	0.90
70SD30P	15.6	6.47	15	135	0.111	0.92
70S30P	14.7	6.47	15	135	0.111	0.93
P		12	15.4	115	0.134	0.92

1.2.3 Results and Discussion

Most of the gas species measurements used what are now standard procedures in our laboratory and are documented in published literature and in the dissertation work of Chunyang Wu (Wu 2006). A few of the species deserve special mention here.

Consistency between the two analyzers

As mentioned elsewhere, four species, CO, CO_2, SO_2, and NO, were measured with both the Horiba and MKS analyzers. O_2 can only be measured with the Horiba analyzer, and HCN and NH_3 are solely quantified by the MKS analyzer. Measurement consistency based on the species common to both analyzers provides indication of data reliability, as discussed below.

Data from four species measured by both analyzers (SO_2, CO, CO_2, and NO) from three tests (one test in the case of SO_2) appear below, including one pure coal test (Blind Canyon), one cofiring test (70% sawdust 30% Blind Canyon), and one pure biomass test (sawdust). These data sets illustrate consistency and precision of the measurements. All measurements were calibrated with NIST-certified standard gases prior to each test for the Horiba analyzer, providing some assurance of accuracy and mitigating against systematic analyzer errors. Figure 4 and Figure 5 compare the results of the two independent analyzers over broad ranges of composition.

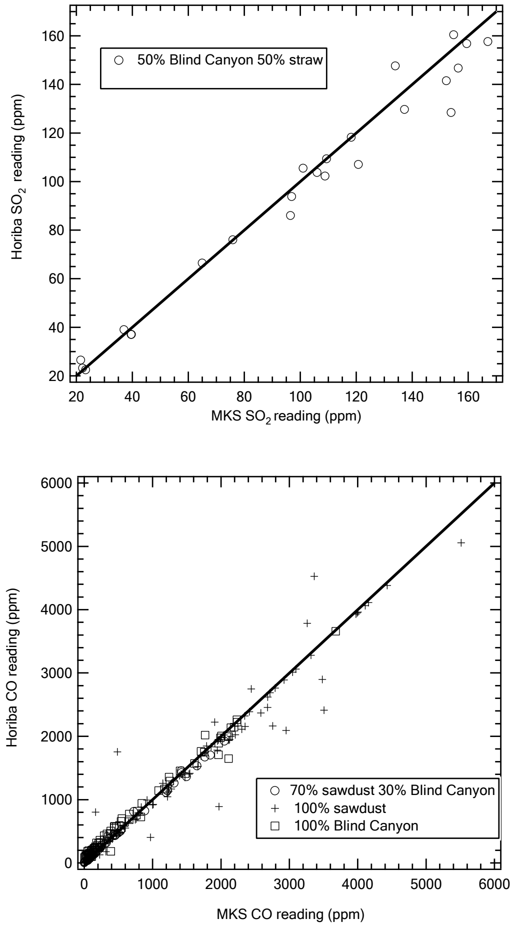

Figure 4 Comparison of the real-time reading at the same position by the Horiba and MKS analyzers: SO2 and CO2, during one cofiring case only (50% straw 50% Blind Canyon)and three cases (straw, Blind Canyon, and 70% straw 30% Blind Canyon), respectively.

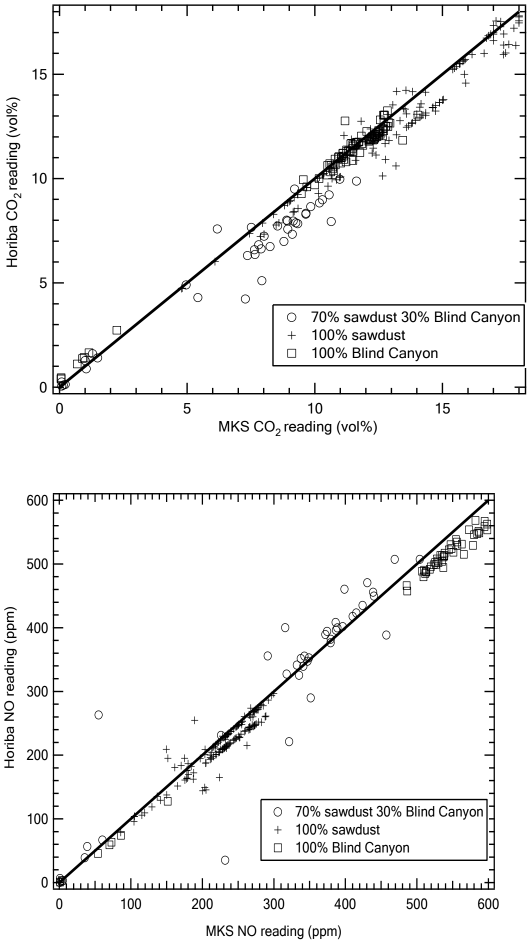

Figure 5 Comparison of the real-time reading at the same position by the Horiba and MKS analyzers: CO and NO during three cases (straw, Blind Canyon, and 70% straw 30% Blind Canyon).

Among the four species measured by both analyzers, SO_2 has the longest response time (five minutes). Collecting these data with both instruments strained the limited amount of fuel available to get a full species map. Therefore, only one cofiring case (50% straw 50% Blind Canyon) includes complete datasets from both analyzers for SO_2. The correlation coefficient for the SO_2 data is 0.988.

CO has shortest response time in both devices among all the gas species. The CO readings from both analyzers match better than the other species, with correlation coefficients in Tests BC, 70SD30BC, and SD of 0.998, 0.995, and 0.981, respectively.

CO_2 and NO require longer response times than CO. In this configuration, the CO_2 data show better agreement (correlation coefficient: 0.986) than those of NO (0.961), which might be due to the differences in quantification techniques. The Horiba analyzer uses NDIR (non-dispersive infrared) spectroscopy to measure CO_2, while an FTIR spectrometer (a dispersive instrument) provides raw data for the MKS analyzer. The two methods share some wave-lengths for some samples, but the signal collection and analysis methodology differ. As for NO, the technical difference is much larger than for CO_2 between the two analyzers. The Horiba instrument uses chemical conversion followed by chemiluminescence to determine NO:

NO is converted to NO_2, and the latter reaches an excited state before releasing electrons, which causes luminescence that is used to quantify the NO. This technique differs radically from the FTIR spectroscopy technique used by the MKS instrument. As shown in Figure 5, bias exists and sometimes can be extreme for a few points among the NO results. However, most data demonstrate a reasonable consistency during the tests.

With respect to data from tests from different fuel combinations, the pure coal data compare most closely. As the fraction of biomass increases, the agreement between the two devices decreases, as shown in the figures. This might result from the sampling probe plugging with biomass particles, since the average biomass particle size is about six times larger than coal. Both analyzers have a requirement of constant sampling flow rate, and a partially plugged sample path impacts the flow rate.

Despite these inconsistencies, the data from both devices show satisfactory consistency. Data from both analyzers appear in the remaining analyses and discussion except for O_2, H_2O, HCN, and NH_3, which are only measured by one analyzer (Horiba for O_2 and MKS for the remaining species).

Description of the gas species profiles

This section discusses the pure Blind Canyon coal test (Test BC) data relative to CFD predictions. These verified species maps are compared with those from pure biomass tests (Test S and Test SD), and from cofiring tests. The data illustrate differences in the major gas axisymmetric maps associated with larger particle size and higher volatile yield and their impacts on the swirling flow region. Because there was not enough Pittsburgh #8 for entire map, only measurements from two axial distances (40 cm and 160 cm) appear.

The gas species concentrations measurements appear in two-dimensional contours, and this added difficulty in comparing the fate of each species through the reactor between different tests. Therefore, alternative analysis methods that more clearly indicate trends are discussed in Section 1.2.4. This section focuses on the species two-dimensional profiles.

Benchmark: pure coal test (Test BC)

The Blind Canyon test provides important benchmark information for comparison when biomass is added. Especially, the replication and characteristics of the axisymmetric spatial gas species profiles, including CO, CO_2, O_2, and NO, indicate the repeatability and general structure of swirl-stabilized flames. CFD predictions of axial velocity, gas flow temperature, and species concentrations (CO, O_2, and CO_2) supplement the experimental data. The discussion involving NO and its intermediates (NH_3 and HCN) appears in Section 1.2.4 below.

Results from two BC tests under the same operating conditions (Figure 6) illustrate data repeatability. The major gas species mole fraction data contour maps appear as a function of radial and axial position. The data represent results from a vertical slice of the reactor passing through its geometric centerline and including both radial directions from this nominally axisymmetric centerline. In the maps, a high contour density represents regions of steep mole fraction gradient, indicating a reaction-dominant region or combustion zone or, less commonly, a region of rapid mixing. This zone expands vertically from the inlet to about 40 cm (within the top reactor section) and horizontally to nearly one-half of the reactor radius (20 cm). The regions with few contours denote the relatively flat profiles for each species, and this is where product gas species (mainly CO_2, NO, and H_2O) dominate, or the reacted-gas zone. Independently sampled maps of the species appear for each of the two tests, respectively. A general description of each species appears as below, followed by a discussion of the repeatability.

The symmetry of the data around the centerline is one test of data quality. As seen, all data exhibit a reasonably well-defined symmetry axis, but this axis deviates a few centimeters from the geometric center of the reactor. Given the size of the reactor and the complexity of the flow, this slightly offset symmetry axis represents a minor aberration in the results.

Another measure of data quality is consistency: regions of high CO are always accompanied by low CO_2, low NO, and high O_2 concentrations in each test. The reaction region for all species maps indicates consistent flame location and structure. In the reaction region, the shapes of each species contour resemble each other, confirming repeatability. Generally, across the reacted gas region, mole fractions for CO_2, CO and O_2 match within 10% when comparing the replicated tests. NO mole fraction contours show much larger differences (±30%) than those for the other species in the reacted-gas regions: one with a peak value nearly 400 ppm, and the other 600 ppm.

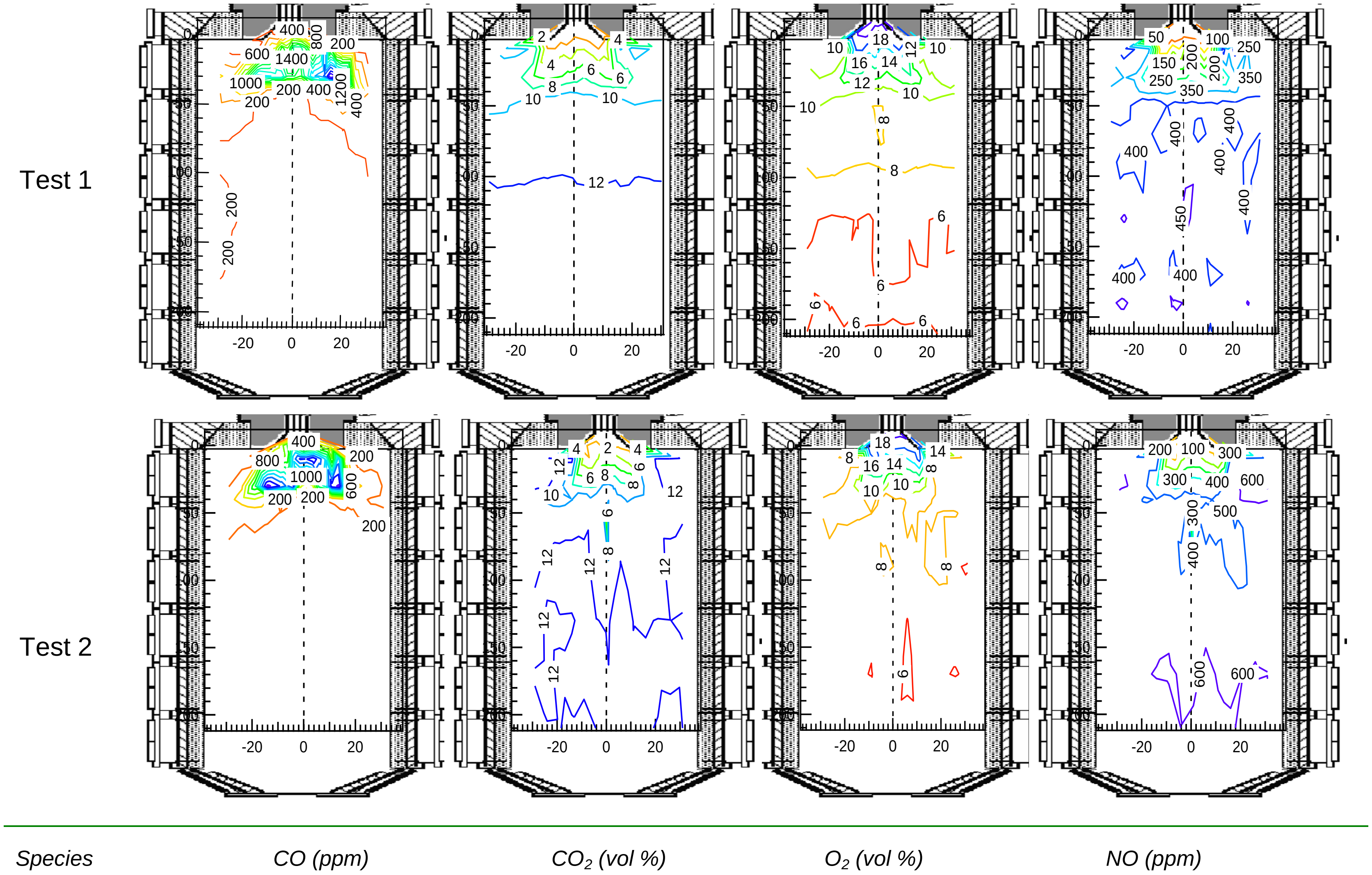

Figure 6 Comparison of major species contours from two Blind Canyon tests under same operating conditions. Both fuel and air entries locate at the top of the reactor, and the radial location unit is cm.

Figure 7 illustrates predicted contours of streamlines, reverse-flow, temperature and major species (O2, CO, and CO2) simulating Test BC. As shown by the closed streamlines, both the internal recirculating zone (IRZ) and external recirculating zone (ERZ) are predicted by the current model. The IRZ extends within the top 80 cm vertically (within the top two section of the BFR) with a horizontal radius of nearly 15 cm. The colored region represents the axial velocity towards the inlet (top). The strongest backflow region locates near the axis right below the cooling-water quarl. Predictions of temperature and three gas species (O2, CO, and CO2) display a high gradient region in the reactor top section (from 0 to 40 cm).

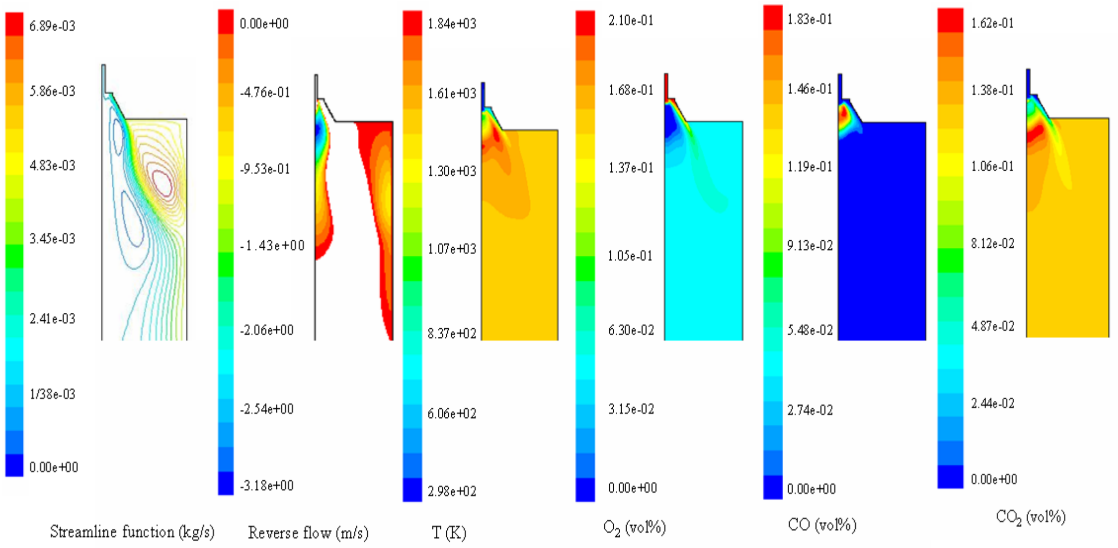

Figure 7 CFD prediction contours of streamline functions, axial velocity, reverse flow, gas-phase temperature, and major species (O2, CO, and CO2) volume fractions from simulation of Test BC in the BFR.

When compared with the axisymmetric maps (Figure 6), the CFD simulations under-predict the combustion region size. Furthermore, the predicted O_2-depleted region is not reflected in the data, and the predicted CO_2 peak isn't found in the corresponding axisymmetric maps. The difference between CFD simulations and experimental data could be attributed to the following factors.

The relatively simple combustion model used here solves species profiles with an equilibrium-based mixture fraction approach, which is based on the assumption that the process is mixing-limited. This method has internal limitations in accurately simulating gas species profiles involved in turbulence chemistry under swirling-flow, low-grade fuel combustion conditions. Specifically, such techniques cannot predict kinetically impacted profiles such as CO.

The particle injection velocity was assumed to be independent of size. However, larger particles react more slowly to accelerating/decelerating carrying gases, potentially creating size-dependent velocities and changing positions where reactions initiate and continue.

The predictions assume a steady-state flame profile. In reality, the flame moves rapidly from place to place, leaving fluctuating fuel-rich and fuel-lean eddies in most regions of the reactor. While the pdf chemistry model used in these predictions incorporates some of this influence, its inability to accurately describe turbulence-chemistry interactions is a well-recognized limitation of CFD.

The point-measurement adopted in the current project represents the best method for collecting species data in the BFR. However, it is not without limitations. Specifically, this intrusive sampling method in the swirling flow environment unavoidably influences the aerodynamics of the sampled region in recirculating flows. The boundary of the combustion region, which is rich with incomplete combustion species such as CO and radicals, represents a delicate fluid dynamic balance between competing momentum and pressure forces that the sampling probe inevitably disrupts.

The predicted oxygen-depleted region nearly overlaps with the IRZ core. Counter-intuitively, the O_2 reading in this region is high (from 8% to 18%, mole percent, Test BC, shown in Figure 6) rather than being close to zero as would be expected for a fuel-rich environment, and this is consistent with data from the same reactor during the Black Thunder coal combustion with swirl numbers ranging from 0 to 1.5 in the reburning project (Tree 2002) and during straw firing/cofiring tests under a swirl number of 2.3 (Damstedt, et al. 2005). This suggests a conceptually different model of near-burner flame structure than commonly appears in the literature. These data suggest that there is no region in this flame that is always under reducing conditions (always has an oxygen content of zero). Rather, a dispersed flame consisting of fuel-rich, presumably particle laden eddies separated by fuel lean eddies permeates the entire near burner region, with any individual location witnessing transient variation between the rich and lean eddies. The turbulent flow near the inlet and in regions of high composition and velocity gradients should lead to wildly fluctuating gas-phase species concentrations at each measurement point. However, the measurement is the time-average of each species within the probe diagnostic volume. Presumably the fuel-rich core would eventually form if the equivalence ratio becomes high enough, but over the broad range of equivalence ratios examined here (0.64-0.93), no case generated a consistently fuel-rich core. It is not clear if this is a feature of this particular burner or if it is a common phenomenon.

Isokinetic sampling under such widely fluctuating conditions is not possible. Non-isokinetic sampling of gases, unlike particles, leads only to changes in the size and local location of the diagnostic volume, not to systematic biasing of the measurements. Currently there exists no other method with the same accuracy, efficiency, or flexibility as the intrusive measurement techniques used in this project for gas composition in such particle-and soot-laden, larger-scale flows. The probe likely quenches most flames in its vicinity when sampling near the stoichiometric boundary and most active reacting region, resulting in biases toward high oxygen and low fuel-rich species. All of the factors mentioned above could contribute to the fact that there is no zero or nearly zero O_2 region found in the combustion region.

A close comparison of the two Blind Canyon coal tests is provided by plotting the species profiles along a single horizontal sampling line in the IRZ, including NO, O_2, CO_2, and CO (Figure 8). The data symmetry is not perfect and the symmetry axis consistently misaligns with the geometric axis by a few centimeters. However, both the symmetry and the symmetry axis location indicate relatively high-quality data for such complex and large-scale systems.

These data illustrate measured profiles in the radial direction, located 12 cm from the reactor inlet. This location in the reactor contains among the steepest and most complex gradients in species concentration profiles (and all other properties) and therefore provides a rigorous test of both symmetry and reproducibility.

Combined with the reverse flow velocity predictions from CFD, it is obvious that large gradients of CO, CO_2, O_2, and NO appear around the reverse flow region (from -12cm to 16 cm radially), and outside the region, there was much less variation in the species profiles. This verifies that the reverse flow region strongly influences combustion processes.

The high CO reading (around 2000 ppm) might signal the existence of a locally fuel-rich region. However, CO generated from the decomposition of CO_2 at high temperatures (> 2400 K) could contribute to the high concentration of CO measured. This effect increases with increasing temperature (Lissianski et al. 2000). The measured peak CO values of 2000 ppm (0.2 mole fraction) could only be generated by CO_2 disassociation at temperatures well above those measured or predicted in this reactor. However, additional evidence suggests these high CO values arise in large part from fuel-rich regions in the current experiments. The existence of HCN, $NH_{3,}$ or both, accompanying the high CO region strongly indicate that a locally fuel-rich region exists at least transiently in these regions of the reactor. Kinetic and thermodynamic calculations show that neither HCN nor NH_3 survive a fuel-lean environment at 2000 K (Dean and Bozzelli 2000). Both species exist for a significant time (dozens of ms) in an overall fuel-rich environment, but less than 1 ms under fuel-lean conditions, which will be discussed in Section1.2.4. Therefore, the simultaneous existence of HCN or NH_3 with CO confirms the region as being locally fuel-rich at least a portion of the time.

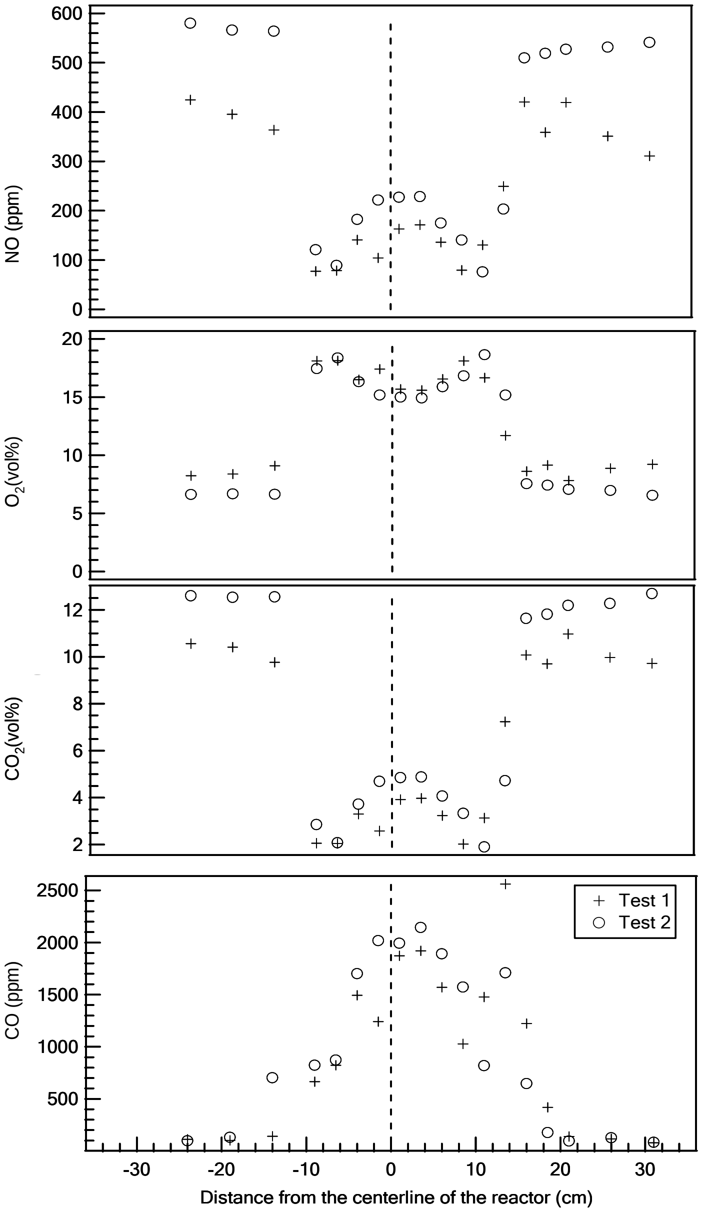

Figure 8 Results of replicate NO, O2, CO2, and CO measurements during two Blind Canyon tests positioned at an axial distance of 12 cm below the zero line (on a 3% O2 basis).

The top section of the BFR contains a region around the centerline characterized by high CO, and O_2 and low CO_2 molar concentrations. In this region, variations among the replicated data for all major and minor species are O_2, ±10%; NO, ±25%; CO, ±10%; CO_2, ±20%. Because of the turbulence impact, the O_2 measurement here is seemingly high.

In the near-wall region, the variation of some species between the two tests exceeds that observed near the centerline region. The disparity often increases as the probe approaches the reactor walls. The disparity in this region could arise from shifts in the local external recirculating region of gas flow. Such recirculating flows represent delicate balances in pressure and momentum forces. The sampling region (around the radial distance of 15 cm from the reaction centerline) corresponds to the approximate end of the external recirculation zone, which appears to shift slightly from test to test – a subtlety of the flow pattern unable to be exactly reproduced in these experiments from one test to the next. The sampling probe may also influence the structure of such recirculating zones in ways not precisely known and difficult to predict.

Comparison of maps from biomass tests to that of Test BC

This section discusses experimental data from the two pure biomass tests, as appear in Figure 9, respectively. In the Test S (straw) maps, the blank region observed close to the left wall of the reactor results from the shortage of measurement points, not a low gradient region.

Generally, the combustion region of both pure biomass tests is similar to that of Test BC, with Test SD (sawdust) exhibiting a wider radial penetration. The high CO_2 reading in the reacted-gas zone in Test SD is caused by the operating equivalence ratio (0.90), as confirmed by the lower reacted-gas region O_2 mole fractions.

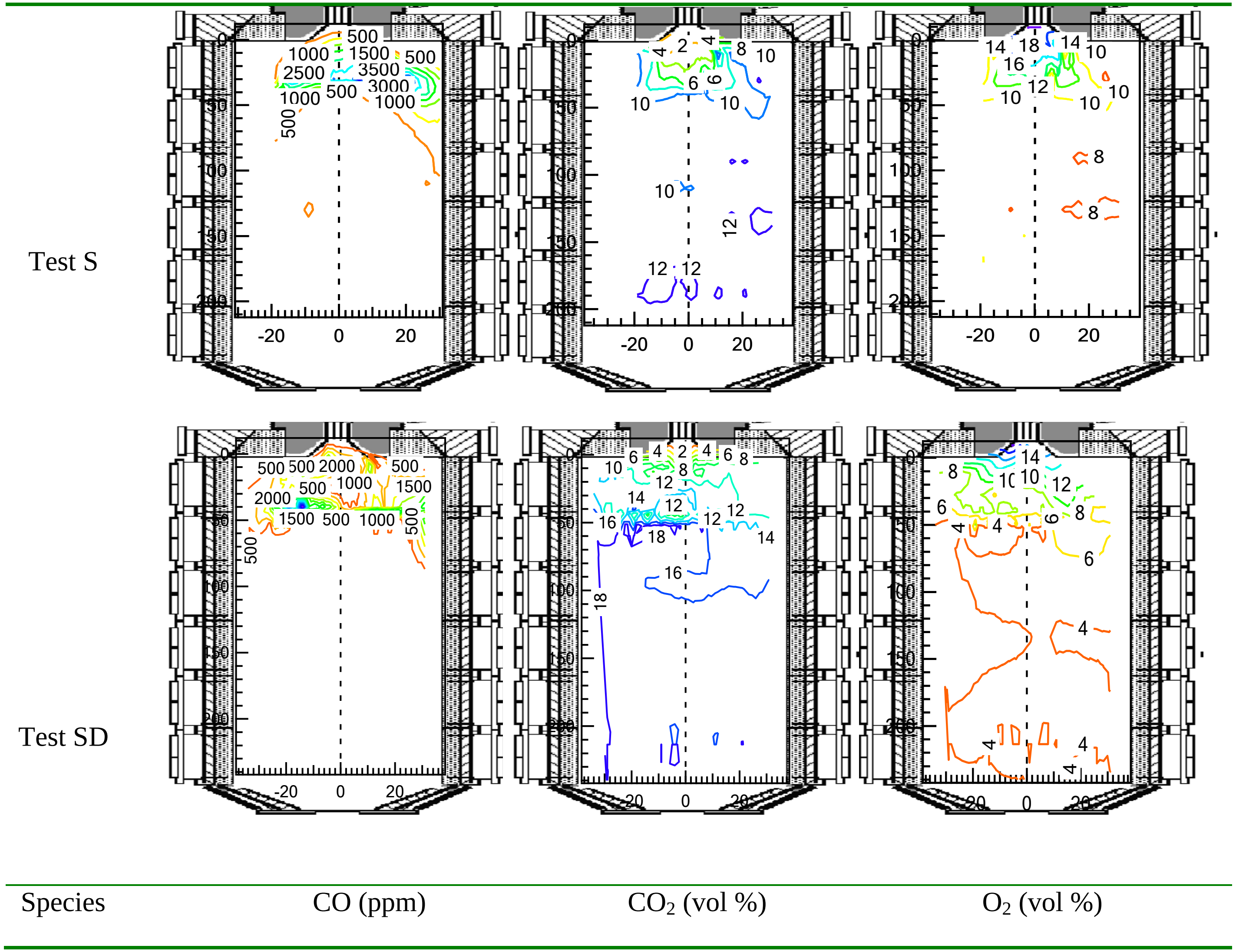

Figure 9 *Species maps of the two pure biomass: Test S (straw) and Test SD (sawdust)*

Axisymmetric maps of two biomass cofiring tests involving Blind Canyon coal and straw appear in Figure 10. The rest of the cofiring maps appear in Appendix I. In all the cofiring tests, the combustion region is larger in both axial and radial directions than in the Blind Canyon test: in Test 70S30BC, it reaches an axial distance around 60 cm, and during the other cofiring tests, it extends beyond the top two sections (over 80 cm). Section 0 discusses these differences in detail.

Below is a brief description of each species map.

Most of the CO detected resides in the top two sections (0-80 cm) in the reactor. The peak CO appears in a toroidal region at about 15 cm from the centerline and 30 cm from the inlet plane, occurring where the predicted axial velocity approaches zero as it changes from reverse flow to positive flow. From 80 cm and downstream, there is little change compared to that observed in the combustion regions. The high CO reading, which acts as a fuel-rich indicator, provides strong and definitive evidence of transient fuel-rich eddies under the overall fuel-lean conditions, as further indicated by the presence of HCN and NH_3, as described in Section 4.1.1.

CO_2 shows a monotonic increase with increasing distance from the inlet. Outside the combustion region, CO_2 reaches levels similar to that measured from the bottom section of the reactor. After the top two sections, the profile becomes nearly flat, indicating that solid fuel combustion is nearly complete within the top two reactor sections (0-80 cm).

In the combustion region, O_2 monotonically decreases with increasing distance from the inlet. Consistent with the CO_2 profile, outside the reverse region little variation in O_2 concentration appears. Comparing the CO and O_2 maps, high mole fractions of O_2 coexist with high mole fractions of CO, an interesting and quantitative feature of this combustor. A detailed discussion of this feature appears earlier.

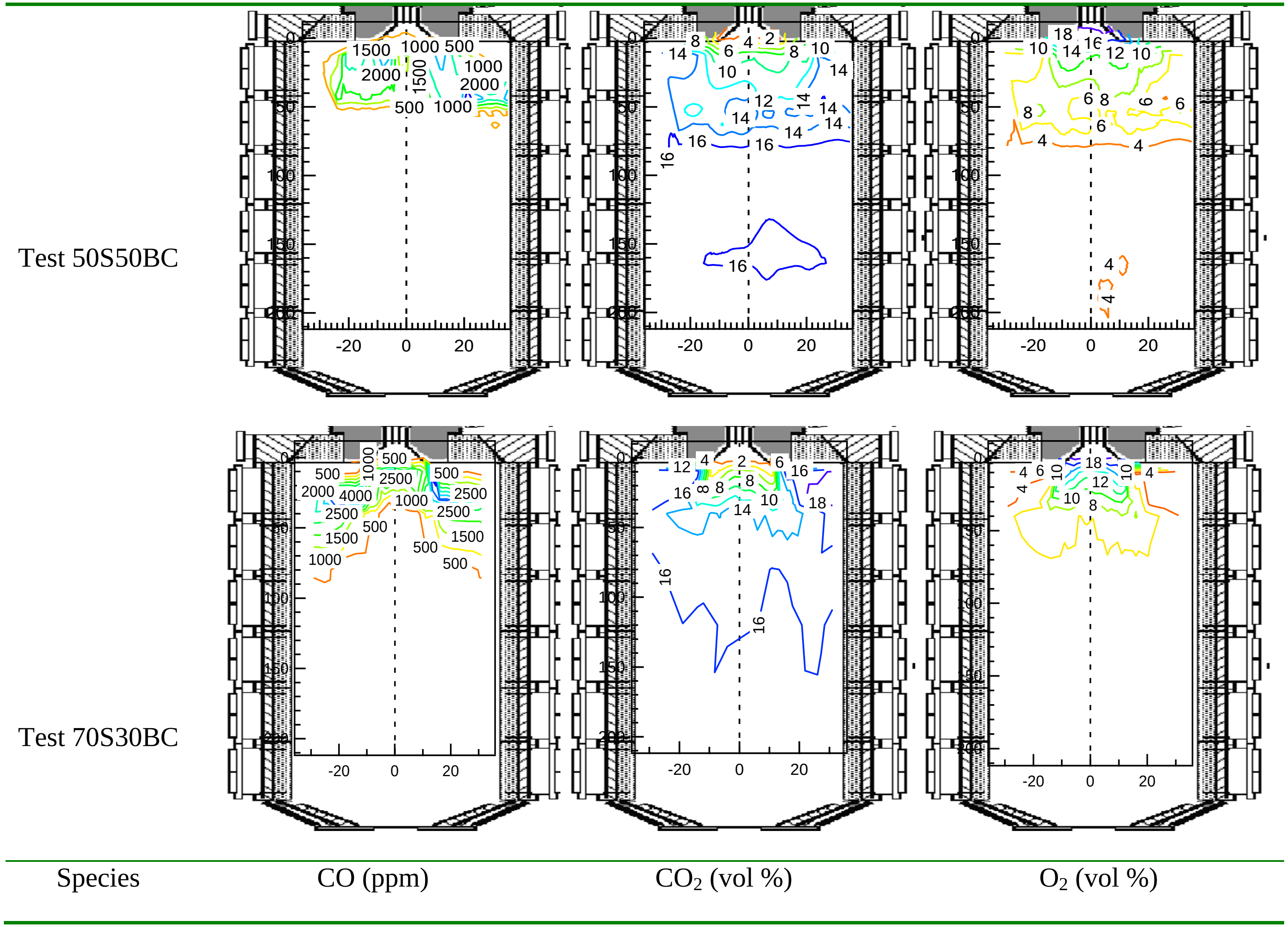

Figure 10 *Species maps of the two cofiring tests: Test 50S50BC (50% straw and 50% Blind Canyon, wt) and Test 70S30BC (70% straw and 30% Blind Canyon, wt).*

1.2.4 Experimental data analysis

This section is focused on the regressions of the experimental data for more insightful information on the biomass combustion behavior under swirling flows.

The axisymmetric species maps mentioned so far illustrate mole fraction distributions of major gas species during biomass combustion under swirling flow conditions, and demonstrate differences in the size of the combustion zone/fuel-rich region. These multidimensional data can also be used to reveal the performance of normalized mole fractions of each gas species, and NO_x formation analyses can be done, leading to insight into emission generation during biomass combustion.

Two methods of data analysis appear below. The first is to compute the spatial map of the stoichiometric ratio from the species maps, evaluating the impact of burning biomass on the flame structure. The second is to monitor the trends in gas species mole fractions as a function of axial distance. This can help reveal the effects of biomass high volatile content during firing/cofiring in the swirling flow region, as well as clarify the mixing and devolatilization effect in the near-burner region.

Stoichiometric ratio maps

The stoichiometric ratio is the inverse of equivalence ratio. Qualitatively, it is the air to fuel molar ratio in the existing system normalized by the same ratio under conditions of no excess of either fuel or oxidizer. Stoichiometric ratio is most commonly represented for the entire system, not just the gas phase. Calculations of stoichiometric ratio for complex systems such as these are not entirely straightforward because many of the species have several stable oxidation states, so distinguishing fuels from oxidizers can be ambiguous. Furthermore, the biomass fuels are highly oxygenated, so a given stoichiometric ratio with biomass represents a significantly different environment than the same value for coal. To resolve these and other issues, an alternative definition of stoichiometric ratio is adopted here. The local stoichiometric ratio (φ) can be treated as the ratio of the oxidizing potential to the reducing potential. This can be mathematical expressed as follows:

$$\varphi = \frac{\sum_{j}^{s} x_j \left(\sum_{i=0}^{e} -v_i n_{i,j} \Big|_{v_i<0} \right)}{\sum_{j}^{s} x_j \left(\sum_{i=0}^{e} v_i n_{i,j} \Big|_{v_i>0} \right)} \qquad \textbf{\textit{Eqn 1.4}}$$

where the symbols are defined as follows:

v_i : the reference oxidation state/valence of element *i*;

$n_{i,j}$: the number of moles of element *i* in species *j*;

x_j : the mole fraction of species *j* in the stream (which can be either reactants or products); *e* and *s*: total number of elements in one species and the total number of species respectively. The reference oxidation states are the valences under fully oxidized conditions – not the actual valence of the element in the flow, i.e., C = +4, H = +1, O = -2, Al = +3, N = 0, S = +4, etc. Molecular nitrogen and other atoms that exist in zero oxidation state at reference conditions do not impact the value of the equivalence ratio. Therefore, the only species of significance for this calculation include CO (in the fuel-rich region), CO_2, O_2, SO_2, and H_2O, with all others being of too low concentration to be significant in the calculation. Based on the measured species compositions, local gas-phase stoichiometric ratio is determined based on Eqn 1.4

Gas species normalized mole fractions (1-D profile)

The normalized gas species mole fractions along the reactor axis, termed a 1-D profile, are the ratio of the integration of the mole fractions with CFD temperature and axial velocity predictions across each horizontal plane, as described in the following equation.

$$Y_i(z) = \frac{\int_0^R \frac{P}{RT(r,z)} y_i(r,z) v(r,z) 2\pi r dr}{\int_0^R \frac{P}{RT(r,z)} v(r,z) 2\pi r dr} \qquad \textbf{Eqn 1.5}$$

where the symbols are defined as follows

$Y_i(z)$: the mole fraction of species i on the horizontal plane with an axial distance of z;

$T(r,z)$, $v(r,z)$, and $y_i(r,z)$: the temperature, axial velocity, and mole fractions of species i as functions of radial and axial position, respectively;

The mole fractions of species, $y_i(r,z)$, were determined from the measured values while the temperature and velocity were obtained from simulations. The reactor pressure P can be assumed as constant at 0.85 atm. R is the ideal gas constant.

In practice, P and R can be eliminated from the equation (assuming P is consistent from day to day) but are retained above to illustrate the derivation of the above equation. The integrand in the numerator represents the local molar flux times the mole fraction and the integrand in the denominator represents the local total molar flux. The function represents the flux-averaged mole fraction at a given axial position.

Features of biomass combustion under swirling flows

In this section, possible changes in the flow pattern during biomass combustion is discussed first, followed by a discussion on the influence of two features of biomass properties, large particle size and high content of volatiles.

Among the nine tests, as shown in Table 3, Test BC and Test S have relatively low equivalence ratios, 0.77 and 0.64, respectively. The ratios of the primary to secondary feed rates range from 0.52 (Test 50S50BC) to 0.134 (Test P). A parametric study was carried out with the modeling to verify the influence of changes in equivalence ratio and air set-up ratios on the reverse flow zone and gas species contours. Three cases were defined based on the operating conditions of a pure coal test, Test BC, and a biomass test, Test S, respectively. For the same fuel, all the cases have the same secondary air feed rate.

Case 1: The equivalence ratio and air set-up are same as those in Table 3, i.e. Test BC has an equivalence ratio of 0.77, Test S 0.64, and the air set-up ratios are 0.079 and 0.1, respectively.

Case 2: The equivalence ratio is 0.9, and air set-up ratio is 0.1.

Case 3: The equivalence ratio is 0.9, and air set-up ratio is 0.05.

The major gas species (CO and CO_2) and reverse axial velocity contours of straw and Blind Canyon combustion are shown in are shown in Figure 11 and Figure 12, respectively. For both groups, the simulation results show the combustion region, where the color gradient is high, resides in the similar location in the reactor, although the peak differs among the cases for the same fuel. The axial reverse flow velocity contours are of similar shape for the same fuel, and this shows there is little difference in the size and scale of the reverse flow region with the equivalence ratios and air set-ups considered for straw and Blind Canyon. Therefore, among the tests, even with smaller equivalence ratios (0.64, and 0.77) than the other tests and different air setups, modeling results indicate few qualitative differences in flows or structure.

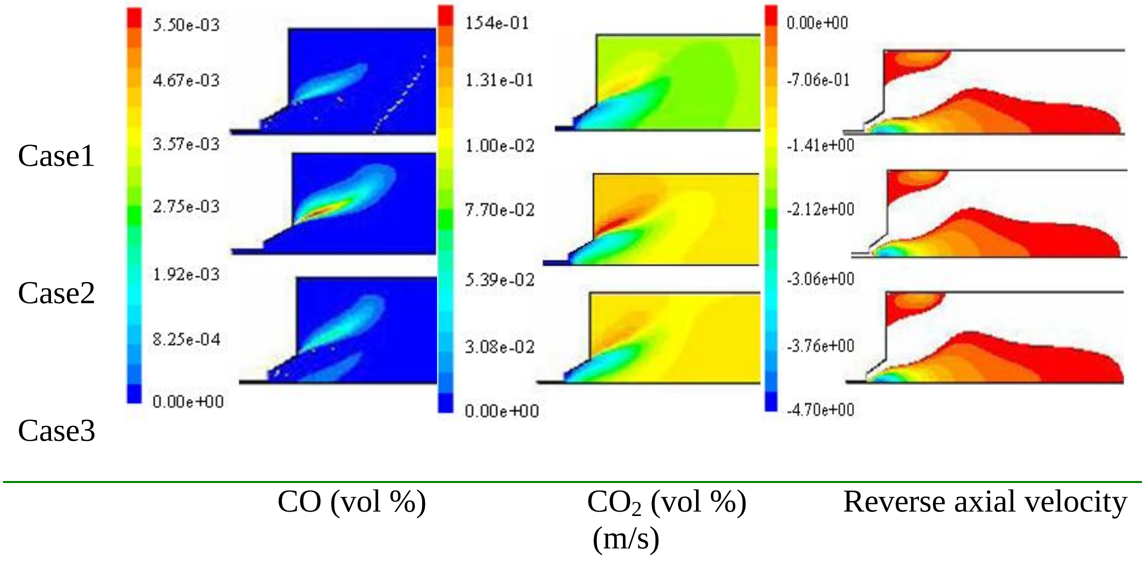

Figure 11 Contours of CO, CO2 and axial reverse velocity from simulations of straw combustion.

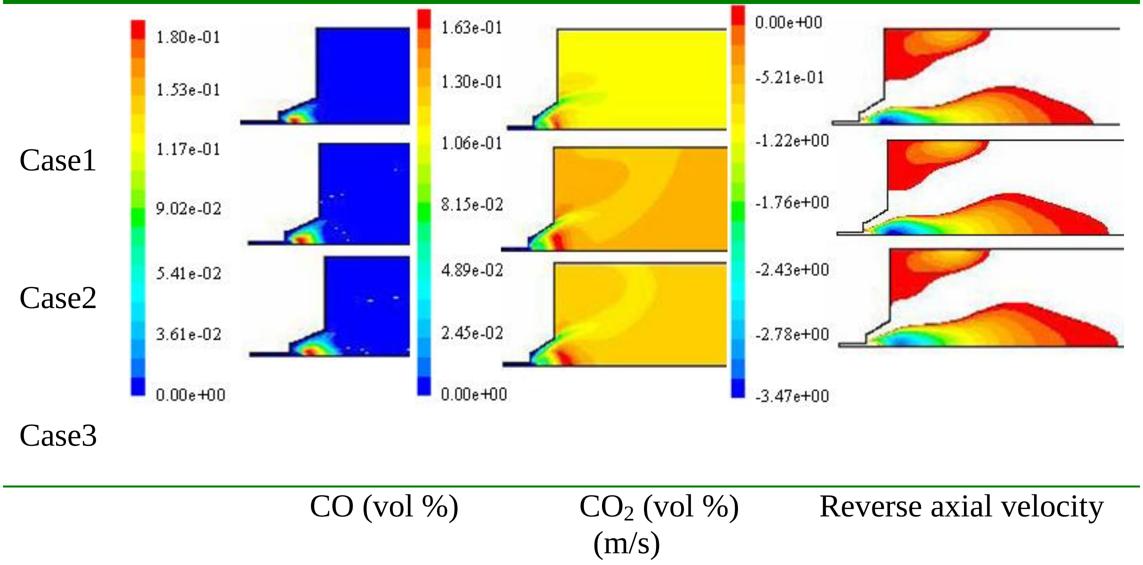

Figure 12 Contours of CO, CO2 and axial reverse flow velocity from simulations of Blind Canyon combustion.

Flow pattern

This discussion compares predictions of reverse flow zones from biomass tests to those of the pure coal case (Test BC).

Figure 13 illustrates the predicted reverse flow contours from simulations of the single fuel tests (Test BC, P, S, and SD). For a better description, all the contours were plotted with the same scale (from -4.7 m/s to 0 m/s). Both the IRZ and ERZ are predicted to be axisymmetric. The core of the former resides around the reactor axis right below the quarl exit. Because of the differences in the ratio of primary air to the secondary air feed rates, the predicted peak reverse flow velocity varies among the tests. Test S has the highest secondary feed rate (150 kg/hr) and the strongest predicted peak reverse flow velocity (-4.7 m/s). Test P has the smallest secondary feeding (115 kg/hr) and the weakest peak reverse velocity (-1.14 m/s, not shown in the figure). Test SD and Test P tests have the same secondary air feed rate, but the larger primary to secondary air flux ratio the latter (0.134) counteracts the scale of reverse flows, resulting in a less negative peak value in Test P than Test SD. The predicted size of IRZ also differs among these simulations, and this is caused by the air feed rate set-up. Modeling of Test BC predicts the smallest IRZ, and Test SD and Test S simulations demonstrate the largest IRZ. With the current relatively simple models, the observed differences in the IRZ size (discussed in the next section) couldn't be explained satisfactorily, but all the single fuel simulations indicate that combustion of biomass doesn't penetrate the IRZ or otherwise qualitatively alter the flow pattern in a swirling flow burner.

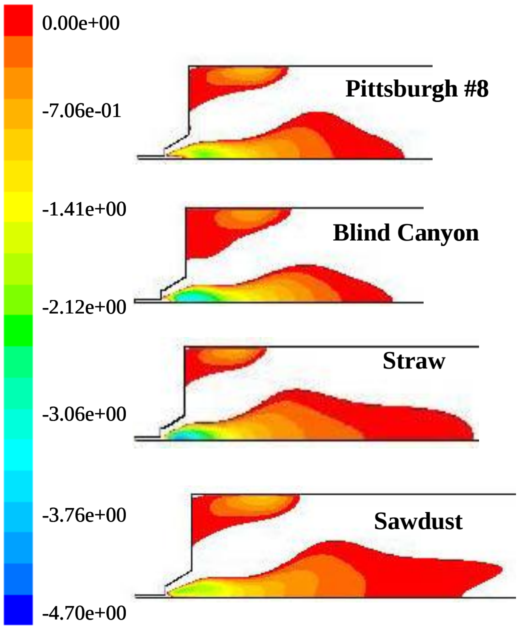

Figure 13 The reverse flow contours (m/s) predicted from simulations of the pure fuel tests.

The predictions of the IRZ from cofiring simulations are illustrated with cases involving both straw and Blind Canyon. The reverse flow contours are plotted in Figure 14. The flow pattern from cofiring simulations is similar to the pure fuel modeling results. The predictions indicate cofiring minimally impacts the qualitative features of flow dynamics. The swirling flow may be sufficient to sustain the adverse pressure zone (pressure gradient that increases in the direction of the average flow) around the centerline, resulting in a reverse flow region near the burner exit, even in the presence of the large biomass particles.

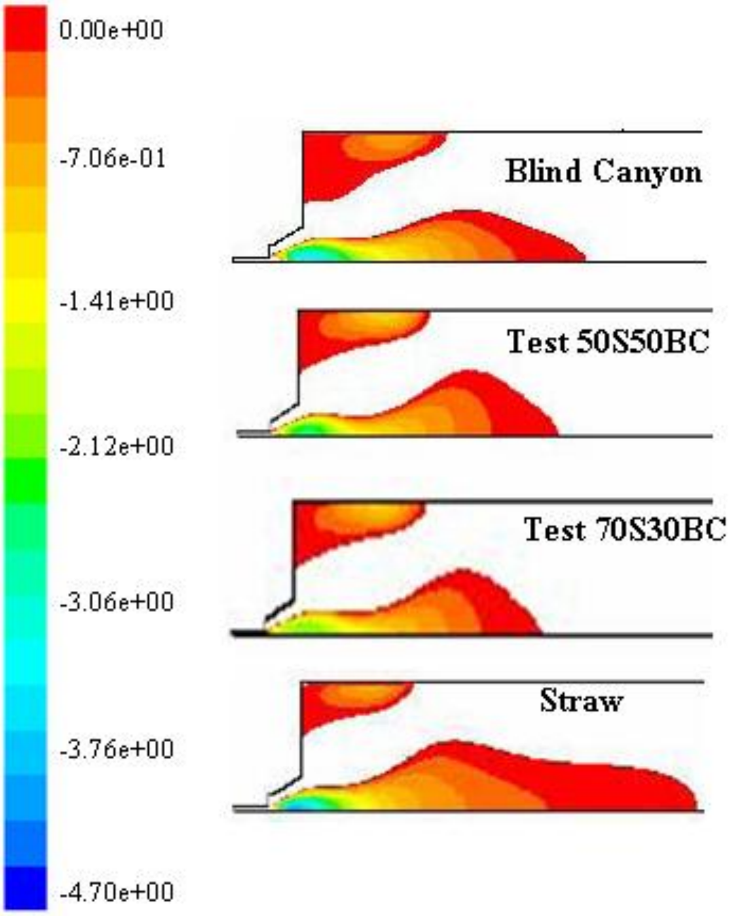

Figure 14 Comparison of reverse flow contours from the two cofiring tests and their corresponding pure fuel tests involving straw and Blind Canyon.

In summary, with the current modeling strategy, no qualitative change in the reverse flow pattern between biomass and coal combustion in the swirling flow burners appears. The impact of biomass combustion on the flow pattern might be limited. This indirectly indicates that the expansion of the size of the combustion region during biomass tests is possibly caused by the fuel properties, such as moisture content, volatile content, and particle size, as discussed in the next section.

Influence of biomass properties: particle size and volatile content

The particle size distributions of fuels used in this project appears in Figure 1. Straw has the largest average particle size (475 micron), larger than that of sawdust (370 micron). These values are much smaller than commercial fuels, which are on the order of millimeters or even centimeters. Both coals considered have an average particle size of 70 micron. In the CFD modeling, as mentioned previously (Table 4), sawdust is assumed to have a volatile content of 95% (mass basis), which is slightly higher than that of straw (90%), Pittsburgh #8 (60%) and Blind Canyon coal (50%). Sawdust generally has a higher volatile content than straw, and both are much higher than coal.

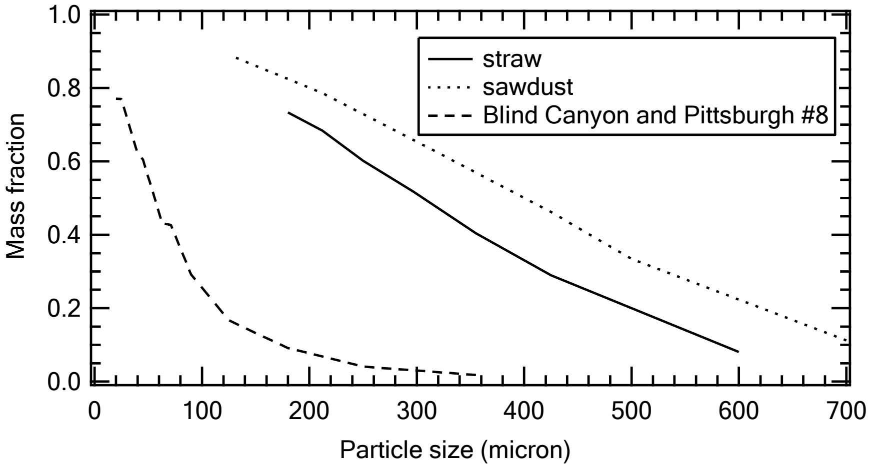

Figure 15 Distribution of particle size of biomass and coal used.

During this combustion process, for the same type of fuel, particles with a larger size need more oxygen and a longer time to both initiate (warm-up) and complete reactions. High volatiles contents mean more off-gases during devolatilization, generally CO, CO_2, H_2O, and a small amount of hydrocarbons. This facilitates the initiation of combustion and helps sustain flames by providing combustible gas mixtures.

The impact of the biomass particle size on combustion could be reflected from the comparison of predictions of CO and CO_2 from simulations of Test BC, Test SD, and Test S, in an order of increasing fuel particle size, as illustrated in Figure 16. For Test BC simulations, this region is attached to the inlet. Predictions of Test SD show insignificant expansion of the CO and CO_2 high-gradient region. For Test S, this region moves further downstream still. Combined with the biomass firing and cofiring axisymmetric maps mentioned in Section 0, these predictions provide qualitative information on the influence of particle size. The expansion of the combustion region can be explained as follows: after fuel is injected into the reactor against the recirculating preheated flow, devolatilization is quickly initiated. Blind Canyon has a relatively low volatile content (50%), and the volatiles are rapidly consumed. Since biomass particles are larger (straw: 475 micron; sawdust: 370 micron) than Blind Canyon (70 micron), they heat more slowly and their devolatilization occurs over a longer path and, due to the larger volatile content (straw: 90%, wt; sawdust: 95%, wt; Blind Canyon: 50%, wt), biomass consumes more oxygen, causing the expansion of the high CO region (combustion region). Furthermore, biomass produces larger char particles than coal, despite the higher volatile content. Char particle combustion generally produces dominantly CO (as opposed to CO_2) and biomass will produce larger CO trails as the particle require longer to burn than do coal char particles.

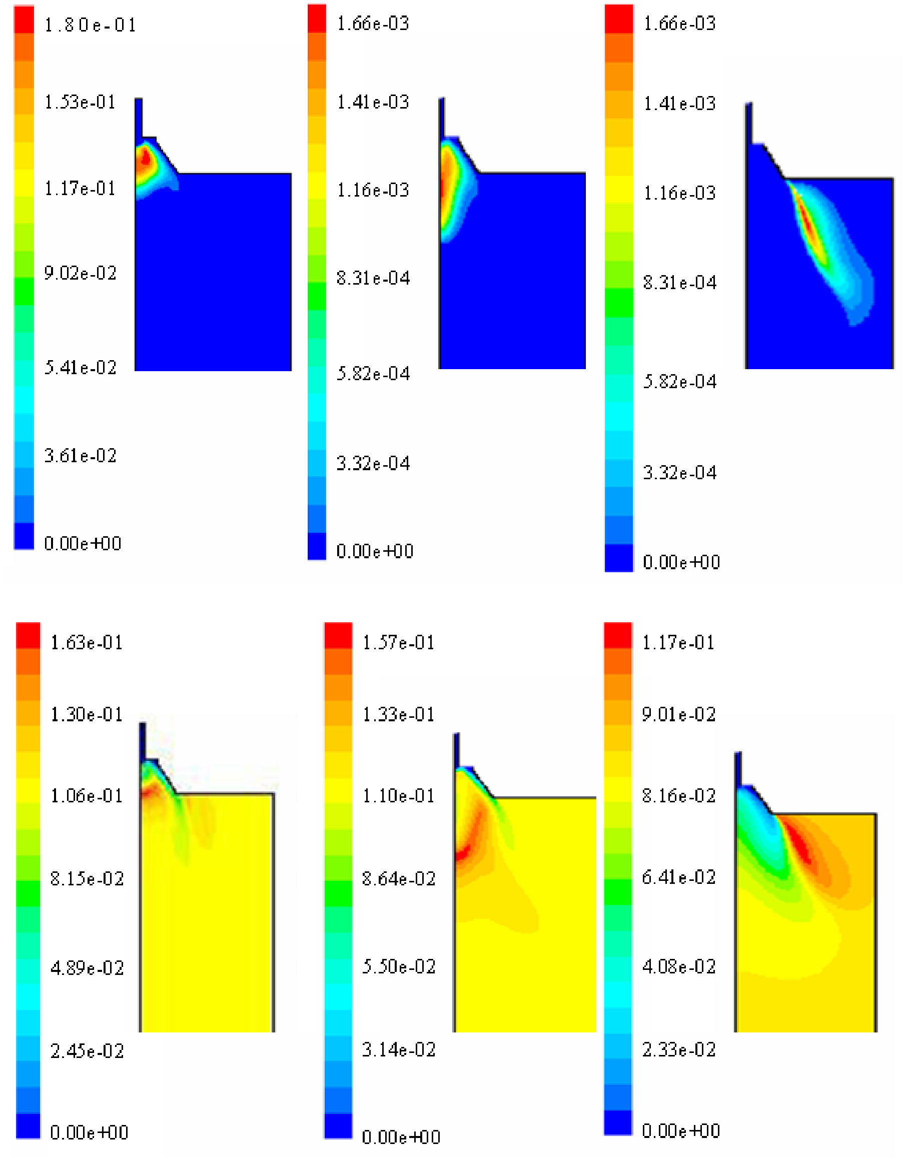

Figure 16 Comparisons of CFD predictions top: CO (ppm); bottom: CO2 (vol %) of Test BC, Test SD, and Test S.

The 1-D gas species profiles from the pure fuel tests are displayed in Figure 17.

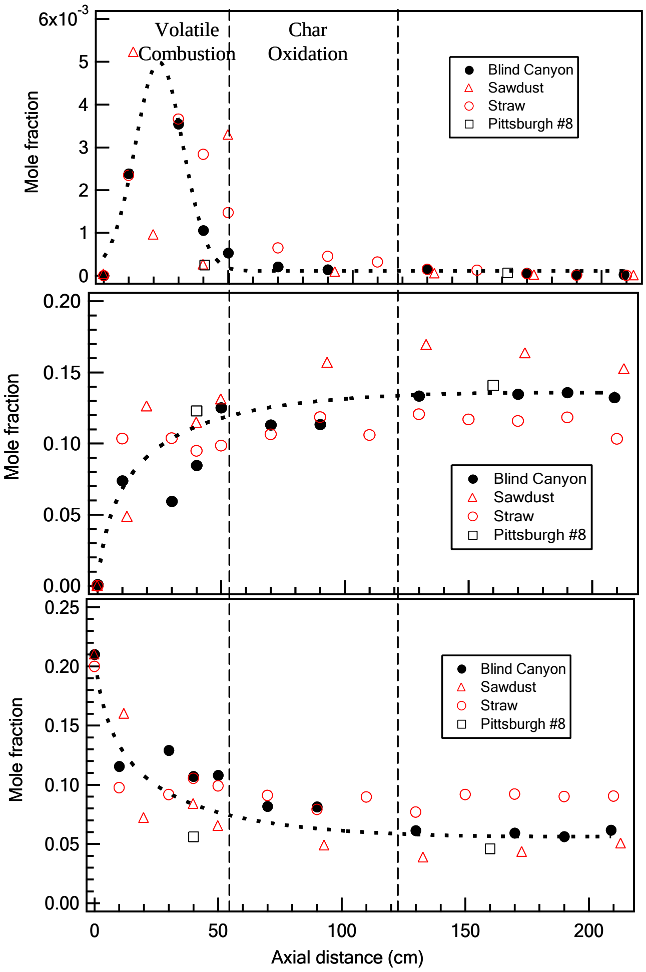

Figure 17 1-D profiles of CO (top), CO2 (middle), and O2 (bottom) during pure fuel tests (The dot-lines describe the trends of normalized results of Test BC along the reactor axis)

The 1-D profiles for each species indicate that the pure biomass test data follow a similar pattern to that of the Blind Canyon test. At the inlet, represented by the origin in the graph, CO and CO_2 mole fractions are almost zero, while O_2 has a maximum concentration, where the combustion process has not fully begun. With increasing axial distance (about 10 cm), particle devolatilization dominates the process, leading to a sharp increase in CO (from 0 to 2000 ppm for sawdust), accompanied with an increase (from 0 to 0.05, mole fraction) in CO_2 and a decrease (from 0.2 to 0.15, mole fraction) in O_2. After enough mixing of air and fuel, from 10 cm to about 50 cm, CO reacts with oxygen in the mixing-controlled reactions, and about 80 % of the overall fuel is consumed by about 50 cm. Simultaneously, CO_2 monotonically increases, and O_2 is reduced by about 70% by 50 cm. It is from 0 to 50 cm where the main part of combustion happens and the IRZ resides. Downstream of this region, CO continues decreasing until fully reacted by about 170 cm. CO_2 increases to a maximum level about 130 cm. O_2 drops to a relative steady level about 50 cm.

These 1-D profiles also provide evidence of the high volatile influence. Biomass is an oxygenated fuel, so CO reacts with oxygen released from volatiles in addition to O_2. Therefore, Test S and SD data show an earlier jump of CO_2 to the steady level (around 0.1, mole fraction by 20 cm) while CO mole fractions are still increasing compared to the coal data. The one presumably spurning CO data point at 50 cm of Test SD seems unlikely, since sawdust has higher volatile content and smaller particle size than straw, in the region where the reacted-gas and combustion regions overlap, there should be plenty oxygen supply to consume CO. It is very unlikely that the CO concentration is about three time of that from Test S. As a rule, the biomass combustion cases exhibit more rapidly increasing CO_2 profiles and CO profiles that penetrate further into the reactor compared to the Blind Canyon coal. Oxygen profiles reflect similar trends, with the coal oxygen consumption in the early section of the reactor (the top 50 cm) less than that of the biomass fuels. Similar trends appear whether comparison is mad with biomass at lower (straw: 0.64) or higher (sawdust: 0.90) equivalence ratios relative to that of the Blind Canyon coal. All of these trends are consistent with the higher volatile content and larger average particle size of biomass used.

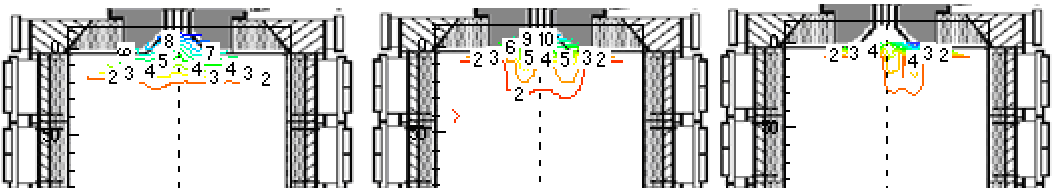

Test 50S50BC Test 70S30BC Test 70SD30BC

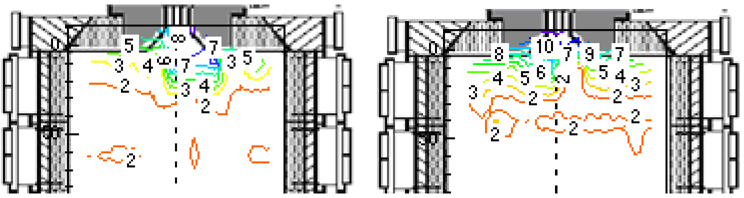

Test 70SD30P Test 70S30P

Figure 18 Stoichiometric ratio maps of the cofiring tests calculated based on Eqn 1.5.

Char has a much higher heat density than volatiles. In contrast to the high-volatile, low-char biomass properties, coal lacks volatiles and forms more char. During the cofiring tests, both biomass and coal are injected simultaneously through the same path. The mixture contains components with both high and low volatiles and fixed-carbon contents and large and small particle sizes. Stoichiometric ratio maps of the cofiring tests (Figure 18) indicate that attached flames with wide radial penetration occur compared to Test BC. The cofiring 1-D profiles of CO, CO_2, and O_2 are plotted in Figure 19, in which each species demonstrated a generally similar trend to that of Test BC. The data show high mass fractions (70%) of biomass leading to larger devolatilization regions remains evident, where the cofiring tests have higher 1-D CO_2 values than that from Test BC within the top 50 cm, accompanied with equal to higher CO values than the latter as well. Coal particles follow gas stream lines more closely and mix more rapidly with gases in the swirling flows than do biomass particles. These data suggest that biomass helps stabilize flames (as indicated by faster increases in CO and CO_2 mole fractions in the reactor), presumably because of its high volatiles content and despite its relatively large particle size. Furthermore, the size and intensity of the fuel-rich core, as indicated by the magnitude and axial extent of the non-zero CO normalized mole fractions, increases with biomass cofiring, presumably for the same reason.

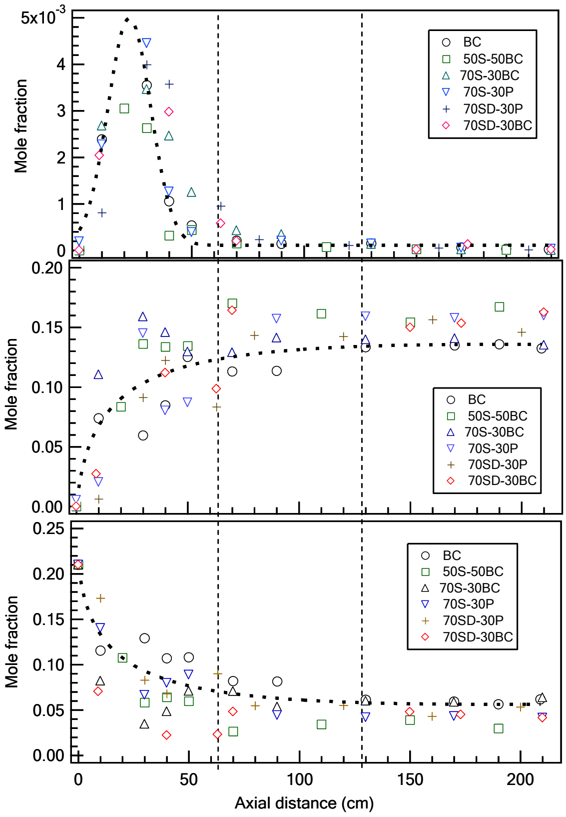

Figure 19 *1-D profiles of CO (top), CO2 (middle), and O2 (bottom) during cofiring tests compared to that of Test BC (The lines show the trend of the normalized results of Test BC along the reactor axis)*

CO spatial profiles

The major gas species mole fraction data contour maps are exampled by CO data in Figure 20. The data represent results from a vertical slice of the reactor passing through its geometric centerline and including both radial directions from this nominally axisymmetric centerline. In the maps, a high contour density represents regions of steep mole fraction gradient, indicating a reaction-dominant region or combustion zone. This zone expands vertically from the inlet to about 40 cm (within the top reactor section) and horizontally to nearly reactor walls. The regions with few contours denote the relatively flat profiles, and this is where product gas species (mainly CO_2, NO, and H_2O) dominate or the reacted-gas zone. The symmetry of the data around the centerline is one test of data quality. As seen, all data exhibit a reasonably well-defined symmetry axis.

Consistent with the high CO mole fraction existing near the reactor inlet, HCN and NH_3 were found mainly in the top section, 0-50 cm below the quarl. Though all the tests involved overall fuel-lean conditions, the existence of HCN/NH_3 provides strong evidence that there is a locally and probably transient fuel-rich region in the top section of the reactor.

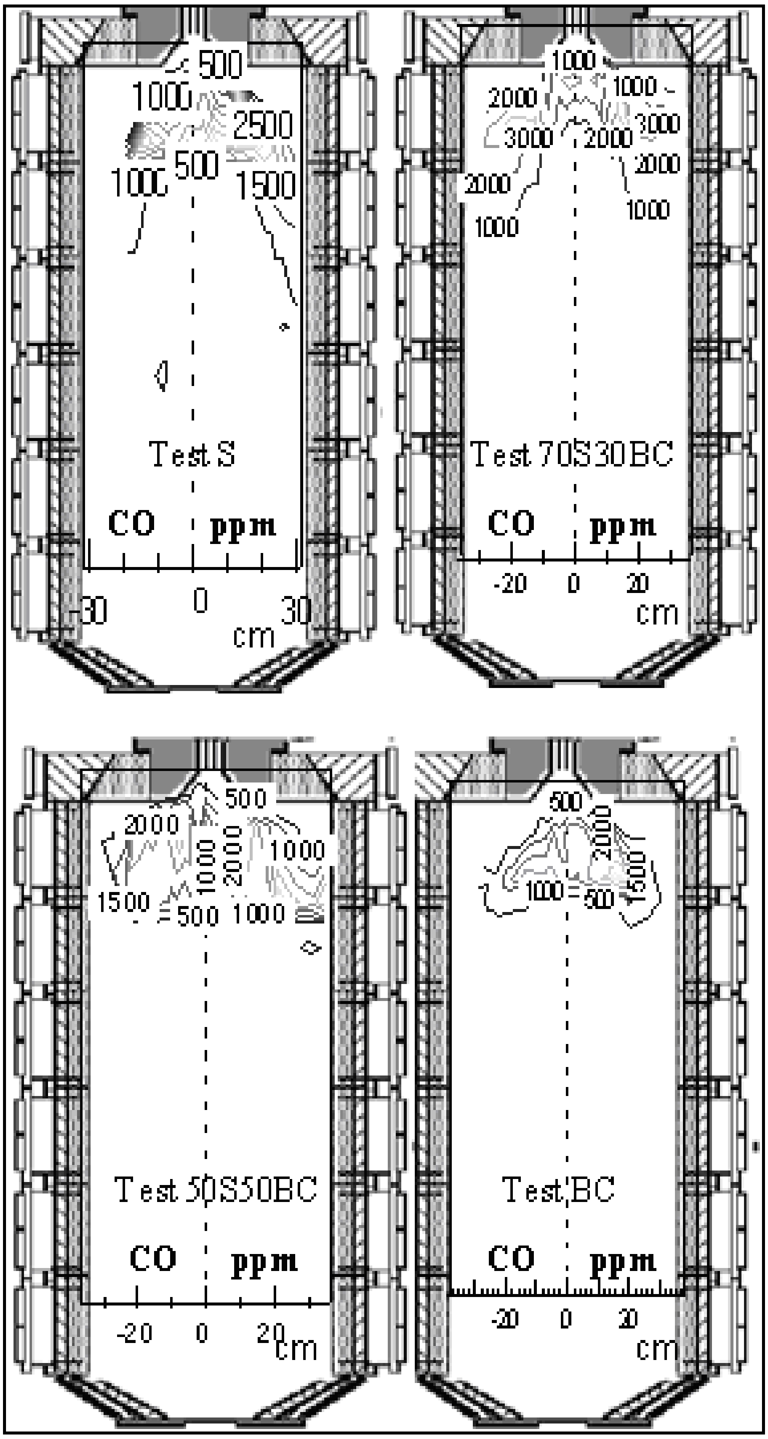

Figure 20: Axisymmetric CO spatial profiles.

Measurements of HCN and NH_3

Indirect evidence of the minimal impact of sample conditioning, specifically water condensation, on the HCN/NH_3 concentrations appears in Figure 21, which illustrates the real-time measurement of NH_3 and HCN with their respective CO profiles from the pure straw test and pure Blind Canyon test. Very high correlation exists between the CO and both the HCN and NH_3 signals. The oscillations in the NH_3, HCN, and CO profiles arises from alternating the probe position between the fuel-rich region and the reacted-gas region of the coal and straw flames, with the intent to test the gas measurements at extreme conditions as major gas species concentrations change significantly. Though only very limited amounts (less than 15 ppm) of HCN and NH_3 are detected in the flue gas, the peak amounts appear at the same time as the peak CO content.

Since the measured NH_3 and HCN closely follow fluctuations in CO and during their measurements no water condensation was detected through the optical access in the cyclone (the lowest-temperature and elevation point in the sample train), the impact of water condensation on the gas sample should be minimal.

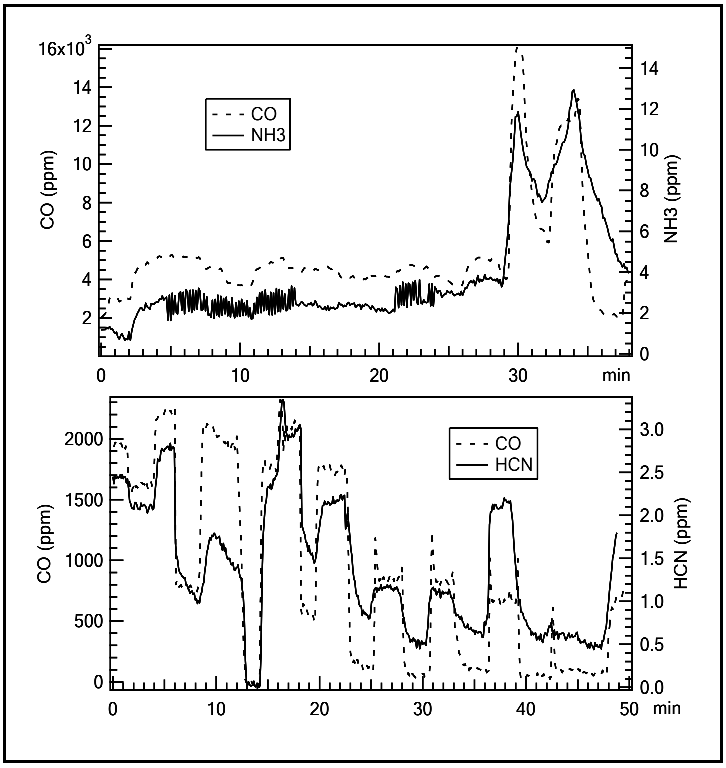

Figure 21. Temporal variations in NH_3 and HCN concentrations with CO concentration in the swirling section of the BFR. (top) NH_3 under Test S (bottom) HCN during Test BC

Figure 22 to Figure 25 depict the HCN and NH_3 maps from the four tests involving straw and Blind Canyon. In Test BC, HCN dominates NH_3 as the primary fixed-nitrogen species in the gas phase. The same is true in Test 50S50BC. As the mass fraction of straw increases, in both Test 70S30BC and Test S, NH_3 becomes the dominant fixed-nitrogen species (and NO intermediate) in the fuel-rich region. This clearly shows that straw and Blind Canyon release nitrogen in different forms and generate different NO_x intermediates. In Test 70S30BC, NH_3 showed much higher values than that during Test S. This is highly possible because of the largely expanded combustion region and higher flame temperature resulted from the local enrichment of both high amount of off-gases and char during the co-firing test.

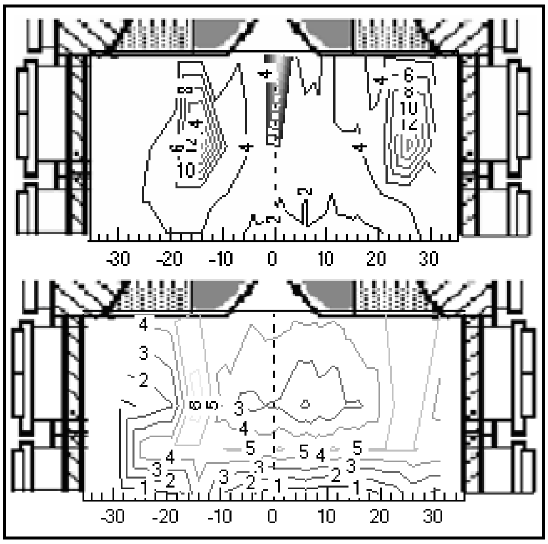

Figure 22. NH3 (top) and HCN (bottom) maps from Test S

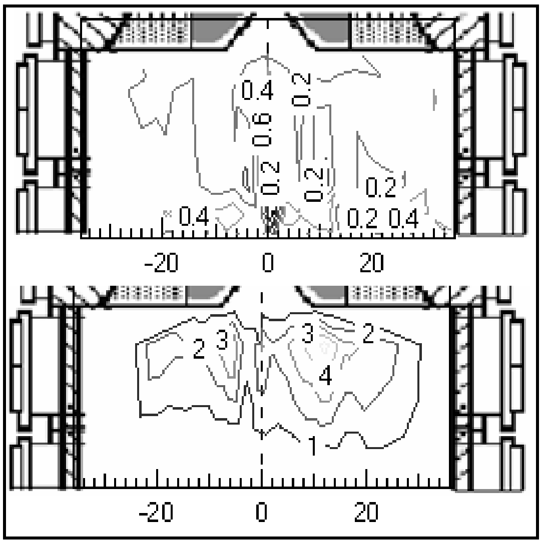

Figure 24. NH_3 (top) and HCN (bottom) maps from Test 50S50BC

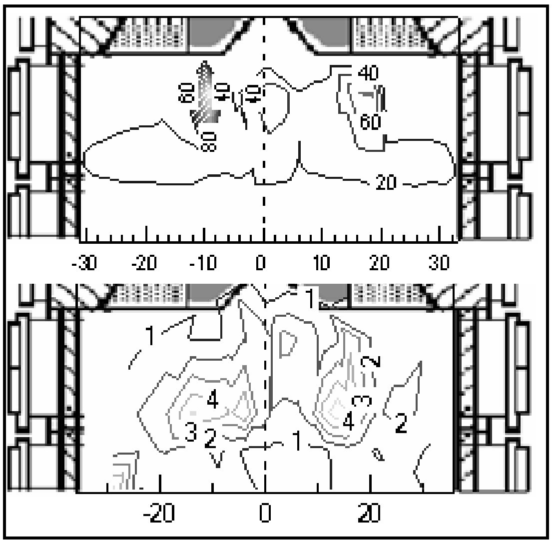

Figure 23. NH3 (top) and HCN (bottom) maps from Test 70S30BC

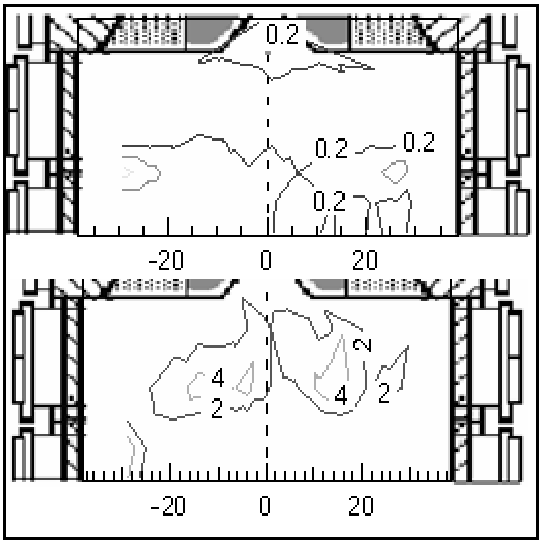

Figure 25. NH3 (top) and HCN (bottom) maps from Test BC

A summary of the NH_3 and HCN maps of all the cases leads to several conclusions as follows:

HCN and NH_3 could be measured in the locally fuel-rich region under the overall fuel-lean tests with the intrusive data collection system, which was confirmed by the consistency in the trend between light nitrogen species and CO, even though CO is much more stable than HCN and NH_3 through the flame front.

NH_3 is the major fuel-NO_x intermediate detected in straw firing and co-firing (with a mass fraction of 70%) tests, while HCN is the major intermediate in coal flames and biomass co-firing with a coal mass fraction of 50%.

1.3 Subtask 1.3: Single swirl burner aerodynamics and stability

The objective of this subtask was to characterize the aerodynamics of swirl-stabilized burners under isothermal conditions using laser-based experimental techniques, such as Laser Doppler Velocimetry and Particle Image Velocimetry. A significant amount of time was spent designing and building a test facility at Aalborg University that allows detailed optical measurements to be undertaken in the near burner region of a down-scaled commercial burner. The effort to collect high quality experimental data was focused on Laser Doppler Velocimetry as this measurement technique offers the best possibility to compare time averaged and fluctuating velocity components on a point-by-point basis.

1.3.1 Design of cold flow test facility at AAU

A test facility with a down-scaled low-NOx burner was build for investigation of the near burner flow field. The test facility consists of a closed water circulation loop. Water was chosen as fluid instead of air because it simplifies seeding and because much lower flow velocities are required for a given Reynolds number. A photograph of the rig appears in Figure 26 with the main components labeled. An electro-magnetic flow meter with a measurement range of 0–280 m3/h was mounted to the main pipe to measure the flow rate. Above the tank the flow splits in a manifold. The manifold’s four branches each feed one of the four burner inlets; centre, primary, secondary and tertiary. Each branch out of the manifold has a valve with a pressure transducer on each side to control and measure its individual mass flow. A pump capable of providing a mass flow up to 80 m^3/h circulated the water in a loop. The pump is wired to a frequency converter which makes it possible to control the circulating mass flow.

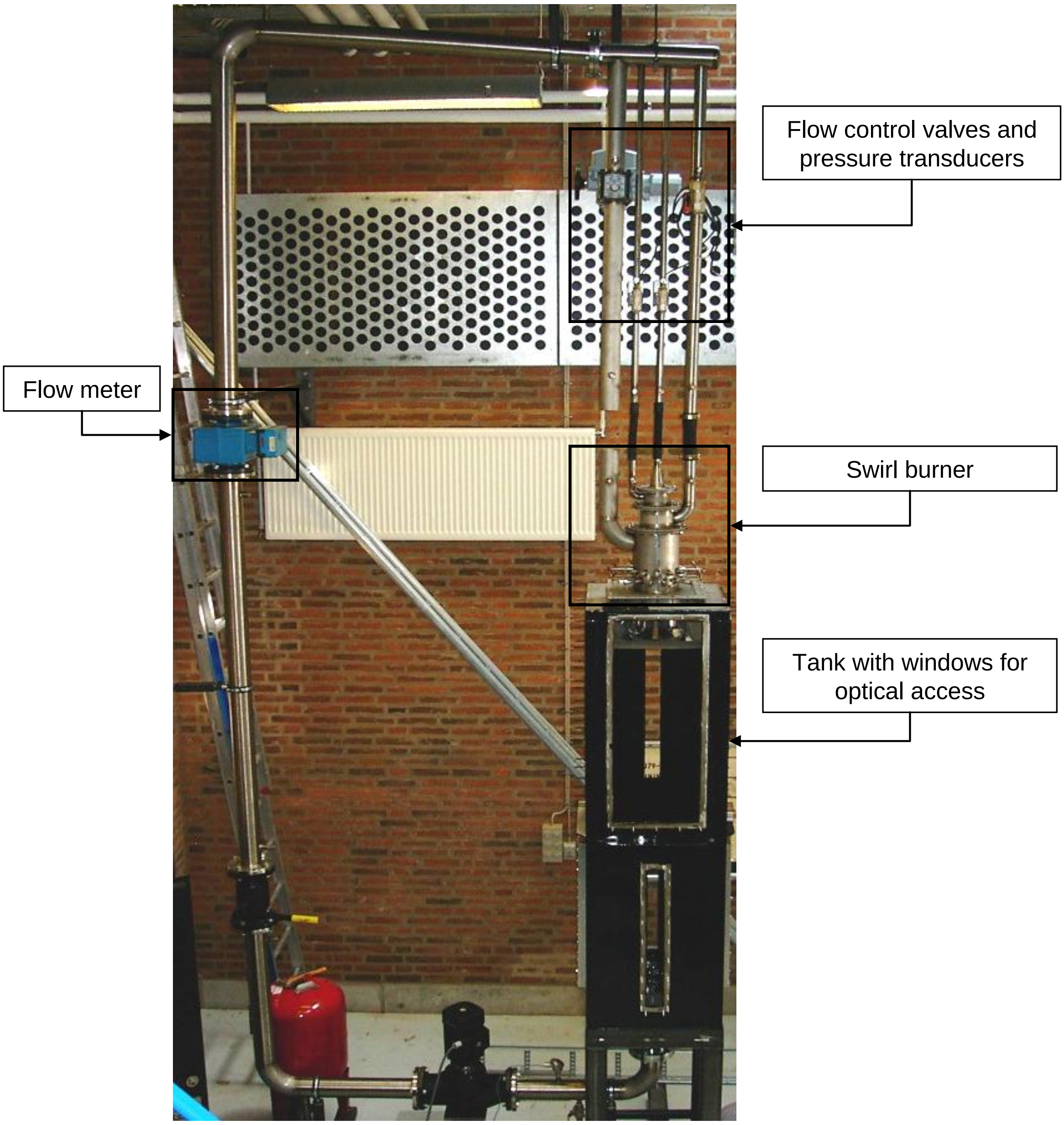

Figure 26 Photograph of the IET-AAU cold flow test facility

The internal height of the tank below the burner head is 1.95 m and the cross section is 0.6 by 0.6 m. It is made of 3 mm thick steel plates and 40 mm thick plexiglas windows. Windows are mounted on all sides for laser measurements.

The reactor quarl section is made of plexiglas to facilitate optical measurements close to the burner outlet. The quarl is submerged into the water tank such that the entire quarl is visible through the windows of the water tank. A perforated plate is attached to the quarl's underside to prevent water circulation above this area.

Scaling of the SSV4 burner head

There are two types of similarity that should be considered when up or down scaling fluid dynamic processes: geometric and dynamic similarity. Geometric similarity is simply that the physical construction must be similar. Dynamic similarity means that the phenomena are similar and is accomplished by modeling equivalent dimensional parameters.

The constructed burner is a down scaled version of the co-fired coal/straw burner used at Studstrupværket unit 4 (SSV4), Denmark. The aim was to construct an exact 1:5 geometrically down-scaled burner, however to use available pipes with standard dimensions some minor deviations from an exact 1:5 scaling was necessary. The burner is an axial vane swirl burner, where the second and tertiary outlets each have 12 spin vanes to control the swirl. The full-scale version has less spin vanes. A larger number is used in this facility to ensure axi-symmetric flow. Both outlets have baffles and sieve trays to distribute the fluid evenly in the pipe before it reaches the spin vanes. These elements are included only in the down-scaled version. A 3-dimensional representation of the burner head is shown in Figure 27.

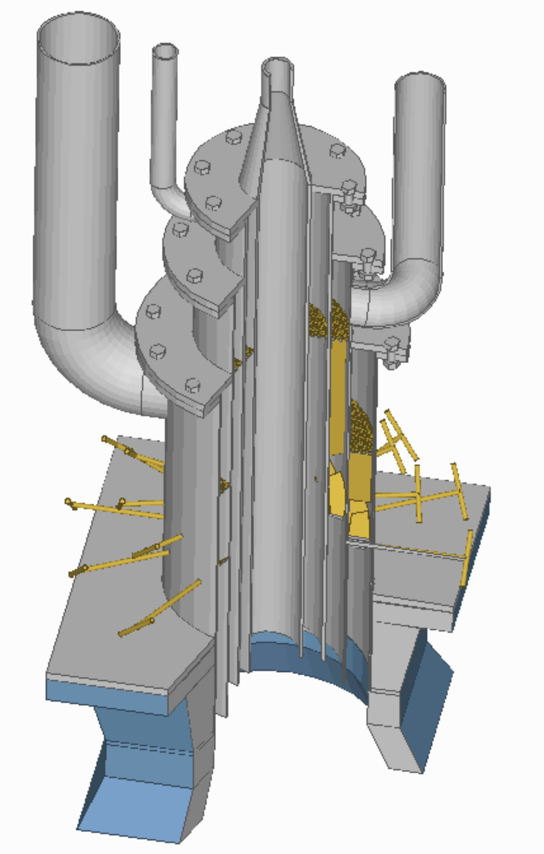

Figure 27 3-dimensional representation of the down-scaled burner head

The flow in the near burner region is in the fully turbulent regime and the fluid dynamics is primarily governed by the ratio of the momentum fluxes in each of the inlets. Therefore the individual inlet flow rates were determined based on the momentum flux ratios in the full-scale SSV4 burner. Water was used in the down-scaled version instead of air, and the ratio between the absolute momentum flux in the test facility and the full-scale burner was 1:5. Typical mass-flow data from the full-scale burner at SSV4 were used as basis for the down-scaling.

Considerations regarding optical access and seeding

To allow optical access to the near burner region the tank below the burner head was built with plexiglas windows on all sides. On two perpendicular sides in the top section large windows were used to allow Particle Image Velocimetry (PIV) measurements to be made. On the remaining sides smaller windows were used to maintain structural strength of the tank. An outline of the tank is shown in Figure 28.

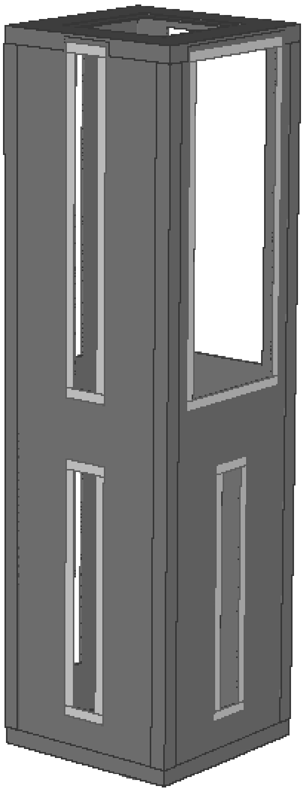

Figure 28 Outline of the tank in which LDA measurements were made

In Laser Doppler Anemometry it is important that the seeding particles follow the flow, not only the mean flow but also the fluctuations. The procedure of finding the frequencies for the smallest vortices represented by the Kolmogorov scales and the corresponding particle size and density that ensure the particle is able to follow these whirls, was described by Albrecht (Albrecht, et al. 2003). The same procedure was used in this work to find the required particle parameters for the test-rig, for further details refer to appendices A and B. From these calculations it was concluded that 5 μm polyamide particles were able to follow all turbulent fluctuations whereas 20 μm polyamide particles were only capable of following the turbulence when the mean velocity is below around 0.4 m/s. It was decided to use the 20 μm polyamide particles because the light reflection from the 5 μm particles was insufficient to get a reasonable data collection rate. From the measurements presented in section 1.3.3 it is clear that indeed the velocity is below 0.4 m/s in the large majority of the reactor.

1.3.2 Apparatus and data acquisition

A commercial laser Doppler Velocimetry system from Dantec Dynamics was used to measure time averaged and instantaneous velocities with a 400 mm lens. The system has four laser beams for 2-dimensional measurements. Measurements were made in the plane indicated in Figure 29.

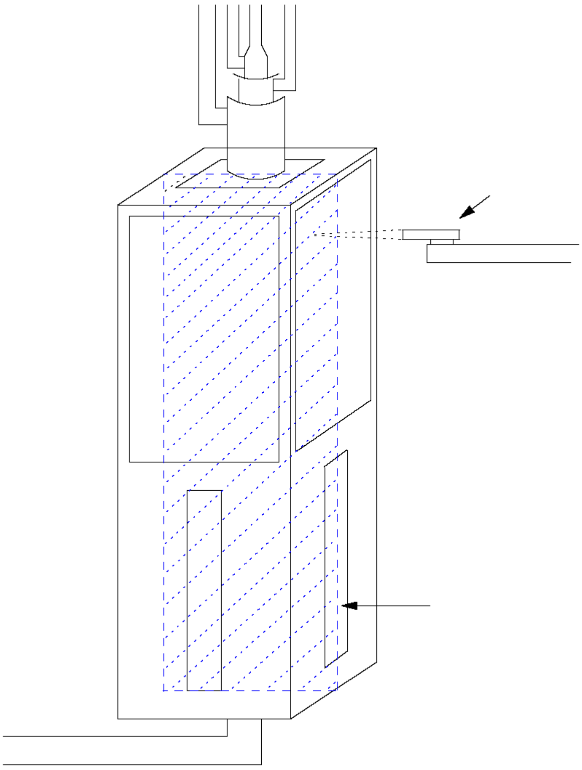

Figure 29 Schematic illustration of the tank showing the plane for LDA measurements

A LabView control system was developed to regulate the opening of the four valves that determine the flow in each of the inlet streams. The correlation between pressure difference over the valve and the flow rate was determined initially using the electro-magnetic flow meter as described in further detail in (Berg 2006).

1.3.3 Experimental data

During the experiments both the secondary and tertiary outlet spin vanes were oriented 45° to the main direction. The corresponding swirl number can be approximated as:

$$S = \frac{2}{3}\left[\frac{1-(d_h/d)^3}{1-(d_h/d)^2}\right]\tan\phi \qquad (1)$$

where φ, d, and d_h are the spin vane angle, nozzle hub diameter, and vane pack hub diameter, respectively. This relationship follows from assumptions of plug flow axial velocity in the annular region, and very thin vanes at constant angle φ to the main direction. According to this formula the swirl number for both the secondary and tertiary inlets is 0.94.

Measurements were made along five horizontal lines from the axial centre of the tank to the wall in the upper part of the tank. The lines were 41.7 mm, 104.3 mm, 313 mm, 500.9 mm and 782.6 mm from the quarl outlet. The measurement time in each location was 10 min, with the exceptions of 8 locations in top of the reactor where it was only 5 min. There were good sampling rates close to the window, but the rate dropped considerably in the inner part of the reactor. Close to the window approximately 2100 samples were collected during ten minutes, and in the centre of the tank only 500–600 samples were obtained. With a measuring time of 600 s and the applied dead-time of 0.120 s, it should be possible to obtain 5000 samples with optimal seeding and a validation rate of 100%. Impurities in the water may be one of the reasons for the reduced validation rate.

Figure 30 shows the measured profiles of time averaged axial and tangential velocities as well as the RMS axial velocity.

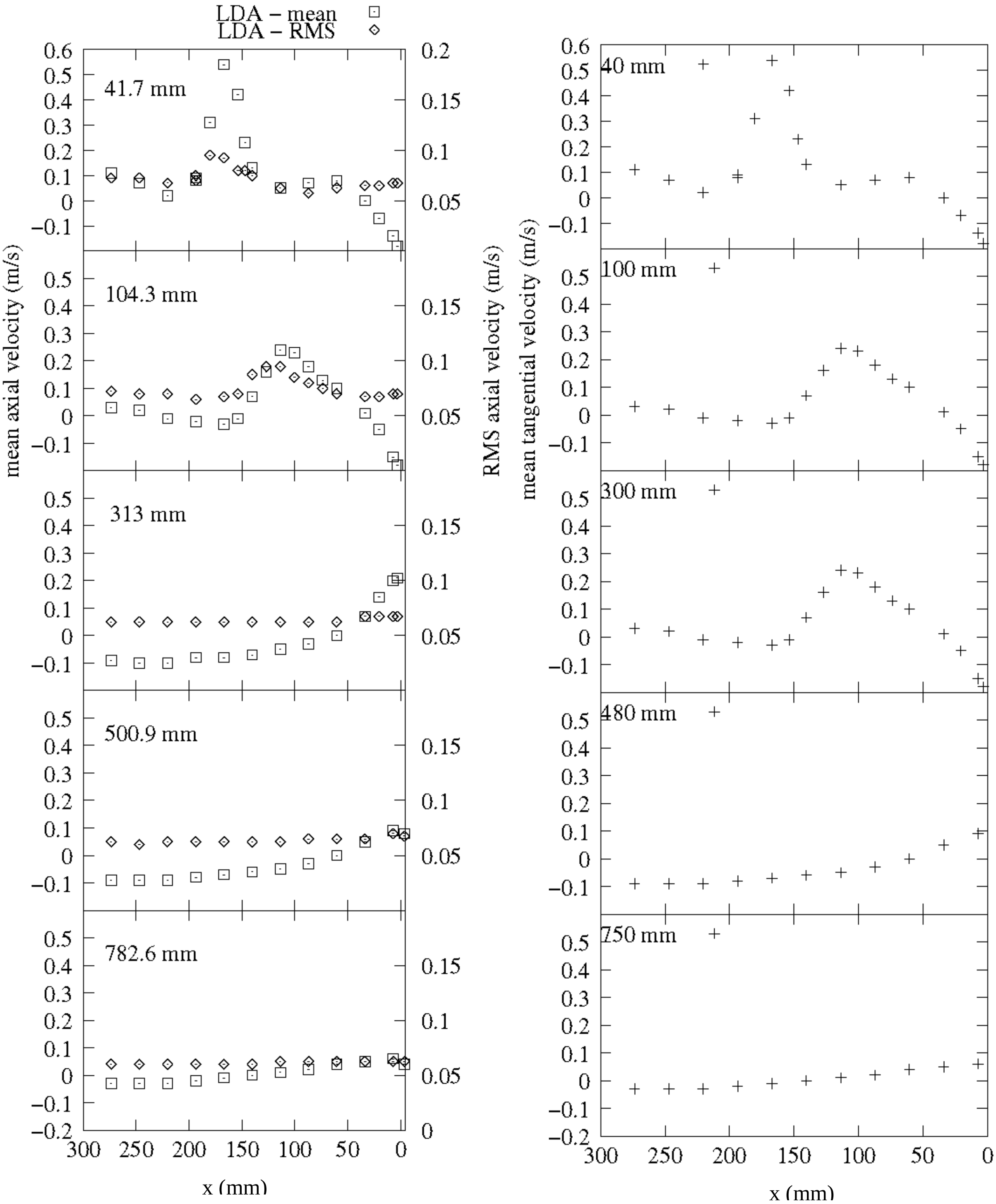

Figure 30 *Time-averaged and RMS axial velocity (left) and tangential velocity (right) measurements.*

As seen from Figure 30 the velocity only exceeds 0.4 m/s in a narrow region at the location of the secondary and tertiary inlets. Overall, the flow is also seen to exhibit the same characteristics as those in a swirl stabilized burner. Further discussion of the measurements is presented in Section 3.1.2, where comparison with the CFD predictions is made.

Additional measurements with different swirl settings and mass flow ratios between the four inlets were desirable. However, a large amount of time was spent solving problems that caused poor data rates in the measurement which precluded further measurements to be made within the timeframe of the project. The main source of these problems was found to be associated with the seeding. The attempts made with the 5 μm particles were unsuccessful as mentioned above. Reasonable data rates were eventually obtained with 20 μm particles when a suitable additive (ethanol) was used to prevent agglomeration of the seeding particles and extreme caution was taken to prevent initial impurities in the water.

1.3.4 Summary and Conclusions

A substantial amount of work was spent designing and building a test facility that allows the swirl angles and flow rates to be set independently in each inlet and at the same time facilitates optical access to a large portion of the primary flow field including the quarl area.

Overall, the testing was very successful as a high quality dataset was collected that clearly demonstrates the usefulness and capabilities of the test facility. This is further supported by the excellent agreement with model simulations demonstrated in Section 3.1.2 of this report. Unfortunately, only one operating condition was tested using the LDV system within the timeframe of this project.

A large amount of time was spent solving problems that caused poor data rates in the measurement which precluded further measurements to be made within the timeframe of the project. The main source of these problems was found to be associated with the seeding. The attempts made with the 5 μm particles were unsuccessful as mentioned above. Reasonable data rates were eventually obtained with 20 μm particles when a suitable additive (ethanol) was used to prevent agglomeration of the seeding particles and extreme caution was taken to prevent initial impurities in the water. Additional measurements with different swirl settings and mass flow ratios between the four inlets were desirable.

Further testing based on the established facility is important with respect to the development and validation of advanced time dependent CFD modeling capabilities based on Large-Eddy-Simulation and similar methods and to gain improved fundamental understanding of near burner aerodynamics. These are however all considered to be activities that can support further development of the cofiring technology on a medium to long term. On the short to medium term these activities are of secondary importance compared to the further development of a reliable particle conversion model and demonstration of the current modeling capabilities to pilot- and full-scale combustion processes.

2. Task 2: Model development

The overall objective of Task 2 is to develop the two CFD-based models that represent some of the primary deliverables from this phase of the proposal and to develop advanced graphics capabilities that allow intuitive visualization of the results.

2.1 Development of CFD sub models

The objective of this task was to adapt the commercial CFD code FLUENT™ to accommodate biomass cofiring combustion features. The primary focus was put on the development and implementation of a particle conversion model that accounts for the non-isothermal and non-spherical effects that are associated with the combustion of relatively large biomass particles. An accurate description of these effects is crucial for the ability to model a wide range of associated processes including volatiles release, carbon burnout, ash deposition and formation of harmful emissions. The work at Aalborg University focused on the implementation in CFD whereas a parallel project at Brigham Young University generated experimental data and model predictions with a stand-alone code (Lu 2006).

Issues related to further development of an existing ash behavior and deposit formation model were given less attention than planned for several reasons. 1) The particle temperature and conversion prediction has a direct impact on the deposition rate prediction hence the existing deposition model will benefit directly from the improved particle model 2) Sufficient information to improve the ash chemistry description is not yet available 3) Data that will support this development is being generated under the project PSO2003-4766 and hence it was found that this development is more efficiently dealt with under the project PSO2003-4881.

2.1.1 Non-isothermal particle conversion

Biomass, and straw in particular, is much less friable than coal and it is not feasible to grind it to particle sizes comparable to pulverized coal in traditional coal mills. This poses new challenges in the CFD modeling of these combustion systems. Historically, the combustion modeling capabilities in commercial CFD codes have been focused on coal combustion. In terms of combustion behavior, there are significant differences between biomass and coal. Some of these include:

non-spherical particle shapes (impacts motion and combustion rates)

particle size (impacts the conversion processes)

Traditional coal combustion models are based on the assumption that internal gradients in temperature and composition are negligible. This assumption, however, does not hold for typical biomass particle sizes. This can be illustrated by the Biot number, which is often significantly larger than the limit of about 0.2 where internal transport processes start to become limiting for heat and mass transfer. Consequently, internal gradients must be accounted for to accurately predict biomass particle conversion and related processes.

The conversion of large particles is fairly well understood and numerical models are described in the literature (Di Blasi 1996), (Lu 2006), (Bryden and Hagge 2003) and (Bryden, Ragland and Rutland, 2002) but have not been included in CFD codes. Focus in this task was on the implementation of a 1-dimensional particle conversion model in the commercial CFD code

FLUENT™. The current implementation of the model includes a 1-dimensional discretization of internal:

1. Temperature gradients
2. Drying, devolatilization and char oxidation rates
3. Composition variations during conversion

The resulting 1-dimensional model framework is illustrated conceptually for a wood chip in Figure 31 with the discretization of the smallest dimension indicated.

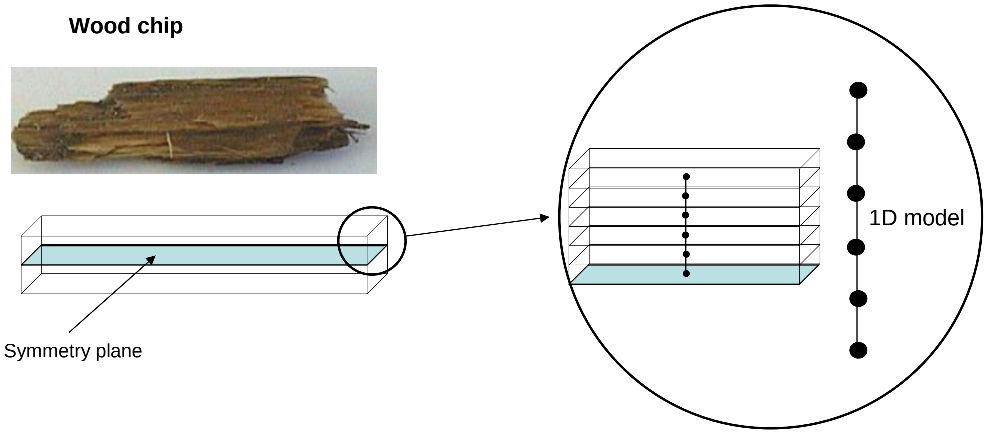

Figure 31 Conceptual illustration of the discretization used for a wood chip.

More detailed calculations were also performed at Aalborg University with a stand-alone model that was decoupled from the CFD code (S. K. Kær, L. Rosendahl, et al. 2005). The objective with this code was to test a more sophisticated approach that included internal pressure and flow distributions as well as species transport equations (Kær, et al. 2005). From these simulations the following conclusions were drawn: 1) the calculation time for a single particle conversion simulation with this model exceeds what is realistic in the context of a CFD simulation unless the calculation algorithm can be made more efficient 2) The added complexity did not lead to results significantly different from the simpler model.

Detailed experimental and modeling investigations of biomass particle conversion was undertaken at Brigham Young University in parallel with the activities at Aalborg University. A detailed description of the work at Brigham Young University is found in (Lu 2006). The experimental data generated are unique internationally with respect to the range of particle types and shapes investigated. In spite of unavoidable experimental difficulties, the data are considered to form the best possible foundation for detailed model validation. The work of (Lu 2006) also included development and validation of a 1-dimensional model based on concepts similar to those described in (Kær, et al. 2005) but with additional physical processes included. The overall conclusion from this work was that: 1) internal gradients cannot be disregarded if the characteristic particle size exceeds 100 µm 2) a 1-dimensional model offers great improvements over a traditional 0-dimensional model 3) particle shape effects are relatively well captured by the 1-dimensional model if a spherical, flake or cylindrical shape representation is used.

Rather than reproducing this comprehensive set of model predictions and undertaking a similar comparison to the experimental data, the CFD implementation has been initiated using the same model foundation, although with reduced complexity, in the current version of the model. The foundation of the CFD implementation is summarized in the next subsection.

Mathematical foundation

The thermal mass of the gas is small compared to that of the solid in the particle and can be neglected in the energy equation. The lumped gas and solid energy equation is thus given by:

$$\frac{\partial(\rho_S i_S)}{\partial t}+\frac{\partial(h_G\,\rho_G\,u_G)}{\partial y}=\frac{\partial}{\partial y}\left(k_{eff}\,\frac{\partial T}{\partial y}\right)+\sum\Delta h_i^0\dot{\omega}_i \tag{2}$$

where ρ_S , i_S , h_G , ρ_G , k_{eff} , Δh_i^0 represent the mass fraction averaged density of the solid matrix, the internal energy, the enthalpy of the gas mixture, the density of the gas mixture, the superficial gas velocity, the effective thermal conductivity and the heat of formation of species i, respectively. The governing energy equation was solved by the finite-volume method. The TDMA algorithm was used to solve the resulting tri-diagonal matrices. The overall solution algorithm for the detailed model is shown in Figure 32. For the CFD version of the model, the pressure field, velocity field, and species transport steps were omitted.

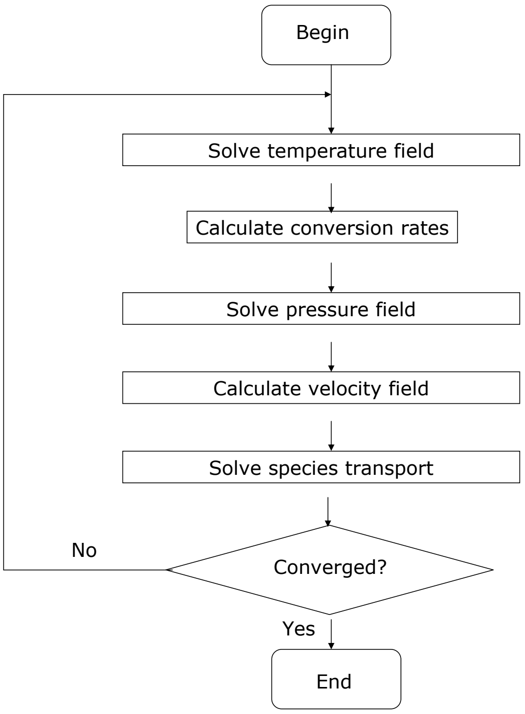

Figure 32 Outline of the calculation algorithm used in the 1D model.

At the particle centre point a zero gradient condition is applied to represent a symmetry plane. At the particle surface, the heat transfer rate due to convection and radiation is used as boundary condition. The combined heat transfer rate is given as:

$$Q_p=hA_p(T_\infty-T_p)+\varepsilon_p A_p\sigma(\theta_R^4-T_p^4) \tag{3}$$

in which, h , A_p , T_∞ , T_p , ε_p , σ , and θ_g represent convective heat transfer coefficient, particle surface area, local fluid temperature at the particle position, particle temperature, particle emissivity, Stefan-Boltzmann constant, and radiation temperature, respectively. The heat transfer coefficient, h, is calculated by $Nu = hd_p / k_g = 2 + 0.6\mathrm{Re}_p^{1/2}\,\mathrm{Pr}^{1/3}$, where k_g and Pr are thermal conductivity and Prandtl number of the fluid, respectively.

Drying is modeled using an Arrhenius expression with a pre-exponential factor of 5.13×10^{10} s^{-1} and an Activation energy of 88 kJ/mol as suggested by (Bryden and Hagge 2003).

When the local temperature inside the particle reaches the devolatilization temperature, release of volatiles begins. The homogeneous combustion of volatiles takes place once they are released from the particle surface and is included in the CFD based furnace simulation. A single-rate kinetic devolatilization model is used to predict the volatiles yield rate, which assumes that the rate of devolatilization is dependent on the amount of volatiles remaining in the particle via a first-order reaction:

$$-\frac{dm_p}{dt} = k\left(m_p - (1 - f_{v0})m_{p0}\right) \tag{4}$$

where k, f_{v0} and m_{p0} denote the kinetic rate, the mass fraction of the volatiles that are initially present in the particle, and the initial particle mass, respectively. The kinetic rate k is defined by the input of an Arrhenius-type, pre-exponential factor and an activation energy. The rate is calculated locally for each computational node.

Currently, it is assumed that char oxidation does not begin until the volatiles of a particle are completely evolved. This is based on the idea that moisture and volatiles leaving the particle effectively prevent oxygen from diffusing into the particle. Because of the large biomass char particle diameter, the diffusion-limited surface reaction rate model is used:

$$\frac{dm_p}{dt} = -A_p D_{ox} \frac{\rho_f \, RT_\infty Y_{ox}}{M_{w,ox}} \tag{5}$$

where D_{ox} and Y_{ox} represent the diffusion coefficient of oxygen in the bulk gas and the local mass fraction of oxygen in the gas, respectively.

Single particle conversion patterns

The difference between particles with low and high Biot numbers respectively is illustrated in Figure 33 showing the moisture and volatiles mass fractions as a function of conversion time.

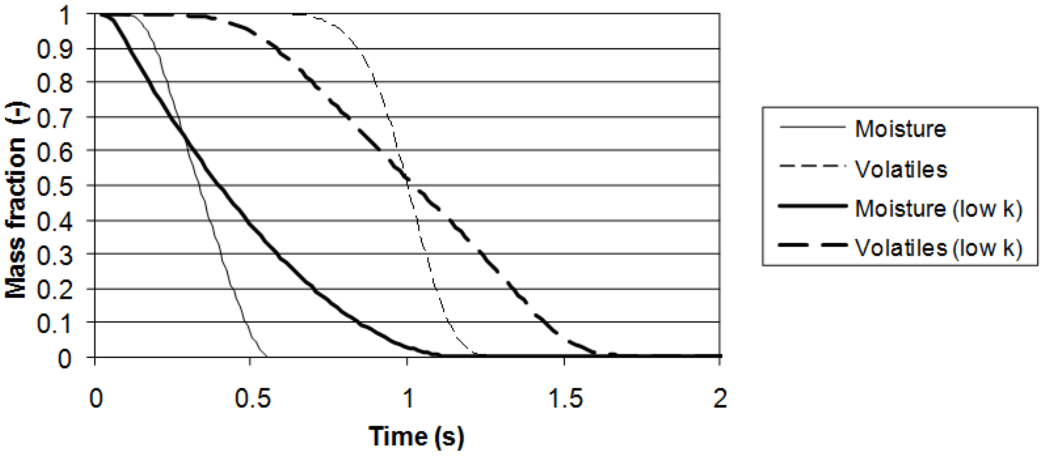

Figure 33 Moisture and volatiles mass fractions as function of conversion time for particles with high and low Biot numbers, respectively.

It is seen that the particle with high Biot number (labeled low k) undergo drying and devolatilization simultaneously. For the low Biot number particle on the other hand, the processes are sequential. The total conversion times are comparable but moisture and volatiles are released at different times. The isothermal particle is converted faster due to the fact that the surface temperature of this particle remains low and consequently the heat transfer rate from the gas is high compared to the non-isothermal case where the particle surface heats up after drying.

To illustrate the influence from particle shape on the conversion process, the mass fractions of moisture and volatiles were calculated as a function of time for three particles with the following characteristics:

1. A cylindrical particle with a diameter of 3 mm and a length of 30 mm (a typical straw shape)
2. A spherical particle with the same diameter as the cylinder but much smaller volume
3. A spherical particle with the same volume as the cylinder but significantly larger diameter

In all cases the particles are introduced into a 1200°C hot gas with an initial particle temperature of 50°C.

Figure 34 shows the result for the cylindrical particle.

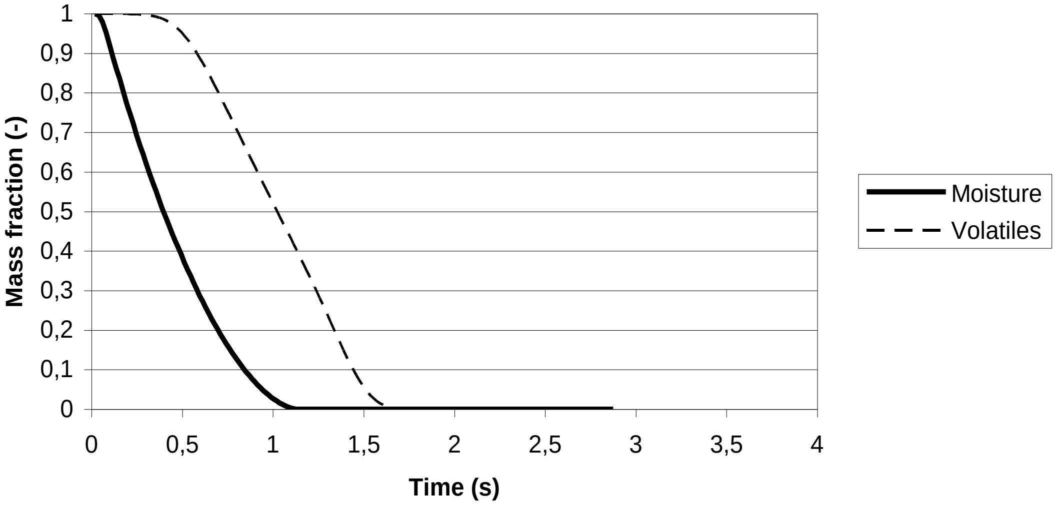

Figure 34 Predicted conversion of a 3 mm diameter 30 mm long cylinder.

For the first case of a cylindrical particle with a diameter of 3 mm and a length of 30 mm, the volatiles are completely evolved after approximately 1.5s. Drying initiates at the surface almost instantaneously and devolatilization begins after about 0.5s. The conversion of a sphere with the same diameter is presented in Figure 35

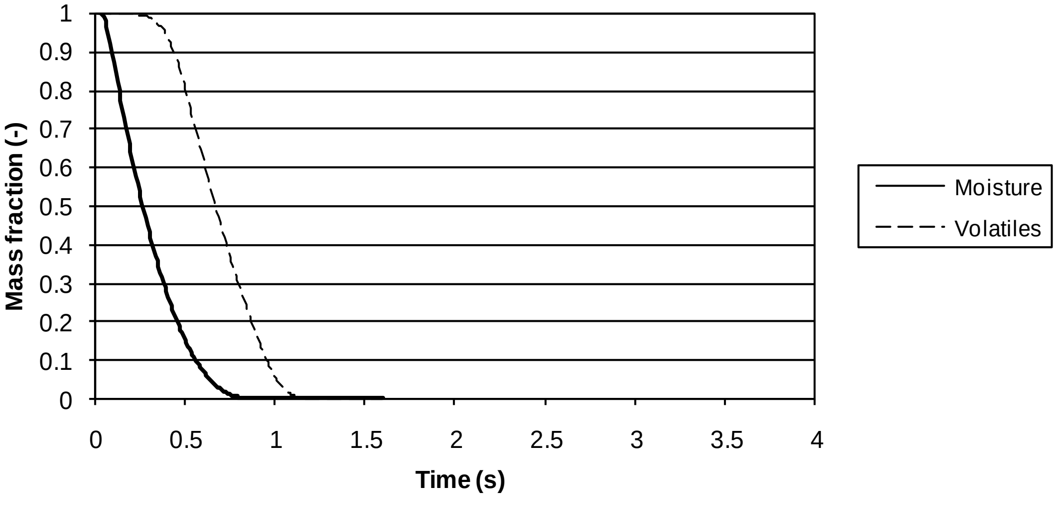

Figure 35 Predicted conversion of 3mm diameter sphere.

It is seen that the sphere is converted faster than the cylinder; however, it must be kept in mind that the volume of the sphere is 15 times smaller than that of the cylinder. Also the conversion processes are seen to be more sequential compared to the cylinder. If the volume of the spherical particle is chosen equal to the cylinder the corresponding diameter is 2.5 times that of the cylinder. The conversion profiles for this particle are shown in Figure 36.

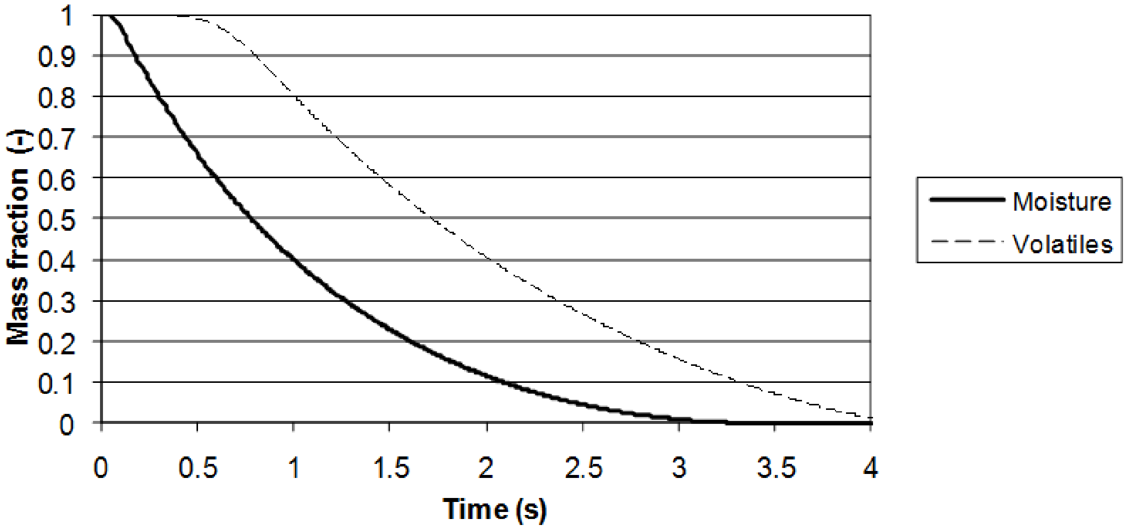

Figure 36 Predicted conversion of a sphere with the same volume as the cylinder presented in Figure 35.

The total conversion time for the equi-volumetric particle is seen to be approximately 3 times that of the cylinder. Also it is seen that non-isothermal effects are now distinct with drying and devolatilization occurring with the devolatilization lagging about 0.5s behind the drying.

From the results presented so far, it can be concluded that non-isothermal effects can have a pronounced influence on the drying and devolatilization behavior of a particle. It has also been demonstrated that the particle shape is important. A non-spherical particle cannot be represented by a sphere of equal diameter or volume without significant errors in terms of the predicted conversion behavior. This is even more so if diffusion controlled char oxidation is taken into account as well because the different processes scale with the diameter to the power of one (flake), two (cylinder) and three (sphere), respectively.

To demonstrate the internal variations in particle properties predictions were made for a flake-like geometry represented by a 1cm thick plate geometry with the thickness being the characteristic dimension.

Figure 37 shows the predicted release rates of moisture and volatiles and corresponding gas velocities in the porous particle at a conversion time of 5.1s. It is seen that the drying front is followed closely by the devolatilization front. When the moisture has completely evaporated in a region, the temperature of the remaining solid increases to the devolatilization temperature of approximately 200°C. The influence from the moisture and volatiles release on the gas velocity is also clearly seen. As the devolatilization front moves towards the symmetry plane at the particle centre, the gas velocity may still increase in outer regions of the particle where no mass release takes place due to density changes caused by temperature variations.

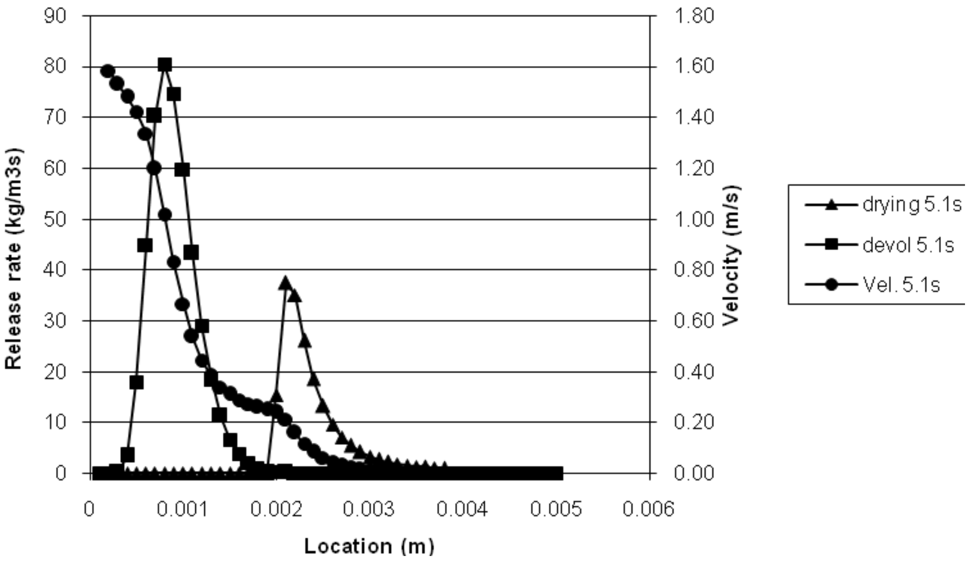

Figure 37 Drying and devolatilization rates for a flake with corresponding gas velocity.

2.1.2 Ash deposition

The modeling of ash deposition and the related impact on heat transfer rates in the boiler was based on the framework described in detail in (Kær, Rosendahl and Baxter, Towards a CFD-based Mechanistic Deposit Formation Model for Straw-fired Boilers 2006). The existing framework is based on a mechanistic description of the main deposition processes:

1. Condensation
2. Thermophoresis and turbulent eddy impaction
3. Inertial impaction

This mechanistic description was originally developed for straw firing in grate based boilers but is also considered valid under cofiring conditions. The ash and heat transfer mechanisms are indicated in Figure 38 for a typical deposit from straw firing.

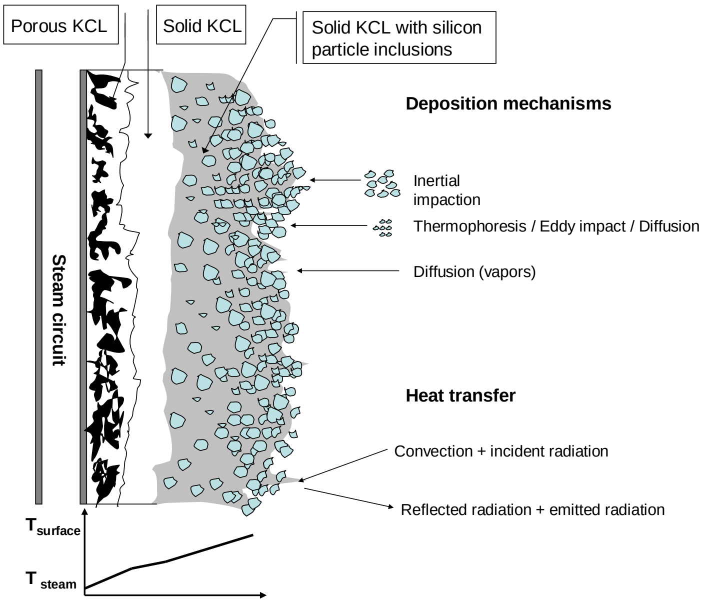

Figure 38 Conceptual deposit structure from straw combustion.

The quasi-stationary modeling approach

The characteristic time scale associated with deposit build-up is much greater than the time it takes to establish a stationary temperature profile across the deposit as well as the time scales of the flow and combustion processes. Therefore, a quasi-stationary modeling approach is used to describe the time evolution of the processes in the furnace caused by deposit accumulation. The flow chart presented in Figure 39 outlines the approach.

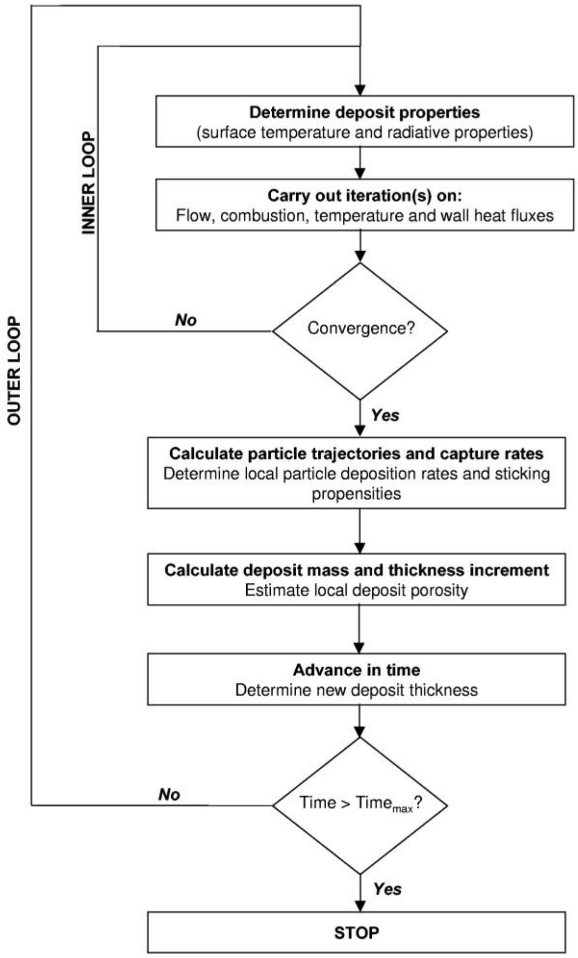

Figure 39. Flow chart illustrating the quasi-stationary modeling approach to determine deposit accumulation on heating surfaces.

Ash release and transformation

With respect to cofiring, it is important to notice the interaction between biomass (straw) and coal ashes is not accounted for. In particular the interaction between the non-volatile coal ash, and the volatile components K, Cl and S significantly changes the behavior of the two fuels compared to when fired alone. A quantitative understanding of these interactions has not yet been established to the extent where the main reactions and their corresponding rates exist. Extension of the model in this area is pending expected results from ongoing fundamental experimental work (ELTRA PSO4766).

The accumulation of ash on the heating surfaces is a two step process; transport to the heating surface by the mechanisms mentioned above followed by sticking to the heating surface. The latter step depends on the stickiness of the ash arriving at the surface and the stickiness of the existing deposit surface. The stickiness of the ash particles is strongly influenced by the temperature and hence benefit directly from the improved particle temperature prediction resulting from the development described under Section 2.1.1 as outlined in the next subsection.

Ash sticking propensity

The subject of ash sticking propensity has been given considerable attention in the literature, however, so far no generally accepted modeling methodology has been developed, especially not focusing on conditions typical for biomass combustion. The sticking propensity is a complex function of particle and deposit surface structure and viscosity, impaction angle and velocity and the fraction of molten material at the surfaces. In mechanistic modeling approaches to ash deposition in coal combustion, the most frequently used approach is that of (Walsh, et al. 1990). The net fraction of particles contributing to deposit growth is modeled as:

$$\chi_{sticking} = \underbrace{p(T_p)}_{sticky\, particles} + \underbrace{\big(1-p(T_p)\big)\, p(T_s)}_{sticky\, deposit\, surface} - \underbrace{\big(1-p(T_p)\big)\big(1-p(T_s)\big)}_{erosion\, by\, non-sticky\, particles} \tag{6}$$

The third term on the right hand side accounting for erosion of the deposit by non-sticking particles is currently not used as there is no well-established mechanistic model available that is able to predict the complex mechanisms removing deposited material. In the original work of (Walsh, et al. 1990) particle viscosity was suggested as the parameter with the most significant influence on sticking propensity. The sticking propensity was assumed inversely proportional to the viscosity with perfect sticking below a certain critical viscosity:

$$p(T) = \begin{cases} \eta_{ref}/\eta & \eta > \eta_{ref} \\ 1 & \eta < \eta_{ref} \end{cases} \tag{7}$$

The compositional and temperature dependence of the viscosity can be determined from correlations suggested in the literature. A brief discussion of a general model for calculating viscosities of general furnace, converter or ladle slags is given below. It is not suitable for mould fluxes. The model is semi-empirical and uses "A" and "B" parameters to calculate the viscosity (η) as follows: (note: viscosity is in Poise)

$$\eta = \mathrm{A\,T} \exp\left[\frac{1000\mathrm{B}}{\mathrm{T}}\right] \tag{8}$$

where T is the temperature in Kelvin. The A and B parameters are derived by dividing the slag components into three categories:

Glass formers (X_G):

$$\mathrm{X_G = X_{SiO_2} + X_{P_2O_5}} \tag{9}$$

Modifiers or fluxes (X_M):

$$\begin{aligned}\mathrm{X_M} = {} & \mathrm{X_{CaO} + X_{MgO} + X_{Na_2O} + X_{K_2O}} + \\ & \mathrm{3X_{CaF_2} + X_{FeO} + X_{MnO} + 2X_{TiO_2} + 2X_{ZrO_2}}\end{aligned} \tag{10}$$

Modifiers or fluxes (X_A):

$$\mathrm{X_A = X_{Al_2O_3} + X_{Fe_2O_3} + X_{B_2O_3}} \tag{11}$$

Where X represents mole fraction.

The model does not allow for presence of solid phases (for instance $2CaO.SiO_2$) and thus assumes the slag is fully liquid at the temperature chosen. If this is not the case and some solid phase(s) are present, the actual viscosity will be higher than the model predicts. It is possible to estimate the "effective" viscosity of slags containing solids using the formula below, where the amount of solid phase is known.

$$\eta_e = \eta\left(1 - 1.35\,\Theta\right)^{-5/2} \tag{12}$$

where:
η_e = effective viscosity of slag
η = viscosity of the molten slag
Θ = fraction of precipitated solid phases

From the above discussion of particle stickiness it is evident that the particle surface temperature upon impaction is a key parameter concerning the rate of deposit accumulation. The detailed prediction of the internal particle temperature distribution and the associated influence on the particle surface temperature offers a significant improvement of the predicted particle stickiness.

2.1.3 Summary and Conclusions

This task has focused on extending the modeling capabilities of the commercial CFD code FLUENT™ to accommodate cofiring combustion features. This subsection summarizes the main achievements and outlines future research.

The ability to account for particle size (non-isothermal) and shape effects represented the area in which improvements to the existing models were most critical as it impacts largely all other processes in the furnace. A novel one-dimensional model was developed based on information from the literature and extensive experimental tests undertaken at BYU. The implementation of an advanced particle conversion model in CFD is unique internationally and constitutes the main achievement with respect to model development. Currently, the model is operational and the first tests were made showing substantial improvements over the existing models. Demonstration of the model to pilot and full-scale will be the next step including optimization of the numerical calculation procedures to improve speed and robustness. The model demonstration to pilot and full-scale is part of the activities under PSO4881 and further optimization of the model based on the experience gained will be the focus of PSO7333.

Regarding the validation of particle dynamics (velocities, size and shape changes), the prediction of velocities was based on drag coefficients modified for non-spherical particle effects and the size changes during combustion was modeled without addressing possible shape changes. Direct validation of the particle dynamics was not possible based on the experimental data that does not include particle sampling. An assessment of particle motion in particular will be included in PSO4881 based on the pilot scale measurements and at full-scale in PSO7333.

With respect to ash behavior, the release of potassium from the straw was included in the deposition model. In addition, the ash stickiness predictions were extended to include both biomass and coal derived ashes using an ash viscosity model that accounts for the chemical composition. Detailed modeling of the interaction of potassium with the coal ash either in suspension or within the deposit is not included but considered an important topic for future development. However, currently the level of understanding is not sufficient to develop a mechanistic model. The activities in the remaining project period of PSO4881 will include a review of the results obtained in PSO4766 including an assessment of the potential for extending the deposition model based hereon.

Biomass and coal particle devolatilization and subsequent gas phase oxidation of the volatile gases was incorporated in the model considering the following gaseous species: CO, CO_2, CH_4, H_2 and H_2O. Using this approach, the substantially different off gas compositions of biomass and coal can be accounted for. Further development is not planned in this area.

2.2 Subtask 2.2: Engineering model development

The objective of this task is to develop an engineering model with the look and feel of a standard computer application that can be used to assess the impacts of fuel properties, boiler design, and boiler operation on boiler performance. This model will be based on concepts similar to those traditionally used for CFD calculations, but the interface, run times, and level of expertise required for use will be appropriate for a power plant engineer or similar user. The model will run under modern Windows-based operating systems for Intel-type processors.

Deliverables from this task include a working computer code that can be run on a typical engineering desktop or laptop computer. The code will include input and output interfaces and will converge within reasonable (less than 30 minute) running times for typical applications. All coding will be done in object-oriented C++.

In agreement with PSO, this task was eliminated from this project.

2.3 Subtask 2.3: Graphical visualization for engineering model development

The objective of this task was to convert the model described under Subtask 2.2 to an appropriate (probably Unix) platform and develop an advanced visualization tool for displaying three-dimensional data from the engineering model in rooms specifically designed for such displays. The plan was to use Silicon Graphics hardware and software (OpenGL) to develop these displays.

Deliverables from this task were to include a three-dimensional projection of the results from the model to be developed under Subtask 2.2 and an interface to allow intuitive investigation of boiler properties and their changes with changing fuel, operation, or design.

In agreement with PSO, this task was eliminated from the project, and there is no current plan to readdress this development.

3. Task 3: Validation of CFD models

The objective of this task is to verify model performance by comparison to mostly existing data related to critical sub models. Verification of model performance at the systems level will be conducted under Subtask 4.2 and in Phase 2 of this project. The verification of the models will take place in three steps/levels, each of which forms its own subtask.

This task involves two subtasks, Subtask 3.1 involving validation of reaction sub models and Subtask 3.2 involving validation of flow field predictions. The flow field and reaction sub models jointly influence each other. These are discussed below in the opposite order (Subtask 3.2 first) since the flow field validations were done in some cases under non-reacting flow conditions whereas the reaction predictions always impact the flow field results.

3.1 Subtask 3.1: Validation of flow field predictions

The main objective of this subtask was to investigate the ability of the fluid mechanical sub models to correctly predict the dependence of the flow field on for example air staging, pneumatic injection of biomass and burner design. The focus of this task was put on comparison with data from the Burner Flow Reactor, including new data and previously collected data, and new measurements from the AAU cold flow facility. In the last case, two of the most widely used Reynolds averaged Navier-Stokes (RANS) based turbulence models were compared.

3.1.1 Comparison to data from the BFR

Cold flow gas velocities were measured in the BFR and reported by (Pickett, Jackson and Tree 1999). These measurements were used to assess the accuracy of the CFD flow field predictions. The overall purpose of this is to decouple the modeling uncertainties associated with the reacting flow calculations from the basic gas velocity prediction. When the reacting flow predictions are compared to measurements in section 3.2 to evaluate the developed reaction sub models, it is to some extent possible to account for the uncertainty that stems from the flow field description.

Modeling of the block swirler

The swirling flow in the BFR is generated with a moveable block swirler. Detailed CFD predictions of the flow field generated by the swirler were made for two reasons; firstly to evaluate whether the axial, tangential and radial velocity profiles are uniform around the circumference of the reactor at the exit of the burner and secondly it was attempted to combine the swirler model with the reactor model in one complete simulation. The latter unfortunately proved to be virtually impossible because of numerical instabilities and long simulation times. Figure 40 shows an outline of the swirler model and the predicted velocity magnitude at the outlet of the block swirler channels. The flow is seen to be of equal magnitude in each of the swirler channels. As the flow exits the channels localized jets form. These, however, do not persist to the entrance of the reactor quarl.

Predicted axial, tangential and radial velocity profiles at the reactor entrance are given in Figure 41. The setting of the swirl blocks required to produce a swirl number of 1.1 corresponding to the experiments was not known a priori. Consequently, the prediction turned out to correspond to a swirl number of 1.6. Changing the angle in the model would require rebuilding the geometry which was considered too time consuming in view of the additional information this would lead to. It can be seen that the profile shapes are very similar in the measurements and the predictions indicating that the inlet profiles can be taken from a CFD model if measurements close to the reactor inlet are lacking.

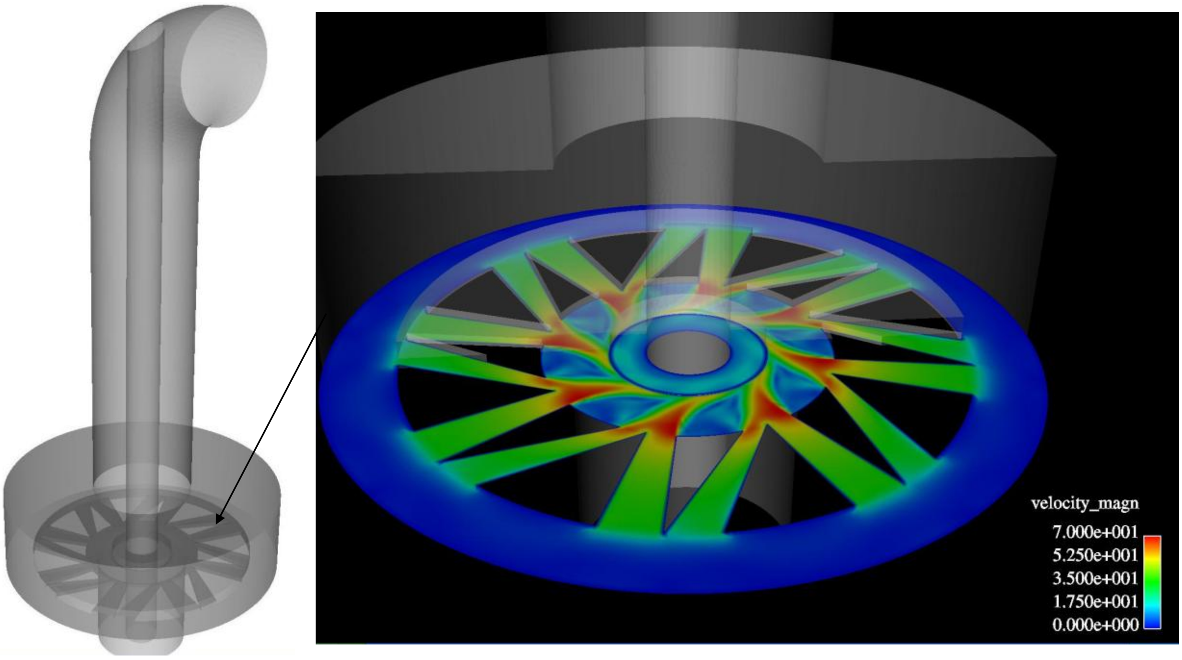

Figure 40 Illustration of the burner inlet CFD model including the block swirler

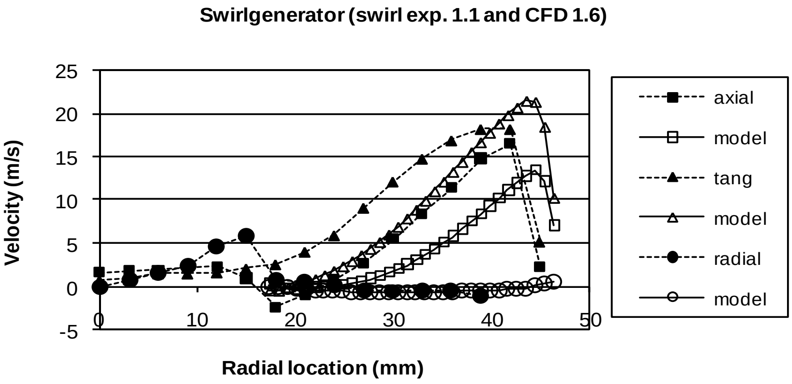

Figure 41 Predicted and measured velocity profiles at the reactor inlet. Please note the difference in swirl numbers

Predicted axial velocity profiles in the reactor

The predictions presented in this section were made with a grid consisting of 120,000 hexahedral cells and the QUICK differencing scheme. Calculations were also made with both the Upwind and the Higher Upwind schemes; however, the best agreement with measurements was obtained using the QUICK scheme. All model settings were kept at the default except the

Cμ constant of the standard k-ε model that was changed from the default value of 0.09 to 0.06. Standard wall functions were enabled.

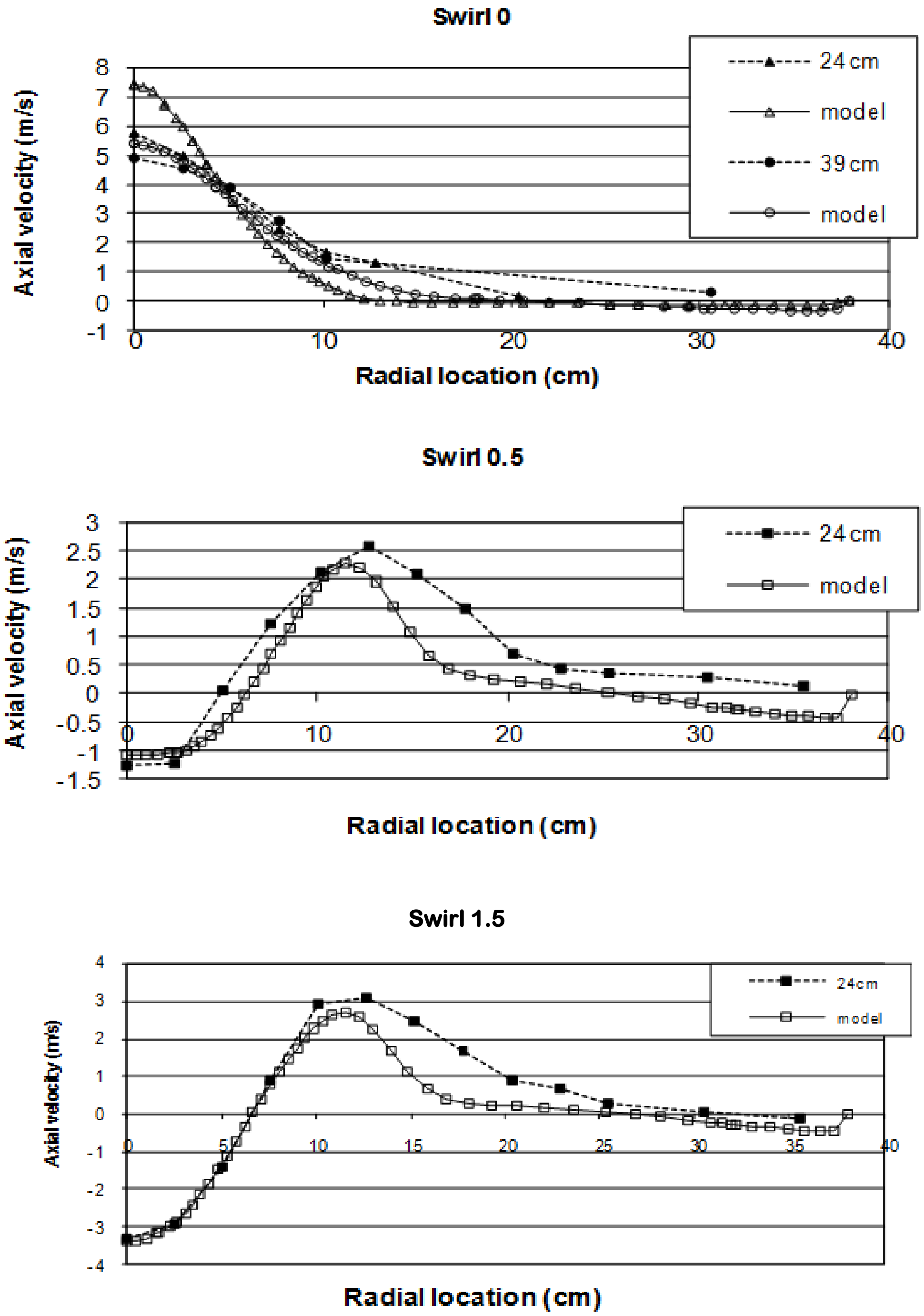

Figure 42 Predicted and measured axial velocity profiles at swirl numbers of 0 (top), 0.5 (middle) and 1.5 (bottom)

It is seen that the shape of the recirculation zone is well predicted judging from the agreement between measured and predicted axial velocities at a distance of 24 cm from the burner exit. The inner 10-12 cm of the profile is particularly well captured by the model. Further out the measured values are consistently higher than the predicted.

3.1.2 Comparison to data from the IET-AAU facility

The CFD predictions of the cold flow facility at AAU were made in two steps; the swirler was modeled in detail in the first step to provide boundary conditions for the reactor simulations in the second step. The first step was required since detailed measurements were not made at the burner exit that could be used as boundary conditions. An outline of the detailed CFD swirler model is presented in Figure 43.

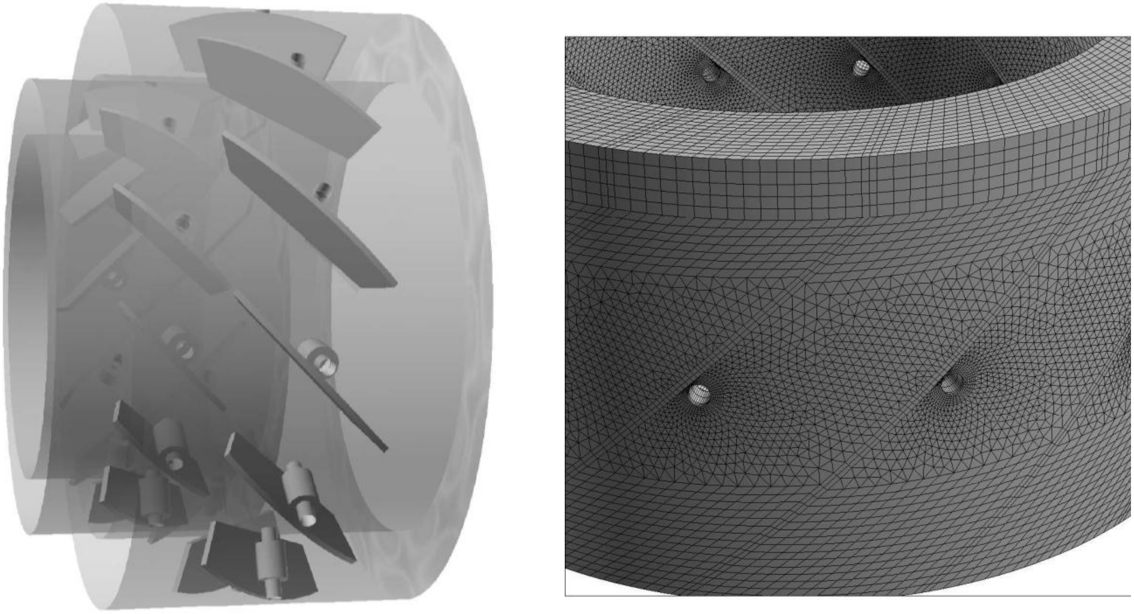

Figure 43 Graphical illustration of the detailed swirler model showing the details of the individual swirl vanes included in the model.

The influence from turbulence closure

In this section results are presented from comparison of cold flow predictions to experimental data from the cold flow test facility at IET-AAU. Figure 44 presents measured mean axial and tangential velocity profiles as well as turbulent kinetic energy compared with predictions based on the standard k-ε model. Please note that the reactor centerline is at x=300mm and the wall is located at x=0. The turbulent kinetic energy was calculated representing the radial component of the normal stress by the average of the axial and tangential normal stresses. Overall the agreement between measured and predicted quantities is very favorable. The location of strong velocity gradients and high turbulence intensities is also well captured. This is of great importance in reacting flow predictions as it represents the primary mixing and reaction zone.

Figure 45 shows similar results based on predictions with the RSM turbulence model. In this case the turbulent quantities which are represented directly by the axial and tangential normal stresses. The predicted mean axial velocity is in slightly better agreement with the measured values compared to the results from the k-ε model shown in Figure 44. The normal stresses however, are not so well captured in particular close to the burner. Direct comparison with the k-ε model is difficult since it only includes the turbulent kinetic energy.

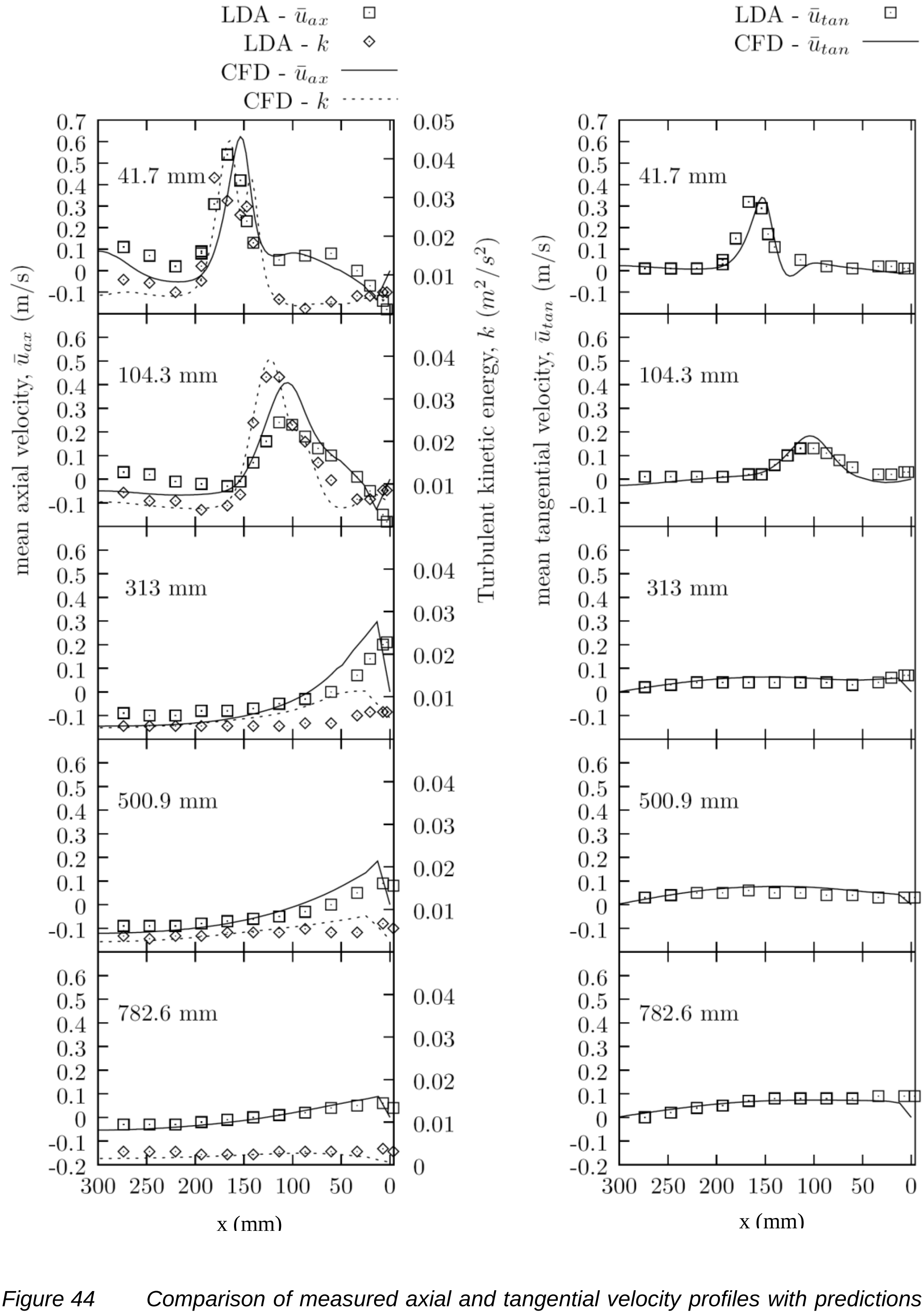

Figure 44 Comparison of measured axial and tangential velocity profiles with predictions from the k-ε turbulence model

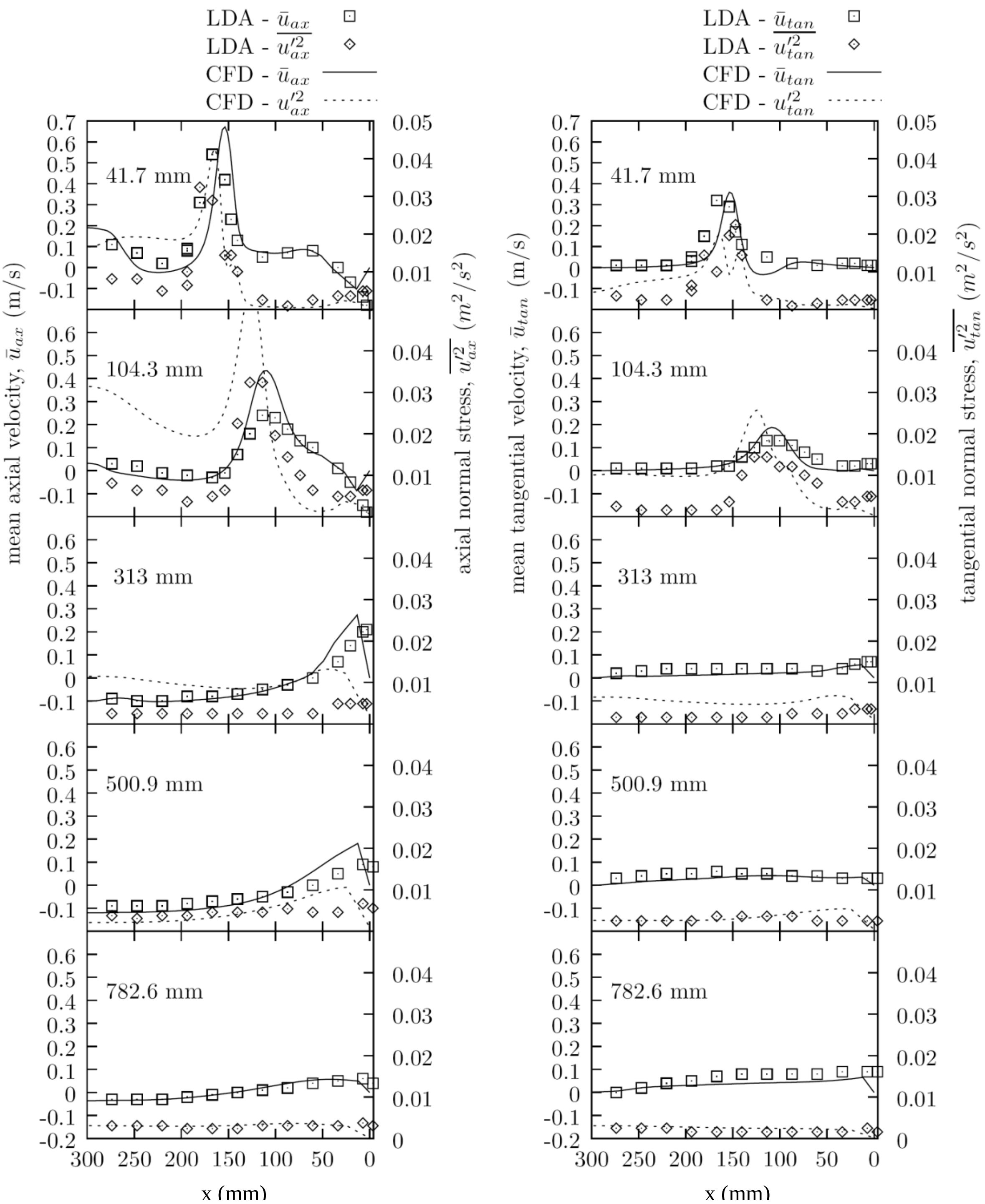

Figure 45 Comparison of measured axial and tangential velocity profiles with predictions from the RSM turbulence model

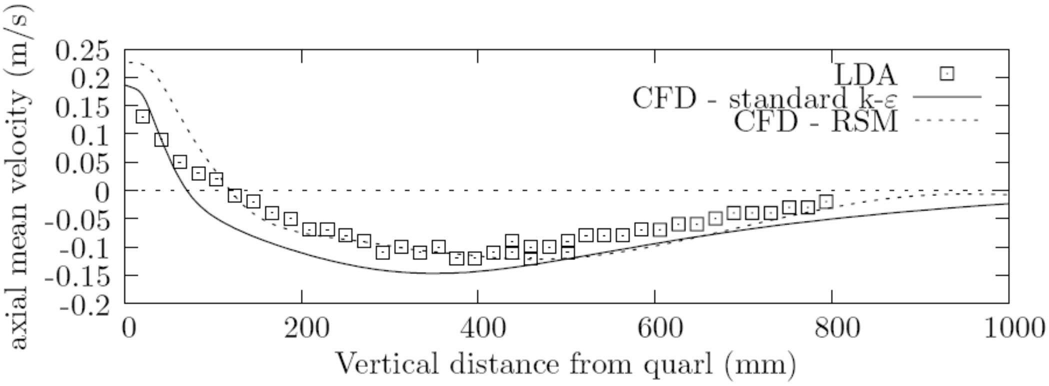

Figure 46 Comparison of predicted and measured centerline axial velocities indicating the extent of the primary recirculation zone

The ability to predict the axial extent of the primary recirculation zone is investigated in further detail by comparing the axial velocity along the centerline in Figure 46. From the comparison it is seen that the RSM turbulence model is in better agreement with the measurements in terms of the predicted recirculation zone. This is another flow feature which has an impact on the ability to predict the reacting flow behavior as it recirculates the hot combustion products to the primary reaction zone close to the burner. The difference between the two predictions is however only minor and from the current investigation no clear conclusion can be drawn pointing towards the RSM turbulence model giving better results than the frequently used k-ε model.

3.2 Subtask 3.2: Verification of reaction sub models

The objective of this task was to verify model performance by comparison to data obtained from tests at the Burner Flow Reactor (BFR) at BYU. The modeling of burners is one of the most critical issues in the modeling of biomass cofiring in suspension-fired plants. Consequently, the reaction patterns in the burner zone were studied by comparing CFD calculations of the BFR at BYU to measurements from the facility. Specific sub models that were validated include gas temperature profiles, gas composition profiles (O_2, CO_2, CO, SO_2, NO_x), and gas velocities. This section focuses on the comparison with data from the BFR under reacting flow conditions (Pickett, Jackson and Tree 1999). Three cases were studied based on measurements from two datasets:

Dataset 1 includes gas temperatures, gas composition profiles, and gas velocities as reported in (Pickett, Jackson and Tree 1999) during pure coal firing. As this dataset also includes gas velocities it was used to study the influence from various model parameters.

Dataset 2 includes gas composition during pure coal firing as well as coal and straw cofiring. This dataset was used to investigate the influence from cofiring. Coal firing was, however, also modeled as the coal type differs from dataset 1. The thesis by Chunyang Wu (Wu 2006) gives a detailed discussion of the dataset.

The volatiles composition and particle model parameters used for the simulations are given in the table below. Dataset 1 was based on the Wyodak coal and dataset 2 on the Blind Canyon coal (BC).

Table 9 Fuel volatiles compositions and particle parameters

	Wyodak	*BC*	*Straw*
Volatiles composition:			
- mass fractions daf			
ch4	44.2	7.5	2.0
h2	0.5	12.4	6.0
co2	20.0	23.2	18.6
co	35.3	57.0	73.4
Mean diameter µm	65.0	70.0	475.0
Spread coefficient, n	3.0	1.1	2.8
Density kg/m^3	1400.0	1300.0	350.0
Volatile component fraction %	48.8	50.0	90.0

The fuel ultimate and proximate analyses are given in the table below:

Table 10 Fuel proximate and ultimate analyses

	Wyodak	*Blind Canyon*	*Straw*
C	0.56	0.60	0.38
H	0.04	0.05	0.05
O	0.11	0.18	0.42
Moisture	0.24	0.03	0.06
Nitrogen	0.01	0.02	
Sulphur	0.00	0.01	
Ash	0.05	0.11	

In all cases, the gas phase boundary conditions were based on measured velocity profiles at the burner exit under isothermal conditions. The reactor wall temperature profile was also based on measurements. Calculation of the inlet gas mass flow from the measurements used as boundary conditions does not correspond to the flow rates reported with the measurements. This mainly due to variations in air flow rates between the different hot flow tests. The fact that the measurements were performed at some axial distance downstream from the burner mouth at cold flow conditions may also play a role. The profiles were scaled to match the flow rates etc. required. To analyze the importance of the inlet velocity profiles a simulation was made specifying plug flow velocity profiles upstream the burner mouth. The result from this analysis is reported in Section 3.2.3.4.

The first section below presents a grid sensitivity analysis. In the second section a reference calculation is presented in detail and predicted and measured gas phase properties are compared. In the third section a number of model parameter variations are presented and the influence from inlet velocity specification is investigated. The fourth section presents results from coal firing based on dataset 2, and section five discusses predictions of cofiring.

3.2.1 Grid sensitivity analysis

Initial tests were made investigating the influence from grid density. Predicted axial velocities based on grids with 14000, 24000 and 57000 cells showed that a grid with 24000 cells gives a grid independent solution. These simulations were based on the k-ε model and a first order upwind scheme. The comparison is shown in Figure 47. The results presented in subsequent sections are all based on the grid with 24000 cells.

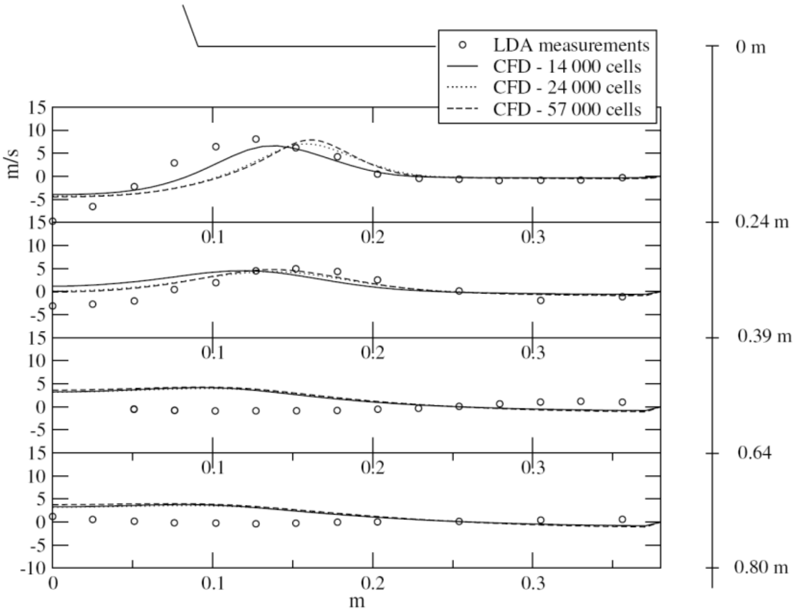

Figure 47 Predicted axial velocity profiles based on different grids

3.2.2 Dataset 1: Results for the reference case

The coal particles were treated as carrying 4 different volatile species, CH_4, CO, CO_2 and H_2. The mass fraction was found from the fuel analysis and the heating value. The coal moisture content was also accounted for, but the ash was omitted. The particle calculation is faster when the ash is not included as the particle tracing is terminated when all the mass has been transferred to the gas phase. The flow was considered 2 dimensional rotational symmetric. The eddy-dissipation model (EDM) was used for the combustion reaction rate predictions and radiative heat transfer was modeled using the discrete ordinates radiation model. Lagrangian particle tracking of the coal, with a Rosin-Rammler size distribution was used, with 6 size groups and a median of 65 μm. The discrete random walk model was used for the turbulent particle dispersion.

Figure 48 shows a close-up of the velocity distribution in the quarl and air inlet area. The coal particles are carried with the primary air, located around the symmetry axis to the left in the figure. The secondary air is rotating and the swirl of the flow forces the secondary air towards the quarl wall. Note that in reality the burner is down fired, but here the flow is shown as being horizontal. The secondary air stream continues downstream from the rear wall with a high velocity. A region with high velocity is also seen downstream the primary air inlet, close to the symmetry axis, which is due to a reversed flow zone.

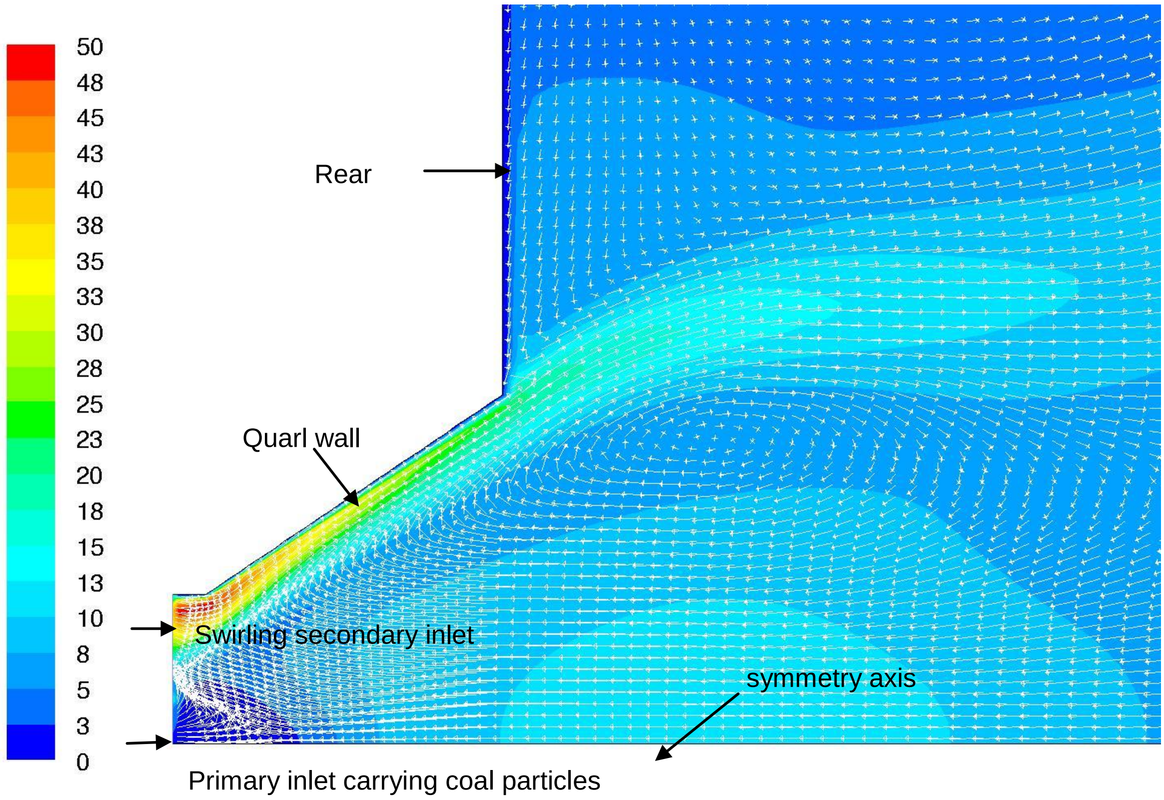

Figure 48 Close-up of the near burner velocity distribution

A contour plot of the velocity magnitude in the whole burner is shown in the top of Figure 49. The distribution is typical for coal fired swirl burners, with the high velocity ejecting from the outer quarl wall and a region with higher velocities in the reversed flow zone close to the quarl area. A region with lower temperatures is seen at the primary and secondary air inlets. The region with lower temperatures continues downstream with the secondary airflow. The temperature increases towards the outer wall and downstream and a region is seen from the quarl area towards the outer wall, which is related to the path of the coal dust particles, which is shown in the third plot from the top. Only a fraction of the particle trajectories are included. A part of the particles continues with the primary air and penetrates the axial reversed flow zone, shown as a contour line of zero axial velocity. The main part of the coal dust particles are captured by the rotating secondary air stream and are transported into the furnace close to the quarl wall and continue towards the outer wall. A high concentration of particles is seen in the corner area of the rear wall and the outer wall. The high concentration of particles in the corner results in a region with low oxygen content, due to the combustion of the coal. The overall picture of the combustion process is a rapid intense combustion with the temperature and oxygen levels reaching a constant level close to the quarl.

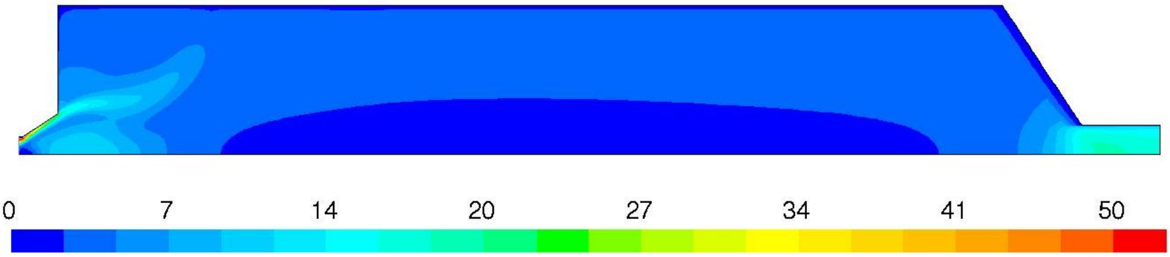

Velocity magnitude

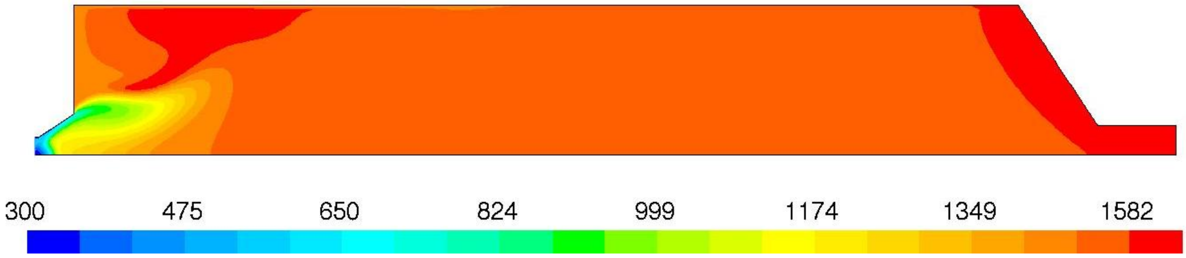

Temperature distribution (Kelvin)

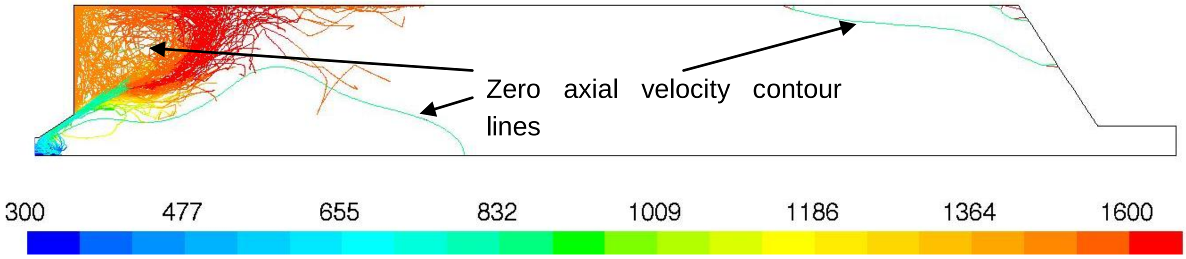

Particle trajectories, colored with particle temperature, and reversed axial velocity zones

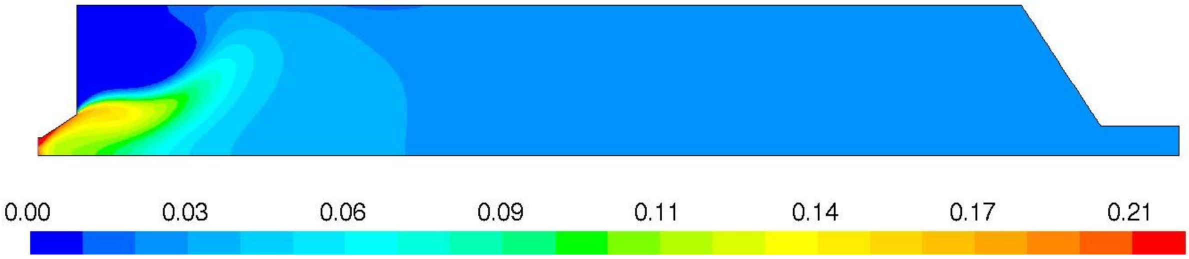

Volume fraction of O_2 (dry)

Figure 49　　Illustration of overall combustion pattern

3.2.2.1　Comparison with measurements

The axial velocity, swirl velocity, oxygen concentration and temperature predicted from the CFD calculation are compared to measurements in Figure 50 and Figure 51.

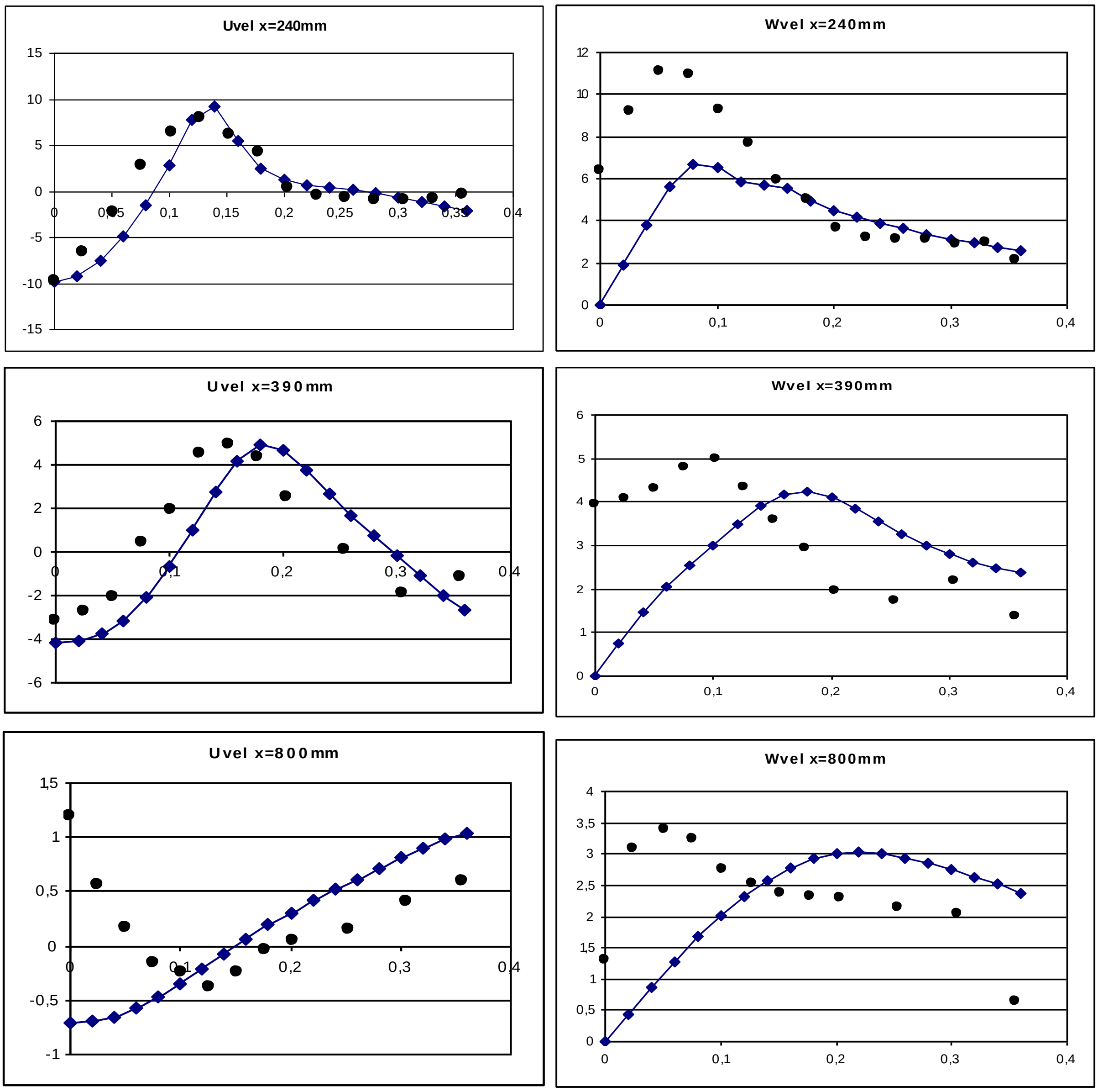

Figure 50 Comparison of predicted and measured axial and tangential velocities. The solid line represents predicted values and the dots are measurements

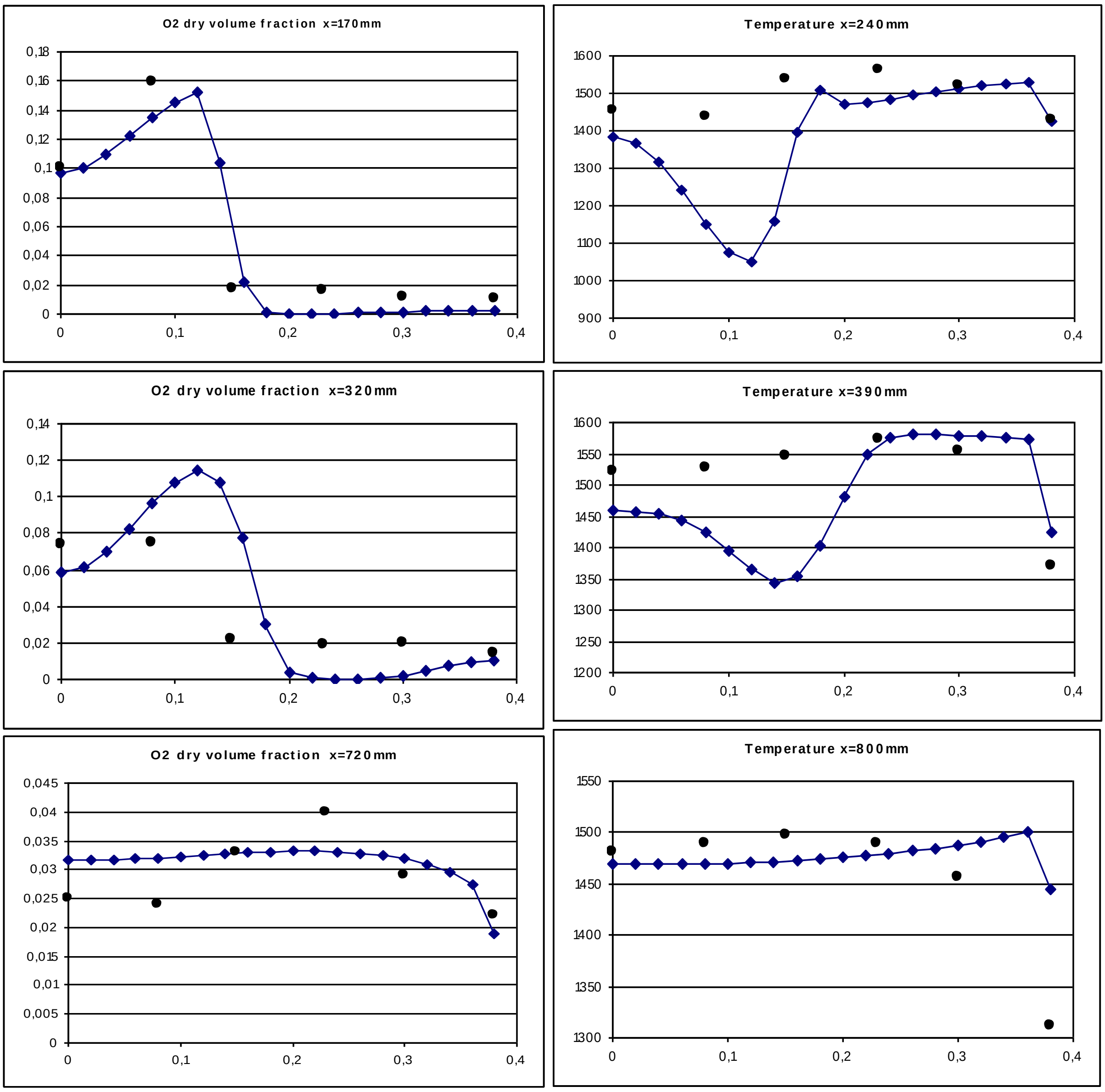

Figure 51 Comparison of predicted and measured oxygen and temperature profiles. The solid line represents predicted values and the dots are measurements

3.2.2.2 Velocity profiles

There is very good agreement between the CFD calculations and the measured axial velocity distribution at the first two downstream locations, 240mm and 390mm. At 800 mm the agreement is not as good, in particular close to the central axis where the recirculation zone still exists in the prediction.

In general, the measurements show a non-zero tangential velocity at the location of the central axis. This indicates the flame was not symmetrical around the geometrical centerline during the measurements or that the experimental technique suffered inaccuracies inside the flame. In the CFD calculation, the centerline swirl velocity is zero due to the imposed boundary condition.

The specified inlet velocity profiles strongly influence on the predicted flow pattern and the development and behavior of the primary recirculation zone. The tangential inlet velocity profile was forced to zero at the centerline although the measurements showed a non-zero value. Similarly, the axial velocity profile was scaled to make the integrated mass flow rate fit the reported total flow rates in the measurements. A simulation is presented later that illustrates the importance of inlet velocity profiles on the overall flow pattern.

3.2.2.3 Temperature

There is some disagreement between the CFD calculations and the measurement at the first two downstream locations. The CFD calculations show a relatively large temperature drop in a region around radius 0.05m to 0.2m. The relatively cool secondary air continues downstream from the quarl exit causing a relatively low temperature in the region mentioned above. The same temperature drop is not found in the measurement. Most likely this is due to an influence from the surrounding hot gases on the local temperature measurement either because of radiation or due to gases being sucked into the suction pyrometer from the hotter surrounding region. At a downstream location of 800mm there is reasonably good agreement between the CFD calculation and the measurement, except towards the outer wall. This difference is a bit surprising as measured temperatures are used as wall boundary conditions in the CFD calculation.

3.2.2.4 O_2 volume/mole fraction

At 170mm good agreement was found between the CFD calculations and the measurement. The CFD calculation predicts near-zero O_2 concentration towards the wall whereas the measured values are around 2%. This could indicate the model predicts a too fast reaction rate in the mixing zone. At the measuring location 320mm, there is a difference in the trend of the profiles. The predicted oxygen concentration has a maximum in the region between radii 0.1m and 0.2m whereas the measurements show a monotonic decrease. The reason for the O_2 concentration peak in the CFD calculation is related to the secondary air stream. The primary reaction occurs is in the mixing zone between the secondary air stream and the bulk flow.

3.2.2.5 Summary on the reference case

Reasonably good agreement was obtained between the CFD calculation and the measurement. It has though not been possible to obtain a good agreement with both the concentration of oxygen and the temperature with the same settings in the CFD calculation. This is mainly ascribed to uncertainties in the temperature measurements.

3.2.3 Dataset 1: Model parameter variations

A large number of model parameters and choices influence the results of the CFD predictions. An investigation was made to analyze some of the most significant for this specific test case. The following table summarizes the models investigated. The different options that were included and the choice of other main model options are also given. The importance of selected boundary conditions is evaluated later.

Table 11 Outline of the different model combinations investigated

Investigated model	*Model choice*	*Fixed models*
Differencing scheme	Upwind 2nd order upwind Quick	k-ε turbulence model mixture fraction combustion model
Turbulence model	k-ε model k-ε model RSM model	2nd order upwind differencing scheme mixture fraction combustion model
Combustion model	1 mixture fraction 2 mixture fractions EDM Jones & Lindstedt EDC Jones & Lindstedt	2nd order upwind differencing scheme k-ε turbulence model

3.2.3.1 *The influence from differencing scheme*

The choice of interpolation or differencing scheme is often pointed out as a key issue in CFD analyses. In general higher order schemes are more accurate (better representation of the variation between grid points) but numerically less stable. Simulations were made using three different schemes for this specific case; a first order upwind, a second order upwind and a third order QUICK scheme. Predicted axial velocity profiles are compared to measurements in Figure 52.

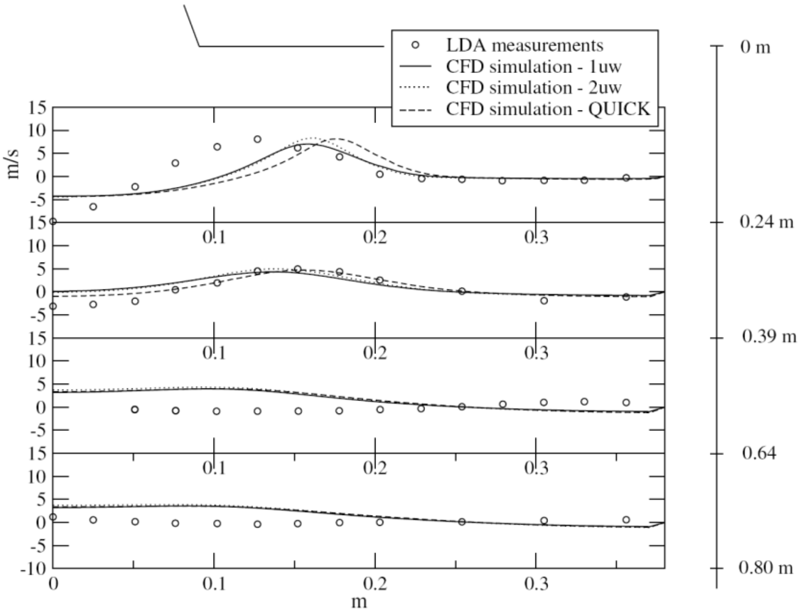

Figure 52 Influence from differencing scheme on the axial velocity profiles

The first and second order accurate upwind schemes are seen to give comparable results whereas the QUICK scheme gives slightly different results at the first axial location. The fact that there is little difference between the three schemes included is most likely due to the fact that the grid resolution is relatively high reducing the advantage of higher order schemes over the first order upwind scheme. In other words it results from choosing grid resolution based on a first order scheme in the grid sensitivity analysis. It was decided to use the second order upwind scheme in subsequent simulations.

3.2.3.2 The influence from turbulence model

The turbulence closure model is another issue, which is often discussed in CFD analyses, in particular, when dealing with swirling flows. An investigation was therefore made to determine the impact of turbulence closure for the specific setup modeled. The standard k-ε model was applied as a reference and compared to the TT k-ε model (k-ε with modified constants) and the Reynolds Stress Model (RSM). Figure 53 compares predicted and measured axial velocity profiles.

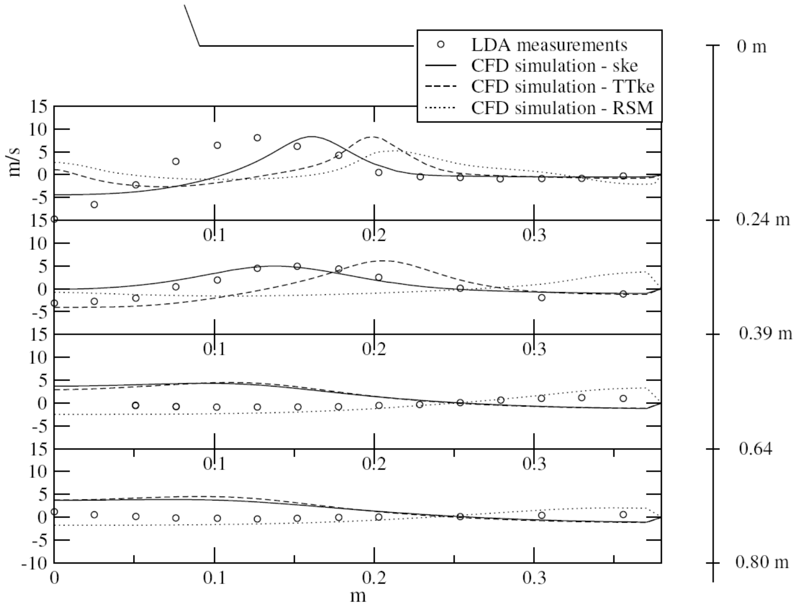

Figure 53 Predicted axial velocity profiles based on different turbulence models

The best agreement with measurements was obtained with the standard k-ε model which will be used in the remaining simulations. This finding is not considered to apply to swirl burners in general but it has been a consistent trend in all simulations of the Burner Flow Reactor made at Aalborg University under both reacting and non-reacting conditions.

3.2.3.3 The influence from gas combustion model

The modeling approach used to calculate gas phase reaction rates is a central part of any turbulent combustion simulation. Two approaches were tested, the first based on the mixture fraction approach using 1 and 2 mixture fractions to represent the fuel streams. In the second category, the eddy-dissipation model (EDM) and the eddy-dissipation concept (EDC) were applied with a four-step reaction mechanism suggested by Jones and Lindstedt. Figure 54 compares predicted axial velocity profiles from the two mixture fraction based models with measurements.

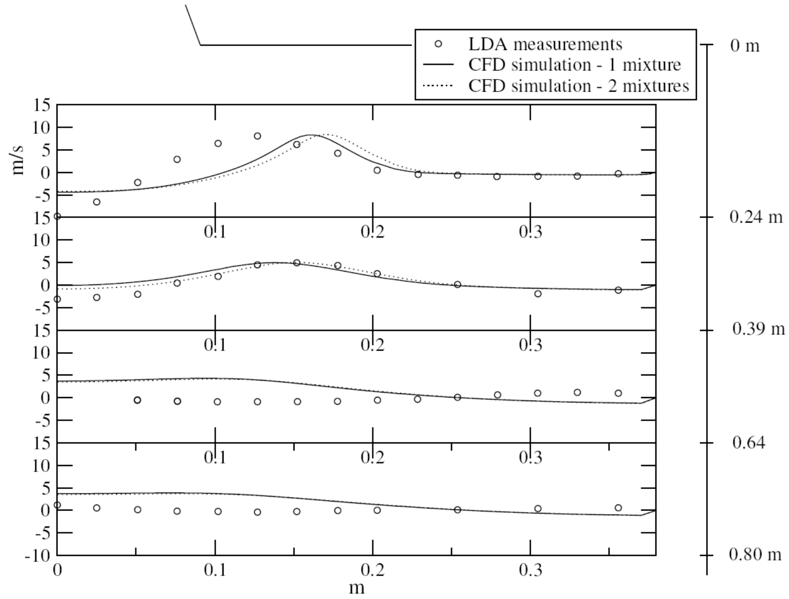

Figure 54 Predicted axial velocity profiles based on one and two mixture fractions combustion models

The 1 mixture fraction approach does not distinguish between volatiles and char whereas with the 2 mixture fractions model they are treated as separate fuel streams. As seen from Figure 54 there is very little difference between the two with respect to predicted axial velocity profiles. The simulation of cofiring would require a third mixture fraction to distinguish between the two volatiles streams (coal and straw) and the char. This is not currently possible with FLUENT and in addition the advantage of the mixture fraction approach compared to the EDM and EDC models in terms of simplicity is not so evident as additional mixture fractions are introduced.

Figure 55 compares predicted axial velocity profiles based on the EDM and EDC models to experimental data. Two simulations were made with the EDM model, one based on the second order upwind scheme and one with a power law scheme.

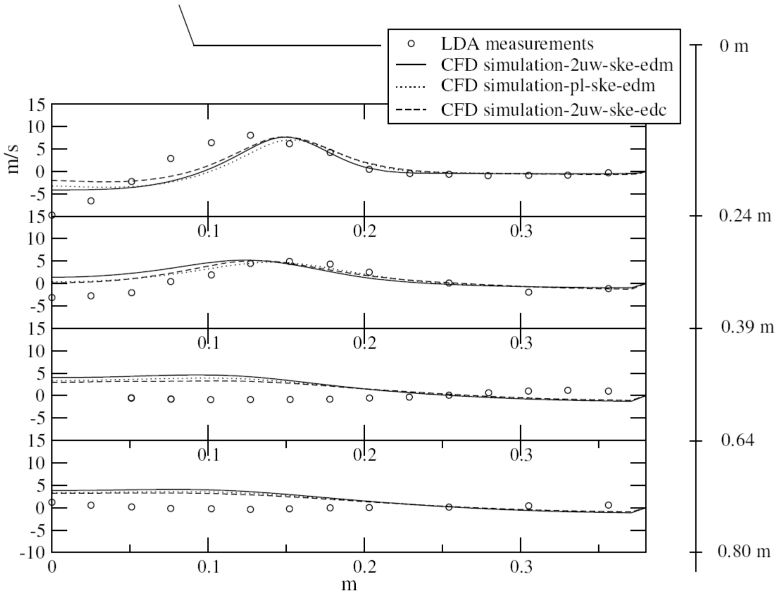

Figure 55 Axial velocity profiles predicted using the FLUENT EDM and EDC models in combination with the four-step Jones & Lindstedt reaction mechanism

There is little difference in the results obtained with the EDM and EDC models. In both cases the agreement with measurements is better than that obtained with the mixture fraction models presented in Figure 54. The EDM model will be used in the remaining simulations.

3.2.3.4 Sensitivity to inlet boundary condition specifications

A series of calculations were also carried out where sensitivity to the inlet boundary conditions for the combustion air and coal particles was addressed. The inlet velocities were measured under non-reacting conditions at a location downstream the burner exit. Corrections of the profiles were made to fulfill requirements like overall air mass flow, split between primary and secondary air, zero swirl at the centerline etc. For comparison a simulation was therefore made with the location of the inlet for the primary and secondary air moved 400mm upstream and plug-flow axial and tangential velocity profiles. For the tangential velocity a swirl angle of 45 degrees was assumed (i.e. equal magnitude of axial and tangential velocity components). Figure 56 illustrates the two computational domains used.

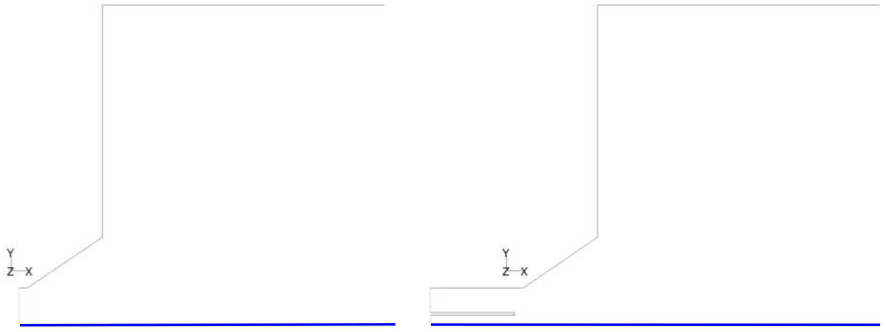

Figure 56 Computational domains used to study influence from inlet boundary location

The influence of a range of different parameters in the CFD discrete phase (particle) specification were investigated; size distribution, number of different particle sizes, turbulent dispersion model, devolatilization rates. Figure 57 compares the following 4 simulations with experimental data:

Reference case: Setup as described in section 3.2.2 with the particle size distribution represented by 6 discrete size classes and a mean particle diameter of 65 micron.

Case 1: The number of size classes was reduced to 3.

Case 2: The particle mean diameter was changed to 81 micron and the Rosin-Rammler exponent from 3 to 3.19 giving a better fit to the measured size distribution

Case 3: The inlet conditions were specified as illustrated in Figure 56 to the right with plug flow velocity profiles.

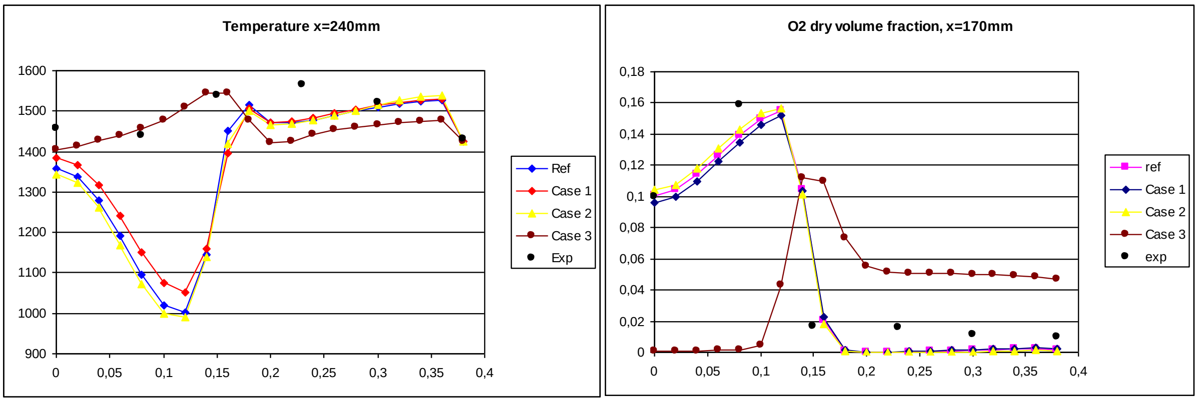

Figure 57 Comparison of the reference simulation to cases 1 to 3 and measured data

The changes made in the particle model all had a minor impact on the results (as an example compare reference case to cases 1 and 2). The reason for the limited impact may be the high volatile content in the coal. The volatiles are released fast and maintain the flame pattern unchanged. The results were sensitive to the gas phase boundary condition specification. As seen from case 3, the flow, temperature and oxygen concentration profiles changed completely when the upstream plug flow velocity profile was used. The agreement with the measured temperature profile improved but it resulted in poor correspondence with the velocities and the oxygen (and other species) concentration profiles. As discussed in Section 3.2.2.1, the temperature measurements are believed to be associated with considerable uncertainty at radial locations of 0.05m to 0.2m. Therefore, the results obtained in the reference case are considered more correct than those of case 3.

3.2.4 Dataset 2: Coal firing results

This section focuses on the comparison to the experimental data collected by Chunyang Wu that are described in detail in (Kær, Rosendahl and Baxter, 2006). Although good agreement between measurements and predictions has been demonstrated for coal firing in the BFR, additional simulation of coal firing are presented in this section as a different coal type, Blind Canyon, was used in the subsequent cofiring tests. Figure 58 compares O_2 and CO_2 profiles at four axial locations based on the same model setup as the reference case in section 3.2.2 except for the changes required to account for differences in fuel proximate and ultimate analyses, cf. Table 10.

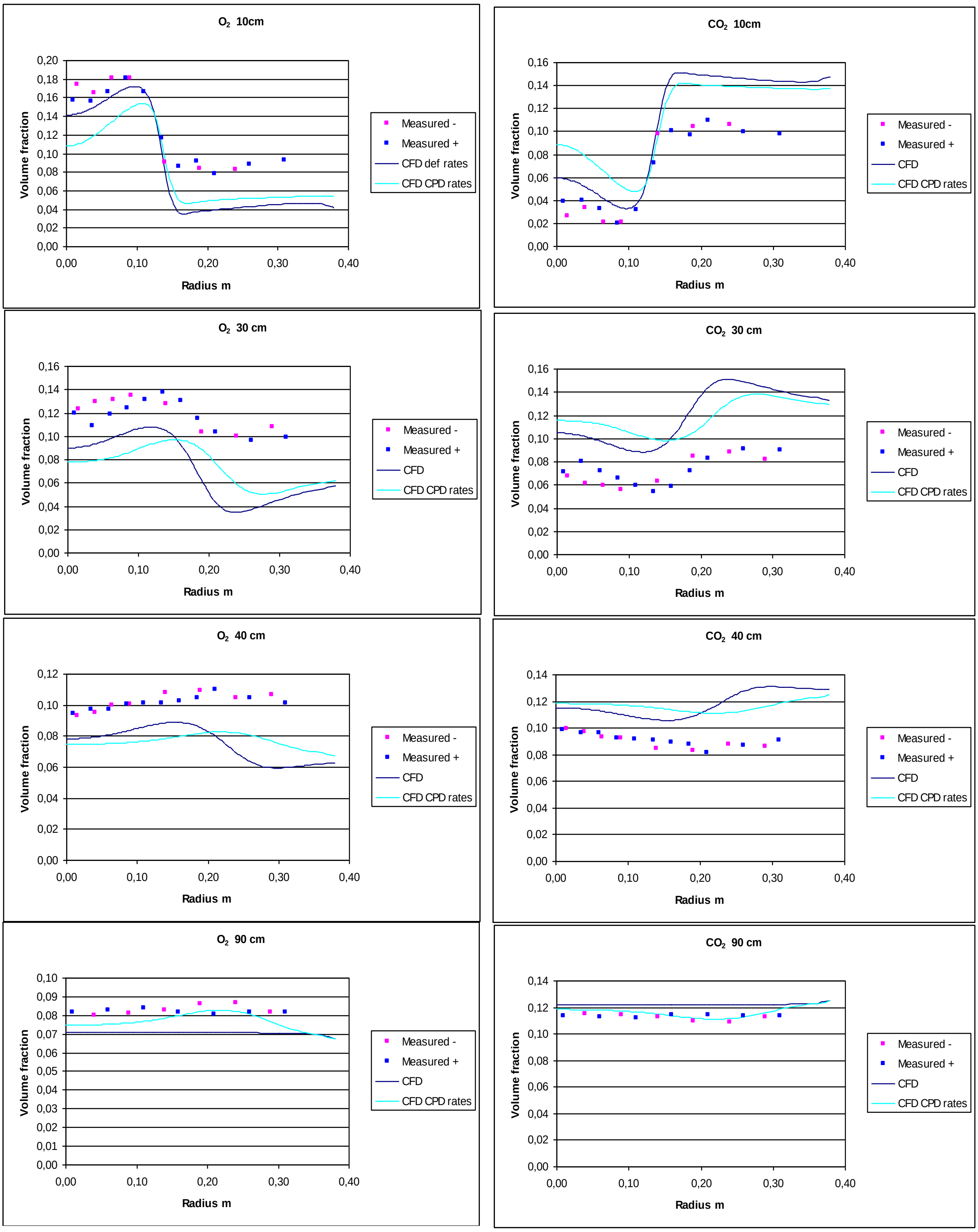

Figure 58 Comparison of predicted and measured O_2 and CO_2 volume fractions

The trends in O_2 as well as CO_2 profiles are well-captured at all axial locations. There is a tendency for the predicted O_2 values to be slightly lower than the measured. This is most likely related to a minor difference in overall stoichiometry between the experiment and the prediction as seen from the predicted O_2 concentration being approximately 0.01 below the measurements at the axial location of 0.9 m. This is consistent with the CO_2 level being slightly over predicted. In general the trends in O_2 and CO_2 are consistent.

Predictions were also made where the single rate devolatilization model of the reference case was changed to the more physical CPD model available in FLUENT. The results from these simulations are included in the comparison shown in Figure 58. The overall trends are comparable to those obtained for the reference case. If the predicted profiles were shifted upwards to fit the O_2 level of the measurements the CPD model seems to capture the profile shape slightly better than the single rate model.

The prediction of CO concentration profiles with relatively simple gas phase reaction mechanisms, as the one applied in these simulations, is associated with significant uncertainty. Still, the degree of correspondence between measured and predicted profiles is surprisingly good, as illustrated by Figure 59 showing CO volume fractions at four axial locations.

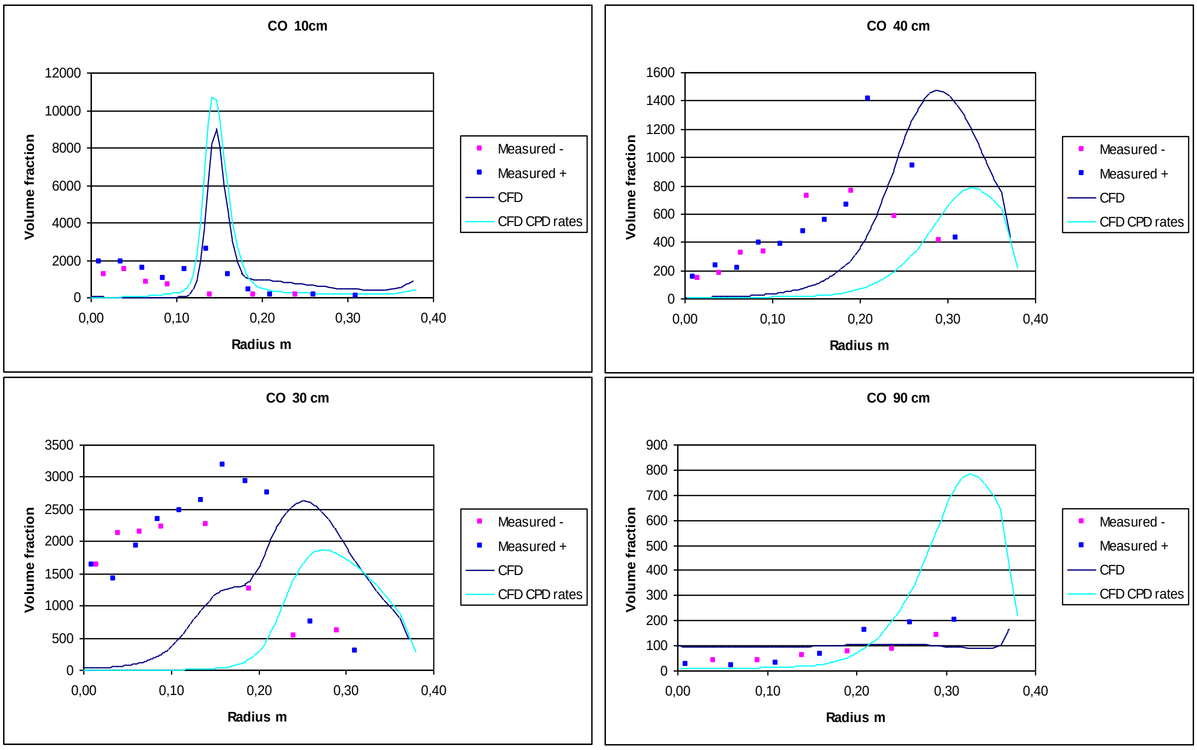

Figure 59 Comparison of predicted and measured CO volume fractions

The predicted and measured CO concentrations peak in the region where the O_2 concentration has a strong gradient (the primary reaction zone). This is most evident at the axial location of 10 cm and the predicted level exceeds the measured significantly. Taking into account that the predicted O_2 concentration at the same location is slightly too low may indicate a too fast reaction rate in the predictions. Another possible explanation could be that it is difficult to capture such a narrow CO peak experimentally. The peak is almost entirely located between two measurement locations.

3.2.4.1 Observations on flame stability

During the calculations it was observed that, with only small differences in the initial guess, different solutions could be obtained. Figure 60 and Figure 61 show the recirculation zones and particle trajectories from a calculation with same physical settings, but different initial guesses.

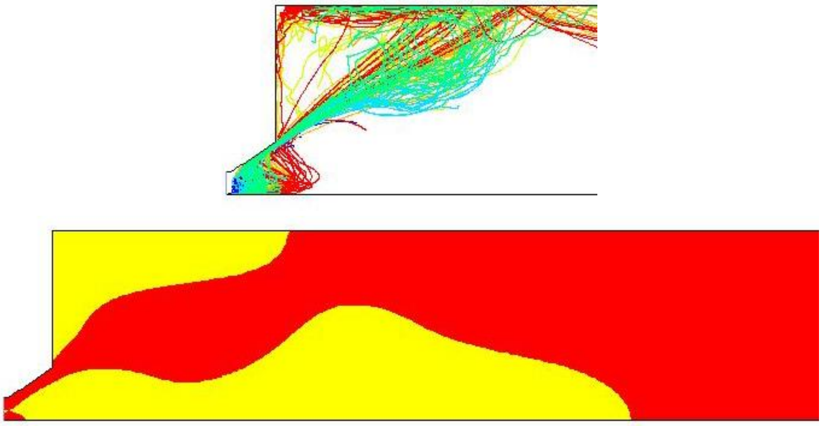

Figure 60 Particle trajectories (color represents particle ID) and recirculation zones for calculation 1

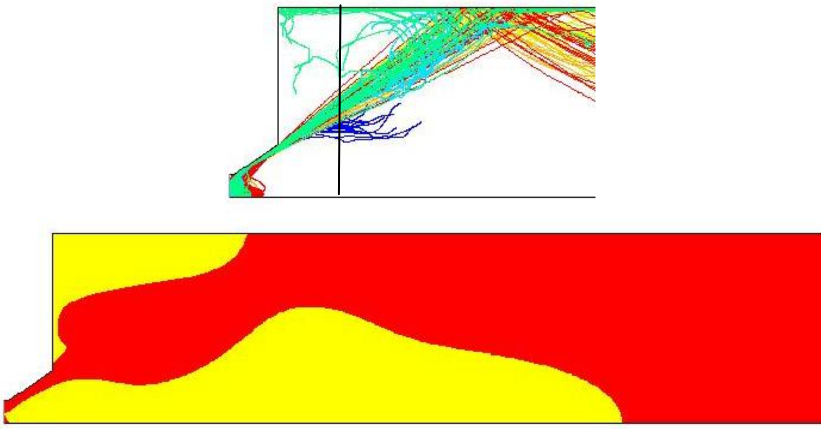

Figure 61 Particle trajectories (color represents particle ID) and recirculation zones for calculation 2

The extent of the primary recirculation zone is about the same in the simulations, but a small difference is seen in how close the zone is to the inlet. A different shape of the external recirculation zone is also seen. In particular the former has a dramatic impact on the gas concentration profiles etc. as is seen from Figure 62. The profiles are collected at the axial location indicated by the vertical line in Figure 61.

The particle trajectories are different for the two calculations. In calculation 1 more of the particles penetrate the primary recirculation zone and more of the particles are reversed into the secondary recirculation zone. The fact that more particles penetrate the primary recirculation zone results in lower O_2 concentrations along the centerline.

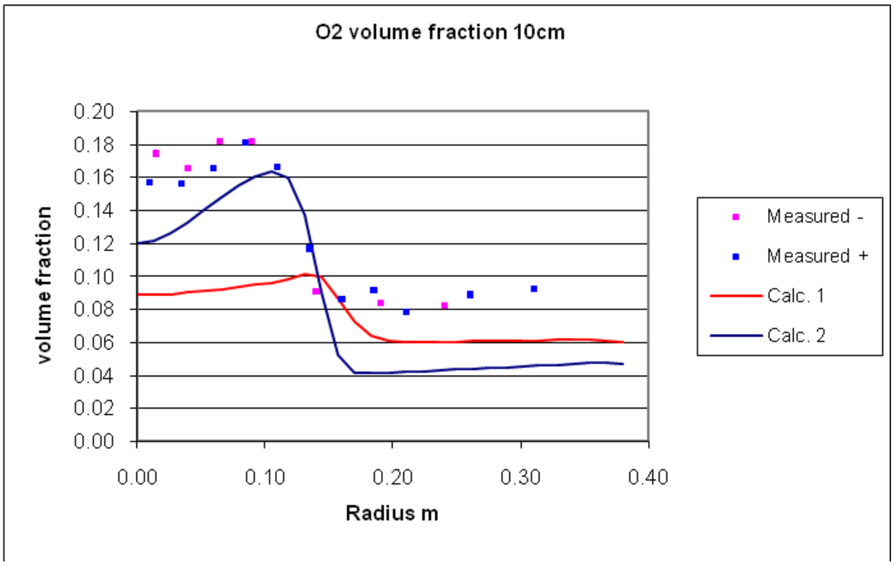

Figure 62 Oxygen concentration 10cm downstream the quarl outlet for the two calculations shown in Figure 60 and Figure 61.

In summary, there is no doubt that the results for the two calculations should be identical, but there was a tendency in the CFD calculation that the solution locked into one of the two flow patterns shown in Figure 60 and Figure 61. There was no difference in the convergence behavior for the two calculations; both converged to a low stable residual level. Predictions made with the double precision version of FLUENT led to similar findings showing that it is not the result of round-off errors in the simulations.

An explanation for the observed behavior could be that the physical settings results in unstable conditions, but the selection of a two dimensional axi-symmetric steady state model forces the solution to be stable and results in different solutions depending on the initial guess of the flow field. A thorough investigation of these issues would require a 3-dimensional, transient CFD calculation possibly with the Large-Eddy turbulence model. It was not possible to undertake such a comprehensive task within the timeframe of this project.

3.2.5 Dataset 2: Coal and straw cofiring results

Coal and straw cofiring (50/50 distribution on energy basis) predictions were made with the coal representation and all other settings as for the reference case above. The gas phase boundary conditions as well as the straw analyses and size distribution were based on the data given in the thesis by Chunyang Wu (Wu 2006) and the parameters presented in Table 9 and Table 10.

As for the coal firing case presented above the simulations were very sensitive to the inlet boundary condition for the gas phase as well as the particles whereas other parameters only had minor or no influence on the results when varied within reasonable limits. Physically, the same phenomenon of axial relocation of the recirculation zone’s forward stagnation point is observed. When compared to the coal firing case the cofiring case is characterized by a significantly increased fuel mass flow rate (from 12.3 to 20 kg/hr) and only a minor change in gas mass flow rate. This results in an even more pronounced deformation/penetration of the primary recirculation zone. This is illustrated graphically in Figure 63 in terms of reversed flow regions (yellow) and forward flow regions (red) as well as particle trajectories.

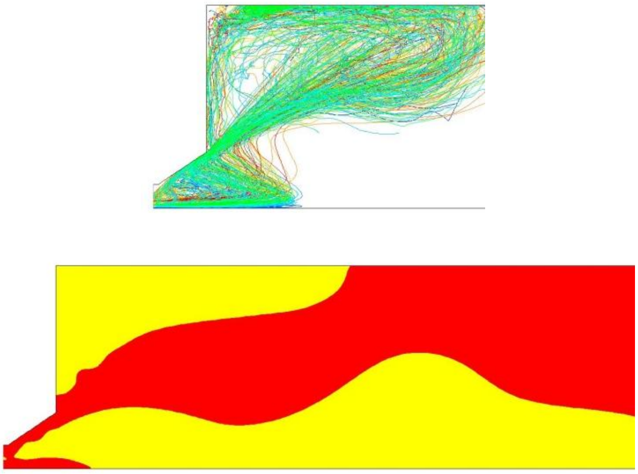

Figure 63 Recirculation zones with zero radial particle (coal and straw) initial velocity

To illustrate the sensitivity to inlet boundary conditions, the particle were assigned a radial velocity component at the inlet corresponding to that of the gas phase (corresponding to zero particle slip velocity). The result from this simulation is shown in Figure 64 with contours and trajectories similar to Figure 63.

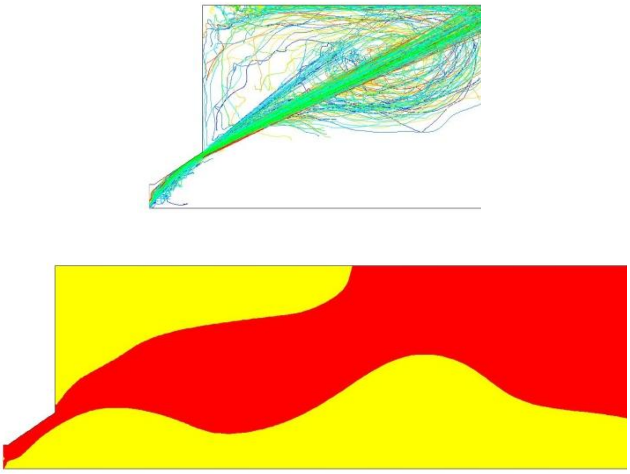

Figure 64 Recirculation zones with radial particle (coal and straw) initial velocity

The resulting change in reversed flow zone is pronounced as the deformation does no longer exist. Whether one or the other is more correct is very difficult to determine but the importance of accurate boundary condition specification is evident. Further model parameter studies were not made as the impact of these would all be minor compared to the changes in flow pattern occurring as the boundary conditions are changed within the uncertainty band with which they were measured.

Figure 65 compares predicted and measured O_2 and CO_2 concentration profiles. The predictions correspond to the flow field illustrated in Figure 63 above. The agreement is reasonably good at the axial positions 200mm, 300mm and 400mm downstream the inlet. At the location 1100mm downstream the predicted O_2 level is significantly higher than the measured. The prediction agrees with overall stoichiometry calculations based on the reported fuel and air flow rates and the fuel compositions. The disagreement is therefore ascribed to a drift in the operating conditions of the reactor compared to the reported conditions.

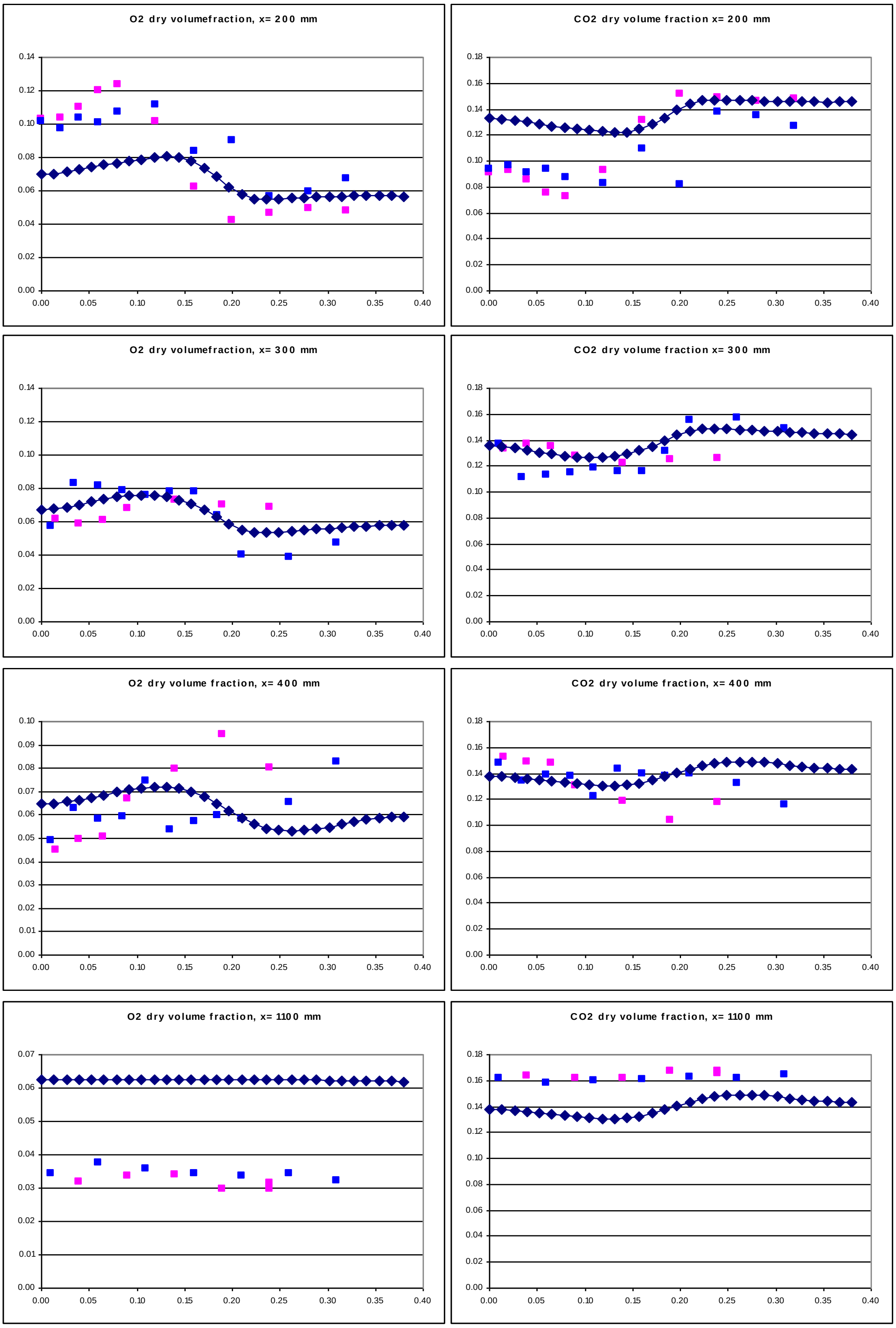

Figure 65 Comparison of predicted and measured O_2 and CO_2 profiles during coal and straw cofiring

Although the agreement is acceptable it is important to note that several parameters, in particular the inlet conditions, have to be established with higher certainty before the influence from model setup can be evaluated with confidence.

3.2.6 Summary on reacting flow verification

A detailed comparison of model predictions to comprehensive experimental datasets was presented in this section. The influence from selected key parameters on the results was investigated and the following overall conclusions were drawn:

Of all the parameters investigated, the inlet gas and particle properties including velocity profiles have by far the most significant impact on the results.

The location of the recirculation zone forward stagnation point and the deformation of recirculation zone vary significantly with the parameters mentioned above.

There is good agreement between measured and predicted species concentration and gas velocity profiles particularly for the two coal firing cases investigated when the location of the recirculation zone is accurately captured.

The coal and straw cofiring case introduces additional complexity to the simulation due to the different behavior and physical characteristics of the straw compared to coal. Further studies are needed to draw conclusion with reasonable confidence since the predictions are very sensitive to the inlet conditions.

Looking forward the dataset recently collected is expected to shed further light on these issues as detailed studies were made to accurately establish the inlet conditions.

4. Task 4: Model demonstration

The objective of this task is to demonstrate the capabilities of the models in the analysis of industrial problems and to provide guidelines for cofiring biomass in suspension-fired power plants.

4.1 Subtask 4.1: Low-NOx burner modeling and optimization

The objective of this task is to make use of the developed models as well as information obtained during the experimental studies in Subtasks 1.2 and 1.3 to design optimized burners for cofiring biomass in a suspension-fired unit. Specifically, burner operation and design will be modeled to help determine the best placement of biomass within a burner. The potential synergy effect between different fuels (fuel mix) in terms of reduced deposition and corrosion tendency will be investigated.
Deliverables from this task include design guidelines for cofiring biomass in low-NO_x burners supported by extensive experimental and numerical studies.

Concise versions of the guidelines appear in this document under a new task number (Task 5), where they are not overshadowed by the considerable discussion of detail on which they are based.

This section discusses NO_x formation during biomass-coal combustion in a swirl-stabilized burner. The following aspects are considered: First, maps of important NO_x intermediates, HCN and NH_3, are analyzed. Second, NO data are compared among the biomass and coal tests, and the emission is analyzed on different bases. Third, the relation between the intermediates and NO formation is discussed through the comparison of the conversion of fuel-N to NO among the tests, supplemented with kinetic calculations.

During the course of the project it was realized that experimental investigation of different strategies for introducing the secondary fuel in the burner and determining the effects hereof on burner performance, deposition and corrosion tendency proved to be too arduous an undertaking. The study of these effects has consequently been postponed, and is investigated experimentally in a continuation of this work (Damstedt, et al. 2005). Investigation through model simulation will similarly await the completion of the models capable of predicting the conversion of biomass particles which have not been available until the closure of the project. Investigations will thus be included in the work being undertaken in the PSO 4881 project.

4.1.1 Measurements of HCN and NH_3

Fuel-N in coal exists in the form of unsaturated cyclic nitrogen compounds, mostly clusters of pyrolic and pyridinic forms. Biomass nitrogen resides dominantly in acyclic molecules such as derivatives of amine, amide, and amino acids. Based on the bond analysis between the possible nitrogenous products and the compounds in the parent fuels, HCN should be the dominant NO_x precursors in coal flames, while NH_3 should dominate during biomass combustion.

Indirect evidence of the minimal impact of sample conditioning, specifically water condensation, on the HCN/NH_3 concentrations appears in Figure 66, which illustrates the real-time measurement of NH_3 and HCN with their respective CO profiles from a pure straw test and pure coal (Blind Canyon) test. NH_3 probe measurements are calibrated with NIST-traceable calibration gas samples, while the HCN calibration relies on a theoretical spectra data base provided with the analyzer. HCN calibration gases are in principle available for calibration, but they pose unacceptably high safety risks and are not used in these tests. The figures indicate very high correlation between the CO and both the HCN and NH_3 signals. The oscillations in the NH_3, HCN, and CO profiles arises from alternating the probe position between the fuel-rich region and the reacted-gas region of the Blind Canyon and straw flames, with the intent to test the gas measurements at extreme conditions as major gas species concentrations change significantly. Though only very limited amounts (less than 15 ppm) of HCN and NH_3 are detected in the flue gas, the peak amounts appear at the same time as the peak CO content. While the quantitative accuracy of the HCN measurements lacks direct validation by NIST-traceable calibration gases, it quantitatively correlates with other fuel-rich species (CO and NH_3), indicating that its measurement is at least semi quantitative (trends are quantitatively correct even if absolute magnitude may be in error). CO and NH_3 exhibit both of these characteristics and are quantitatively calibrated against standard gases.

Both HCN and NH_3 generally occur only in reducing environments, as indicated by the presence of CO. Water is present in quantities (typically 13-20%, mole percent) that greatly exceed CO, NH_3 or HCN in both (mildly) reducing and oxidizing conditions. Since the measured NH_3 and HCN closely follow fluctuations in CO and during their measurements and no water condensation was detected through the optical access in the cyclone (the lowest-temperature and elevation point in the sample train), the impact of water condensation on the gas sample should be limited.

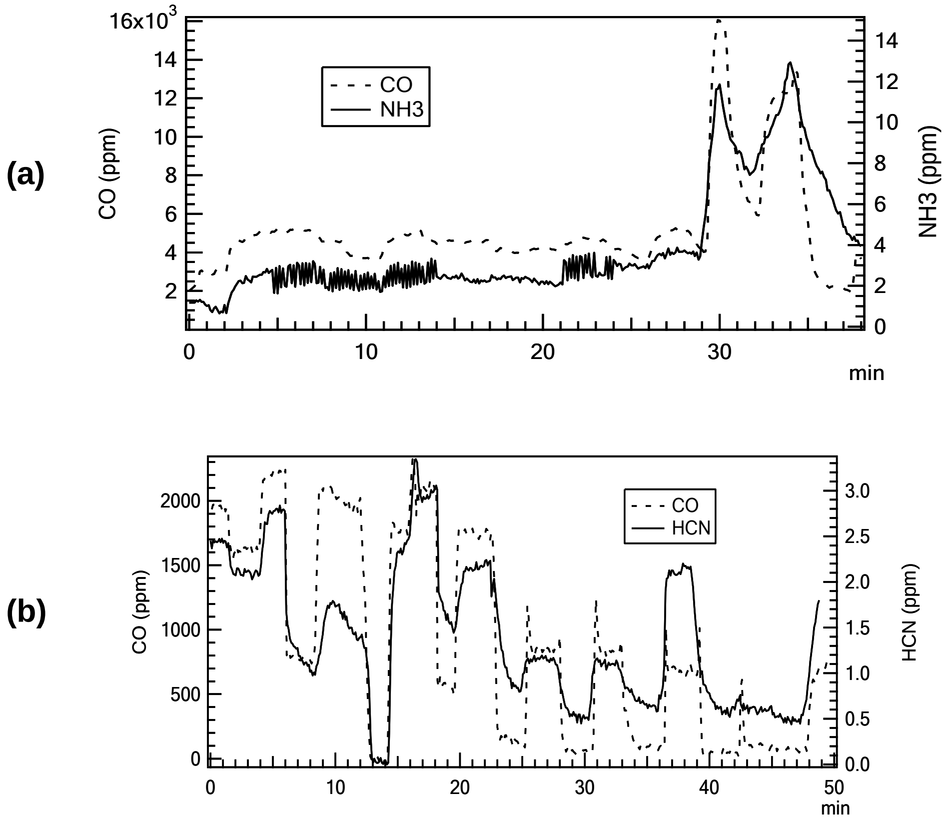

Figure 66 Temporal variations in NH3 and HCN concentrations compared to CO concentration in the swirling section of the BFR. (a) NH3 with CO under Test S (b) HCN with CO during Test BC.

Consistent with the high CO mole fraction existing near the reactor inlet, HCN and NH_3, when detected, were found mainly in the top section, 0-50 cm below the quarl. Though all the tests involved overall fuel-lean conditions, the existence of HCN/NH_3 provides strong evidence that there is a locally and probably transient fuel-rich region in the top section of the reactor, corresponding to the reverse flow region. This section discusses spatial maps of HCN and NH_3 for different cofiring and pure biomass/coal tests and their implications on the flame behavior, supplemented with spatial profiles of CO and local stoichiometry.

Examples of HCN and NH_3 maps from the Test BC appear in Figure 67. The HCN peak values appear in similar regions as those of CO (Figure 6). The HCN data comfortably exceed the noise levels of the analyzer. NH_3 data are below the minimal detection limit throughout the reactor, indicating NH_3 concentrations under this condition are too low to be measured with this system (< 1 ppm) and the patterns seen in the figure are not significant.

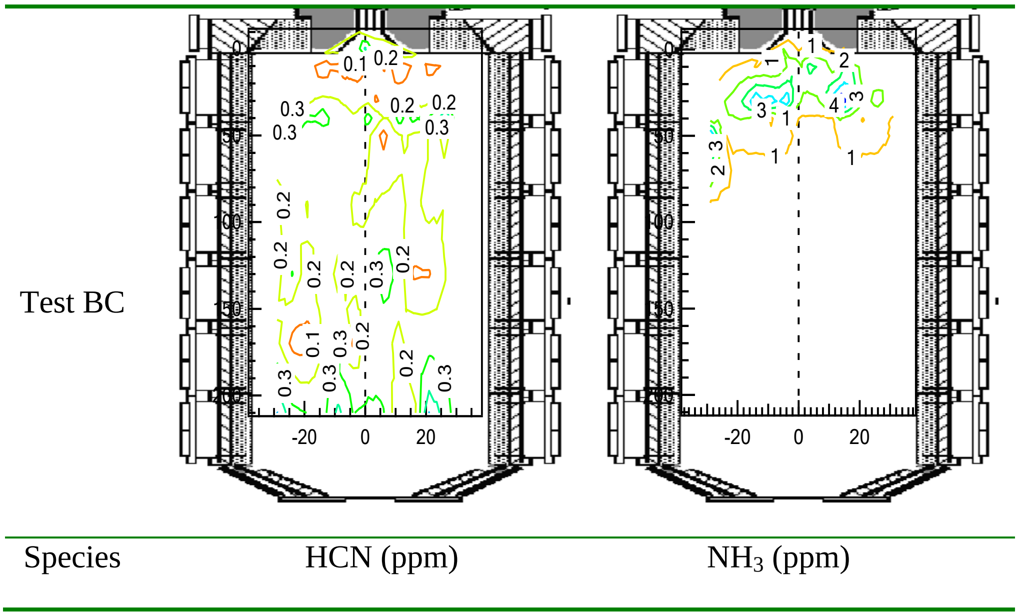

Figure 67 Two dimensional maps of HCN and NH3 from Test BC. NH3 data are below detection limits and the indicated patterns are not significant.

Figure 68 depict the HCN and NH_3 maps from the three tests involving straw and Blind Canyon coal. In the coal test, HCN dominates NH_3 as the primary fixed-nitrogen species in the gas phase. The same is true in Test 50S50BC, and the test of 70S30BC. In Test S, NH_3 rises above the measurement limit and has higher concentration than HCN in the fuel-rich region. These data clearly show that straw and Blind Canyon release nitrogen in different forms and generate different NO_x intermediates

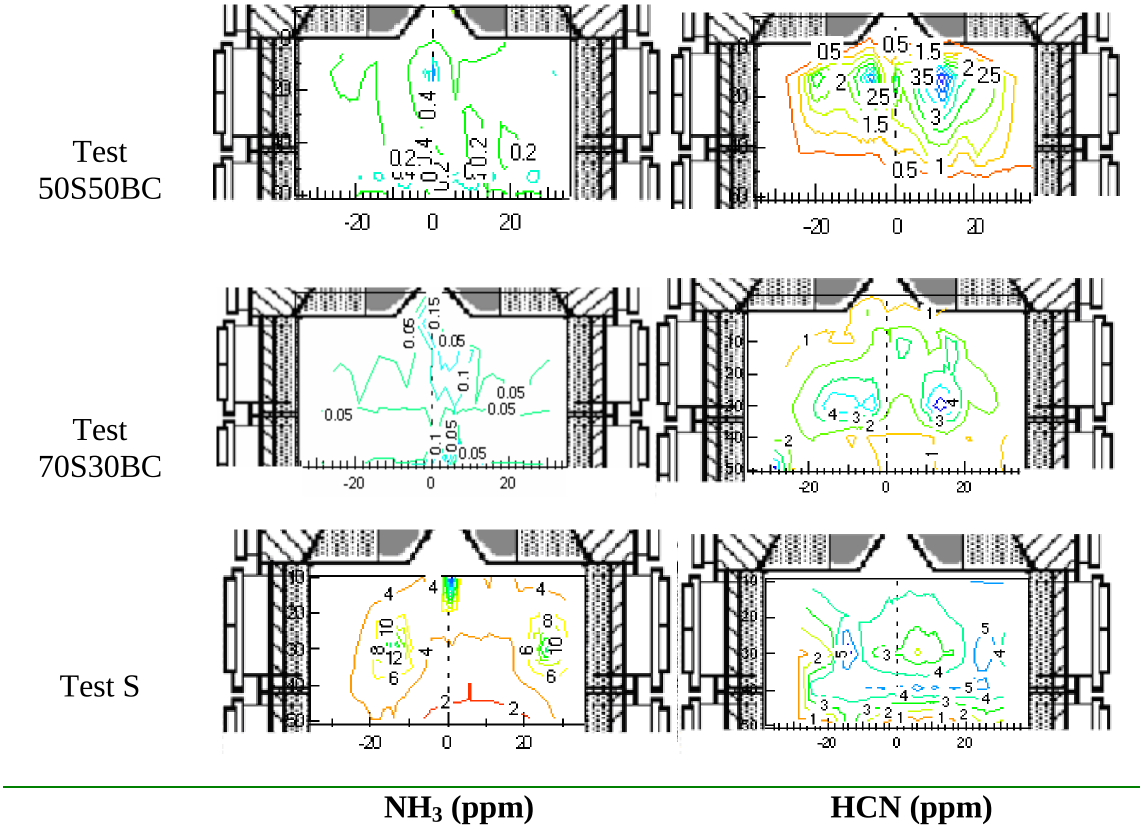

Figure 68 NH3 and HCN maps from Test S, Test 70S30BC, and Test 50S50BC. The unit of radial distance from the centerline is cm.

The low fuel-N content in sawdust leads to NO$_x$ intermediates during combustion that are too low to quantify under these conditions. The maps of HCN and NH$_3$ both exhibit results at or near reliable detection limits (Figure 69). Strictly speaking, the NH$_3$ map sometimes indicates concentrations at or above the detection limit in the measurement region. The peak value in the HCN map coincides with that for NH$_3$. This is attributable to the joint influence of unsteady local flame structure, the turbulent flow pattern and low fuel-N content.

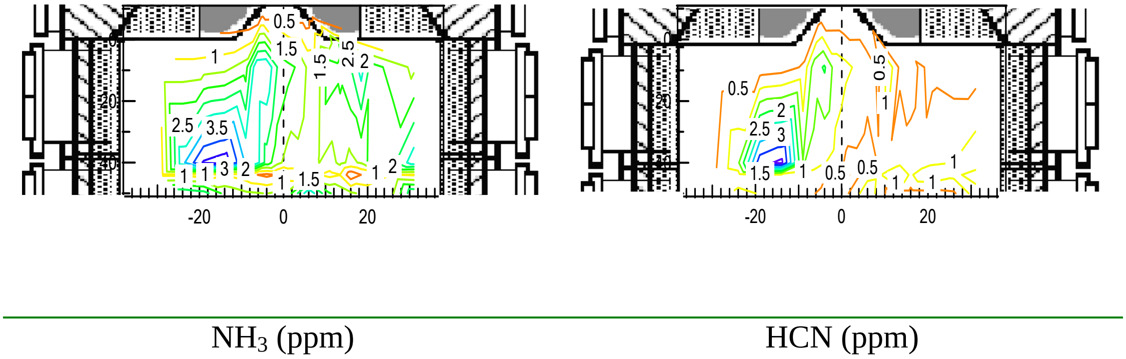

Figure 69 NH3 and HCN maps from Test SD. The unit of radial distance from the center-line is cm.

In the current project, Test P was the last case, and there was not enough fuel left to complete a spatial map, so only measurements along two lines appear (40 cm and 160 cm). Compared to the data from Test SD, neither species in Test P comfortably exceed the detection limits of these instruments during these tests (Figure 70).

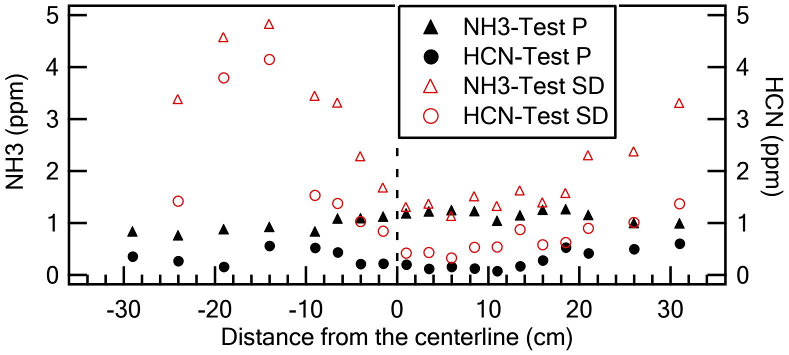

Figure 70 Comparison of NH_3 and HCN data at same position from Test SD and Test P.

In the cofiring case involving sawdust and the Pittsburgh #8 coal, Test 70SD30P, illustrated in Figure 71, the light nitrogenous species profiles have similar characteristics as that from Test SD. This is possibly caused by the high mass fraction of sawdust in the fuel mixture, resulting in the amount of NH3 or HCN released below the measurement limit of the current system.

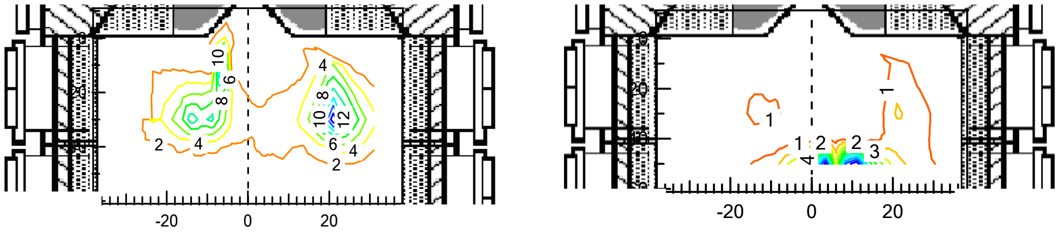

NH_3 (ppm) HCN (ppm)

Figure 71 NH3 and HCN maps from Test 70SD30P. The unit of radial distance from the centerline is cm.

A summary of the NH_3 and HCN maps of all the cases leads to several conclusions as follows:

HCN and NH_3 could be measured in the transient fuel-rich eddies under the overall fuel-lean tests with the intrusive data collection system. CO is much more stable than HCN and NH_3 through the flame front. The light nitrogen species exhibit the same general trend as that of CO. This confirms the existence of HCN and NH_3 in most cases, though several cases included only non-detectable levels.

NH_3 is the dominant fuel-NO_x intermediate detected during straw firing, while HCN is detected in coal flames and blended flames cofiring with coal mass fractions of at least 50%.

4.1.2 Analysis of NO emission data

This section discusses the NO emission data from each combustion test and the impact of cofiring biomass on total NO generation.

NO maps from all the tests appear in Figure 72. They all have similar pattern: the high NO concentrations occur in the combustion region, and in the reacted-gas region NO demonstrates a relatively flat profile.

Test S data exhibit greater NO reduction variation (a NO reduction of nearly 200 ppm) than that of Test SD (about 50 ppm) or any other fuel or blend in the reacted gas region. A careful review of the CO profiles for the straw case (Figure 17, for example) indicates that finite CO concentrations persist much further for straw in the axial direction than for any other fuel. Unlike sawdust, straw contains highly heterogeneous components. Specially, straw knees, which are the joints in the stalk of the plant, are far denser than the bulk of the fuel. Straw knees produce large and relatively dense char particles that require much longer to burnout than does most other parts of the similar particle size. Such residual char particles could be the origin of both the CO and the extended NO chemistry observed in the data. These data are not sufficiently definitive to establish this point, and doing so requires solid sampling, but this is a plausible explanation. This issue will be investigated in some detail in a continuation of this work being conducted by another investigator (Damstedt, et al. 2005). The results from this work will be included in the ongoing PSO project 4881.

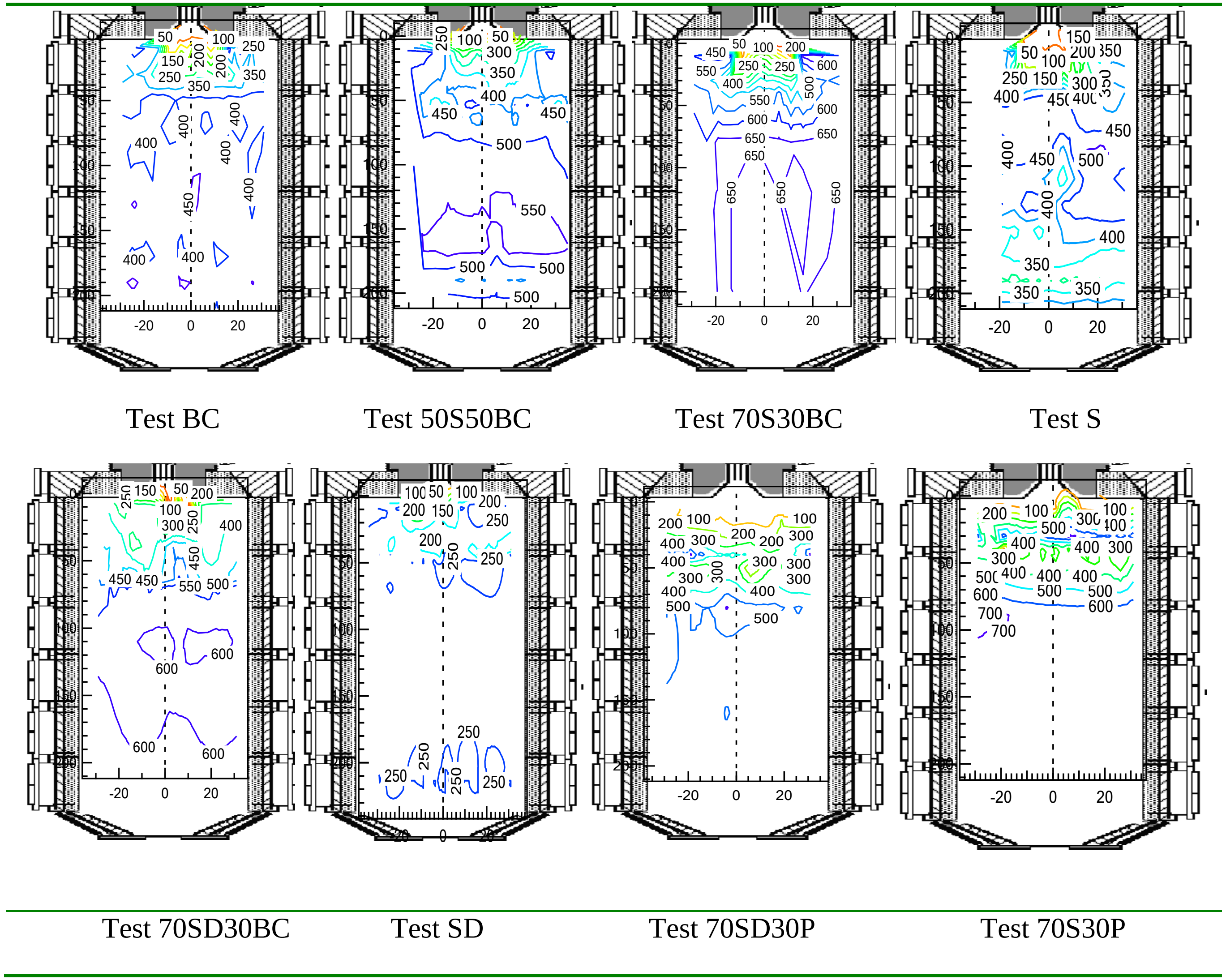

Figure 72 Comparison of axisymmetric NO maps (unit: ppm).

Since the operating stoichiometries are not the same among all the tests. NO emissions from Test BC and other tests are compared on a 3% excess O_2 basis. The normalized NO emission, $Y_{NO,3\%O_2}$, is calculated from

$$Y_{NO,3\%O_2}(ppm) = \overline{Y}_{NO} \frac{21-3}{21-\overline{Y}_{O_2}} \qquad \textbf{Eqn 4.1}$$

where $\overline{Y}_{NO}$ and $\overline{Y}_{O_2}$ are the respective average of NO and O_2 mole fractions across the reacted-gas region.

Changes in stoichiometry represent different degrees of dilution of flue gas components in addition to changes in combustion parameters such as flame temperature and radical concentrations. Normalizing the data to a 3% oxygen basis removes the dilution effects in the data, allowing the combustion impacts to be more clearly evident.

For the examination of the impact on NO emission of cofiring biomass, NO emissions on an energy basis can be determined through

$$Y'_{NO} = \frac{N_{NO} MW_{NO}}{\sum M_i H_i} \qquad \textbf{Eqn 4.2}$$

where N_{NO} is the molar flux of NO (mol/hr) at the exhaust, as calculated from

$$N_{NO} = [(\sum M_i + M_{air})/MW_{mixture}]y_{NO,exhaust} \qquad \textbf{Eqn 4.3}$$

where the symbols are defined as follows.
M_i and M_{air} : the feed rates (kg/hr) of fuel i and air, respectively;
H_i : the lower heating value (as received; MJ/kg) of fuel i ;
$MW_{mixture}$ and MW_{NO} : the molecular weight of exhaust gas mixture (assumed to be 29 g/mol) and NO, respectively.
$y_{NO,exhaust}$: the measured exhaust NO volume fractions;
Y'_{NO} : the amount of NO produced per unit energy of fuel, a more meaningful number from an environmental performance standpoint than the amount of NO produced per unit of flue gas produced, especially when fuel heating values vary as widely as is the case between coal and biomass.

Another term introduced during analysis of NO emissions based on a fuel-N input basis is the fuel-N yield, defined as

$$Y''_{NO} = \frac{Y'_{NO}}{\sum M_i x_{N,i}} \qquad \textbf{Eqn 4.4}$$

where $x_{N,i}$ is the nitrogen mass fraction of fuel i . This parameter represents the amount of NO produced per unit nitrogen in the fuel. Assuming all NO is generated from fuel nitrogen, which is approximately correct for essentially all nitrogen-containing solid fuels, larger values of this parameter indicate greater fuel nitrogen conversion normalized by the heating value of the fuel.

The normalized emissions of all the tests are tabulated in Table 6. The table shows that Pittsburgh #8 has the highest value of $Y_{NO,3\%O_2}$ (668 ppm), followed by straw (561 ppm), which is higher than that of Blind Canyon (504 ppm). Sawdust has the lowest fuel-N content (0.35%, wt, daf) and shows the lowest NO emissions (257 ppm). Cofiring biomass with coal does not necessarily reduce NO emissions on the 3% excess O_2 basis (the basis sometimes used by EPA, among others, for regulations). Two straw cofiring cases, Test 70S30BC and Test 70S30P, show a high $Y_{NO,3\%O_2}$ (665 and 661 ppm, respectively) close to that of pure Pittsburgh #8. Cofiring sawdust with Blind Canyon also increases NO emission compared to that from the pure coal test. Only Test 50S50BC and Test 70SD30P demonstrate a reduction in NO emission compared to the respective pure coal tests.

Table 12 NO emissions in the reacted-gas region during current project

Test ID	$Y_{NO,3\%O_2}$ (ppm)	Y'_{NO} (10^{-2} kg/MJ)	Y''_{NO} (10^{-2} kgNO/MJ/kgN)
S	560.68	4.07	2.47
70S30BC	664.63	3.89	1.91
70S30P	661.45	4.16	1.97
50S50BC	530.06	2.79	1.32
SD	257.14	1.47	2.26
70SD70P	461.19	2.51	1.72
70SD30BC	593.01	3.13	2.27
P	667.68	4.44	2.52
BC	503.54	3.32	2.04

Resulting NO emissions on an energy basis, as included in Table 6.1, indicate that sawdust is once again the lowest NO emitter (1.47e-2 kg/MJ), with its Y'_{NO} less than one half that of other fuels, and its cofiring cases with Pittsburgh #8 drops the emission level by nearly 50%, and a decrease of 18% was achieved when cofiring with Blind Canyon. Because of the relatively high fuel-N content, straw shows a high NO emission close to Pittsburgh #8 and higher than Blind Canyon, and its cofiring cases studied can only achieve a reduction of around 25% (Test 50S50BC) at most. In the higher mass fraction cofiring test with Blind Canyon, NO emission (3.89 e-2 kg/MJ, Test 70S30BC) is even higher than the pure coal test (3.32e-2 kg/MJ).

With respect to yield (Y''_{NO}), the pure biomass tests have the highest NO yields, followed by the pure coal tests, and cofiring can effectively reduce NO emissions. For example, Test 50S50BC has a nearly 40% reduction of NO yields compared to that of Test S on this basis. All cofiring tests were found have lower Y''_{NO} values than their respective pure fuels tests, and this reveals that cofiring can be a potentially feasible method to reduce NO yields on bases of both energy and fuel-N input.

These data show the complexity associated with NO emissions. For example, sawdust produced about half as much NO as the next lowest pure-fuel NO emitter as measured by concentration in the flue gas normalized for dilution. If normalized by fuel heating value, sawdust is still the lowest emitter. When NO per unit energy per unit fuel nitrogen content is considered, sawdust is among the highest emitters of NO.

This analysis shows that nitrogen conversion efficiency to NO is generally higher for NH_3 intermediates (biomass) than for HCN intermediates (coal) regardless whether the actual NO concentrations are relatively high (straw) or low (sawdust). However, fuel properties alone don't account for all of the variation, as indicated by the high NO and conversion efficiency of Pittsburgh #8 coal, presumably because of high temperatures associated with higher heating value and equivalence ratio compared to most other tests.

More insight into NO formation arises by comparing measured NO concentrations during co-firing to the interpolated value based on measured results from pure coal and biomass that comprise the cofired fuel. Results are plotted on a parity diagram, that is, a plot of the interpolated value vs. the measured value. This technique requires three experimental tests, one each for the pure fuels and one of a blend, to establish a single data point. Departures from the diagonal line, where interpolated and measured values are equal, indicate some form of non-linear interaction of the fuels in the combustion environment.

The interpolated NO emissions from cofiring tests could be determined through the summation of mass-weighted data from the respective pure fuels

$$\left(Y_{NO,3\%O_2}\right)_{cofiring} = \sum \frac{\left(Y_{NO,3\%O_2}\right)_{i,pure}}{M_{i,pure}} M_{i,cofiring} \qquad \textbf{Eqn 4.5}$$

where $M_{i,pure}$ and $M_{i,cofiring}$ are the feed rates of same fuel during its single firing and cofiring tests, respectively. The relation between the interpolated and measured NO emission on a 3% excess O_2 basis is plotted in Figure 2. Among the cofiring cases, Test 70S30BC has the best interpolation, with the result point on the diagonal. Other cofiring test show deviations of different level: Test 50S50BC has the highest positive difference of about 28%, with Test 70SD30P 20%, Test 70S30P 14.5%, and Test 70SD3BC a negative deviation of -22%. This is opposed to the previous results from a non-swirling burner (Baxter 2002), as shown in Figure 74 , which suggests that the total NO emission from the cofiring case can be interpolated from the NO emission data from the respective pure fuel tests. The complexities of aerodynamics, stoichiometric variations, and temperature variations inherent in the swirl-stabilized results combine to produce results that differ from interpolations of pure fuel behavior. If these complexities are eliminated, as in the previous data, and only parallel flow reactions are considered, NO chemistry is seen to be primarily a function of the pure fuel behavior. However, these latter tests are much better representations of commercial boiler behavior than are the former tests with idealized flow, stoichiometry, and temperature trends.

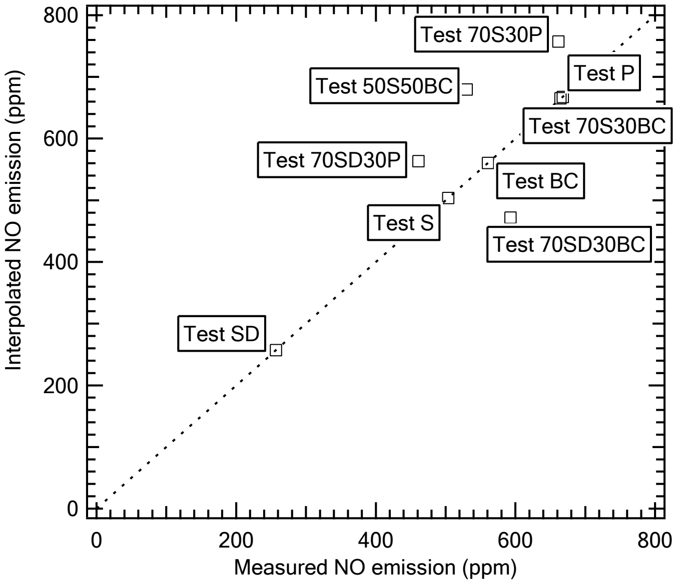

Figure 73 The relation between the measured and the interpolated NO emissions (mole fraction on a 3% excess O2 basis) in the present project.

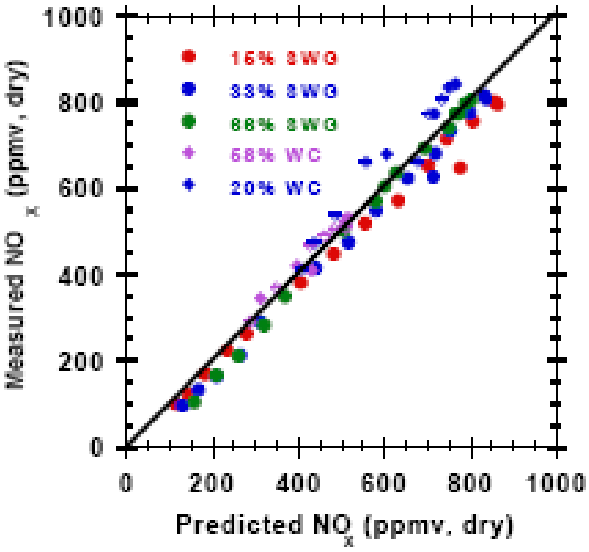

Figure 74 The relation between the measured and the interpolated NO emissions in a non-swirling flow burner (Baxter 2002).

During pulverized fuel, swirling flow combustion in the BFR, NO formation is dominated by gas-phase reactions. After the release from the condensed phase, the gas species and their reactions are independent of the parent fuels. Therefore, the deviation of the cofiring data from the diagonal in Figure 2 is caused by the complex temperature field and highly turbulent flows. The reverse flow predicted with modeling shows all the tests are of similar flow patterns, but the difference in the IRZ size is obvious among the tests. Other details such as changes in local instantaneous velocity can have a tremendous impact on the combustion stoichiometry and instantaneous temperature, resulting in the complexity of gas-phase reactions. Thus the deviation is attributed to the turbulent, complex flow and temperature fields in the swirling region but not the solid fuel interactions. A further analysis of the 1-D profiles is necessary to clarify NO formation in the combustion region, as discussed in the next section.

4.1.3 1-D profiles of NO

NO normalized mole fractions from each test demonstrate a generally monotonic increase with increasing axial position, as seen in Figure 75. From 10 to 20 cm, NO from both biomass tests increases following the sharp increase of CO_2 (Figure 17 as the pure fuel tests data, and Figure 19 as the cofiring data), which is caused by the larger amount of volatile off-gas combustion, as discussed earlier. Results from pure fuel tests show a relatively flat pattern in the reacted-gas region.

Sawdust has much lower nitrogen content (0.35%, wt, daf) than straw (0.91%, wt, daf), and their carbon contents are similar. Therefore, Test SD has a much lower NO generation but similar CO_2 formation.

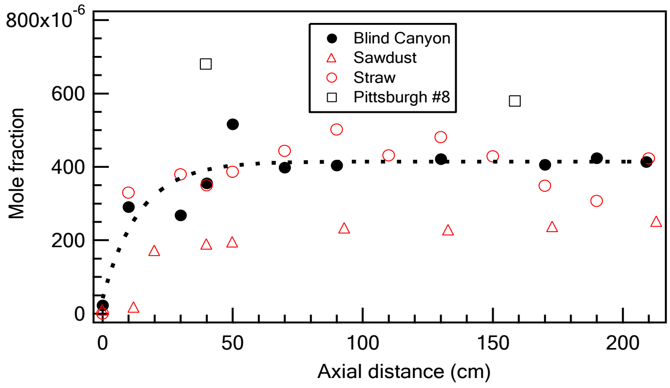

(a)

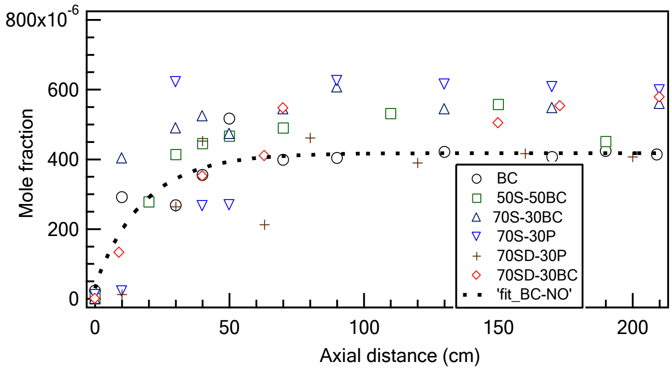

(b)

Figure 75 NO 1-D profiles from pure fuel tests (a) and cofiring tests (b) (The lines show the trends of normalized results of Test BC along the reactor axis)

The nitrogen species data collected, together with CO, CO_2, and O_2 spatial profiles, consistently reveal the characteristics in biomass swirl-stabilized flames. These data provide excellent validation criteria for future comprehensive low-grade fuel combustion models.

4.1.4 Kinetic evidence on the fate of NOx intermediates

Based on currently available theory and computing capability, it is not feasible to develop a comprehensive swirling flow solid-fuel combustion model containing both detailed fluid mechanics and elementary reaction mechanisms. The primary complicating factor is chemical kinetics and the limitations in expressing such kinetics are both theoretical and computational. Non-premixed models reasonably approximate rapidly reacting systems, but they are not appropriate for reactions with time constants that approximate or are slower than the turbulence time scales. Several important species are involved in such reactions, including NO_x, CO, and SO_2, and soot. CFD models usually do not include full chemical kinetics as is the case in FLUENT^{TM}. As described in (Kær, Rosendahl and Baxter, 2006), the fuel-NO_x model built in FLUENT^{TM} is not able to reveal the difference in the fate of the important intermediates, NH_3 and HCN. Detailed kinetics calculations with simplified flow dynamics illustrate the potential impact of different intermediates (HCN and NH_3) on NO formation in this section.

The intention of the detailed modeling work is to develop quantitative descriptions of relative reactivities that are useful in interpreting the measured data. Specifically, the relative thermal stabilities and chemical reaction rates of HCN and NH_3 in combustion environments similar to those in the current investigation can be investigated using detailed chemical kinetics and, despite the absence of turbulent fluctuations in the calculations, qualitatively indicate which species are most stable.

CHEMKIN is a collection of data bases, programs and subroutine libraries written in text files and in FORTRAN code that is widely used in such investigations. It incorporates complex chemical kinetics into simulations of reacting flows. As a powerful set of software tools, CHEMKIN facilitates the formation, solution, and interpretation of problems involving gas-phase and heterogeneous (gas-surface) chemical kinetics, equilibrium, and transport properties.

In this project, CHEMKIN was used to analyze the fate of the NO_x intermediates, HCN and NH_3, at different temperatures representing both the fuel-rich region and the flame front in the BFR. Two detailed mechanisms are considered in the calculations: Kilpinen 97 (Kilpinen 1997) and GRI-Mech 3.0 (Smith, et al. 2000). The Kilpinen 97 mechanism has been largely validated by the biomass gasification data mentioned earlier. The GRI-Mech 3.0 is the most recent and most comprehensive version of the mechanisms developed at the Gas Research Institute.

The detailed kinetic mechanisms do not include the effects of turbulence on the reaction, which is expected to be significant in this mixing-limited combustion application. We do not anticipate quantitatively accurate predictions from CHEMKIN when applied to the complex flows in the BFR. However, results from CHEMKIN calculations are able to explain qualitative observations in the data based on best-available mechanisms for gas-phase NO_x formation. Specifically, we anticipate that the CHEMKIN results will help establish whether the form of nitrogen evolved from the fuel substantially impacts either nitrogen intermediates or ultimate NO_x concentrations.

In the BFR, HCN and NH_3 are resident in transient fuel-rich eddies and oxidized within the flame front. In the former case, HCN and NH_3 exist with carbon monoxides, steam, and other relatively stable species, and are only slightly oxidized because of the scarcity of O_2, and reactions involving HCN and NH_3 include their thermal decomposition. The flame front is rich in radicals and produces the highest temperature. Therefore, oxidation reactions are more significant for the intermediates in this region. One of the purposes of kinetic calculations is to compare the stability of HCN and NH_3 under conditions simulating both the fuel-rich region and the flame front. The other intention is to analyze the difference in their conversion to NO in the flame front. The latter can be achieved through analysis of total fixed nitrogen (TFN), which is the summation of all nitrogenous species except N_2.

The detailed initial gas mixture compositions appear in Table 13. For a comparison of the thermal stability, the gas species mixture is assumed to include equal amounts (mole fractions) of HCN and NH_3, C_2H_2, CO, and similar CO_2 and H_2O contents, with the balance of the mass as $N_{2,}$ (Case 1). With respect to the intermediate's stability in the flame front, OH radicals are introduced to represent radicals penetrating the flame, and CO and C_2H_2 represent the devolatilization off-gases, with a supply of O_2. As for the comparison of conversion of HCN and NH_3 to TFN, either HCN or NH_3 is defined as the only NO_x intermediate in the gas mixture under flame front conditions (Case 2 and Case 3). The calculation was carried out with temperatures ranging from 1600 K to 2400 K.

Table 13 Compositions of the initial gas mixtures in the kinetic simulations

	Case 1	Case 2	Case 3
	Fuel-rich core	Flame front	Flame front
HCN	8.35e-4	8.35e-4	0
NH_3	8.35e-4	0	8.35e-4
H_2O	0.15	0.15	0.15
OH	0	0.01	0.01
CO_2	0.15	0.15	0.15
C_2H_2	1.00e-3	0.10	0.10
CO	1.00e-3	1.84e-3	1.84e-3
O2	0	1.08e-3	1.08e-3
N_2	Balance		

The calculation results with the Kilpinen 97 and GRI-Mech mechanism are almost the same for each case considered. Therefore, results from the simulations with the Kilpinen 97 mechanism are discussed here. The GRI-Mech 3.0 calculation results are listed in (Kær, Rosendahl and Baxter, 2006).

The comparison of the thermal stability of HCN and NH_3 in the fuel-rich region is illustrated in Figure 76. Results from the detailed mechanism show that the decomposition rate of both species increases with increasing temperature, as indicated by time needed to consume the NO intermediates. At 1600 K, there was almost no change in the NH_3 and HCN concentrations during the first 0.05 s. With the process continuing, the amount of HCN begins dropping and NH_3 remains essentially unreacted through the remaining time examined (up to one second). At 1800 K, both species concentrations display a decrease after a reaction time of 0.01 seconds, and reach 1 ppm within 0.5 s. At 2400K, the time required to achieve same reduction of species concentration is about 2 ms. The logarithmic scales somewhat underemphasizes the significant difference in thermal stability at the lower temperatures. These calculations show that NH_3 has greater thermal stability than HCN in the temperature range 1600-2200K, with the difference increasing as T decreases.

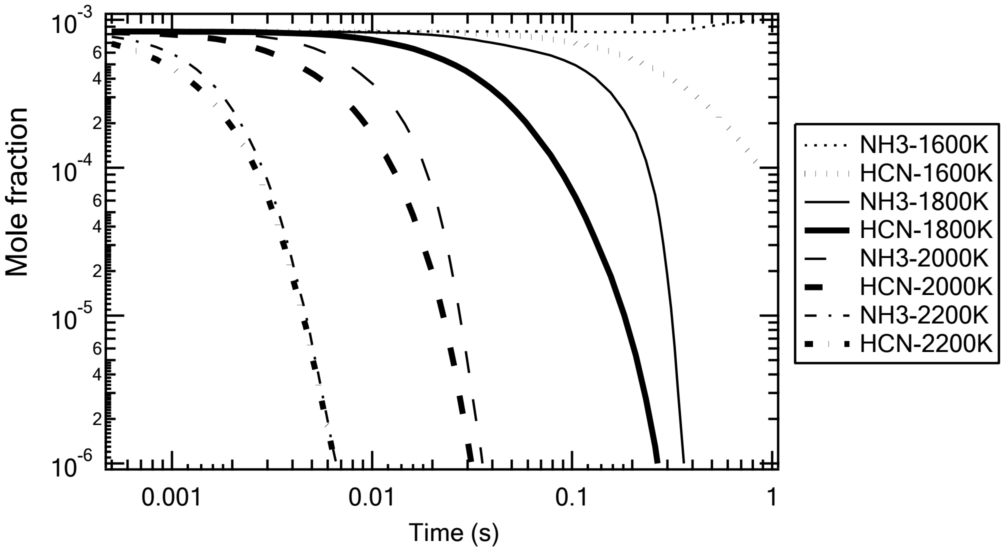

Figure 76 Comparison the thermal stability of HCN and NH3 in the fuel-rich region with the Kilpinen 97 mechanism.

Under the same operating temperatures, the opposite result is found in flame front conditions. HCN shows higher chemical stability (reacts more slowly) than NH_3 throughout the flame front region, with the results from Case 2 and Case 3 shown in Figure 77. Both species react much faster compared to reducing conditions at the same temperatures. The consumption rates of both species increase with increasing operating temperatures.

The NO_x intermediate maps discussed earlier are consistent with the calculation results in the fuel-rich region. Because most biomass fuel-nitrogen resides in the form of acyclic compounds like amine or amide derivatives, NH_3 is the dominant intermediate found in the combustion region during pure biomass tests and most cofiring cases with a biomass mass fraction of 70%. During these tests, more NH_3 than HCN is released during devolatilization in the fuel-rich region, and because of the scarcity of oxygen, the thermal decomposition of the intermediates should prevail. NH_3 is more thermally stable than HCN at temperatures between 1600 K and 2000 K (which is typical for low-grade fuel flames), thus it should be found as the dominant NO_x intermediate in the fuel-rich core. Furthermore, thermal decomposition of NH_3 is less effective than HCN, leading to higher NH_3 concentrations than HCN concentrations as the combustion gases enter the flame front.

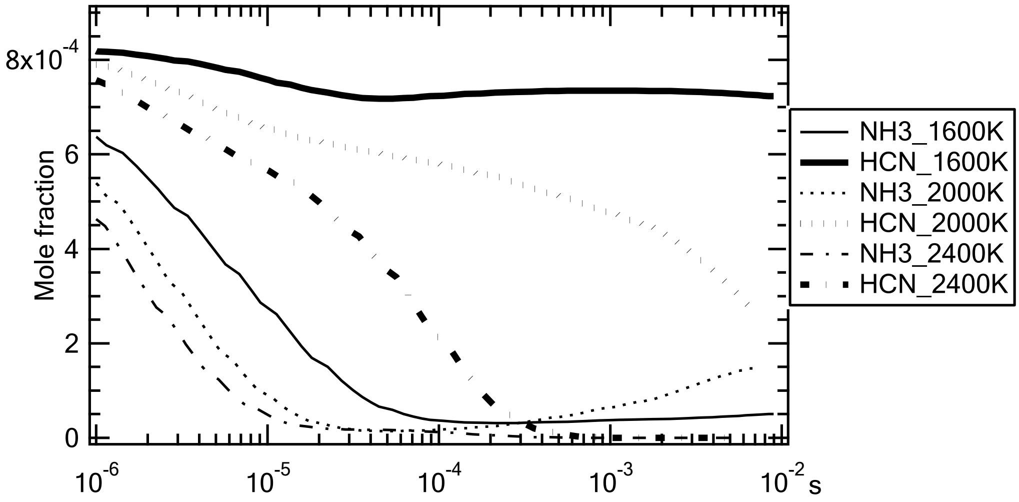

Figure 77 Comparison the chemical stability of HCN (Case 2) and NH3 (Case 3) in the flame front with the Kilpinen 97 mechanism.

At the flame front, both intermediates are consumed quickly through oxidation. NH_3 reacts faster to form NO than does HCN at short reaction times (up to 0.1 ms). At long times, both species approach their equilibrium NO concentrations, which are independent of initial composition. This indicates that NO formation in thin flames is more significant for NH_3 than HCN, though both react to form NO.

The NO formation potential in the flame fronts of HCN and NH_3 can be compared through monitoring respective TFN (the sum of all the nitrogen species but not N_2) and NO profiles from Case 2 and Case 3. The calculation results appear in Figure 78. HCN and NH_3 have the same conversion to TFN under temperatures studied, and the conversion increases with temperature. Since NH_3 is more reactive than HCN, more NO is generated from NH_3 during the initial stage. The time required for NO to reach the peak level decreases from 0.2 ms (1600K) to 0.02 ms (2200K). Under 2400 K, the further increase of TFN is caused by thermal NO_x formation. Another interesting result is that NO accounts for nearly 100% of TFN after a reaction time of 0.05 ms when temperature is higher than 1600K. Below 2400K, the profiles of TFN generally show a flat pattern, indicating that all the intermediates were converted into NO. Mole fractions of both TFN and NO show a slightly decrease with longer reaction time, and this is because more TFN is converted into N_2.

From kinetics calculations, NH_3 is found more thermally stable and chemically reactive than HCN, and NH_3 more rapidly forms NO in the early stages of reaction. These theoretical results are consistent with the observations in Table 6, where NH_3-forming fuels exhibit relatively high fuel nitrogen conversion efficiencies to NO relative to most other fuels.

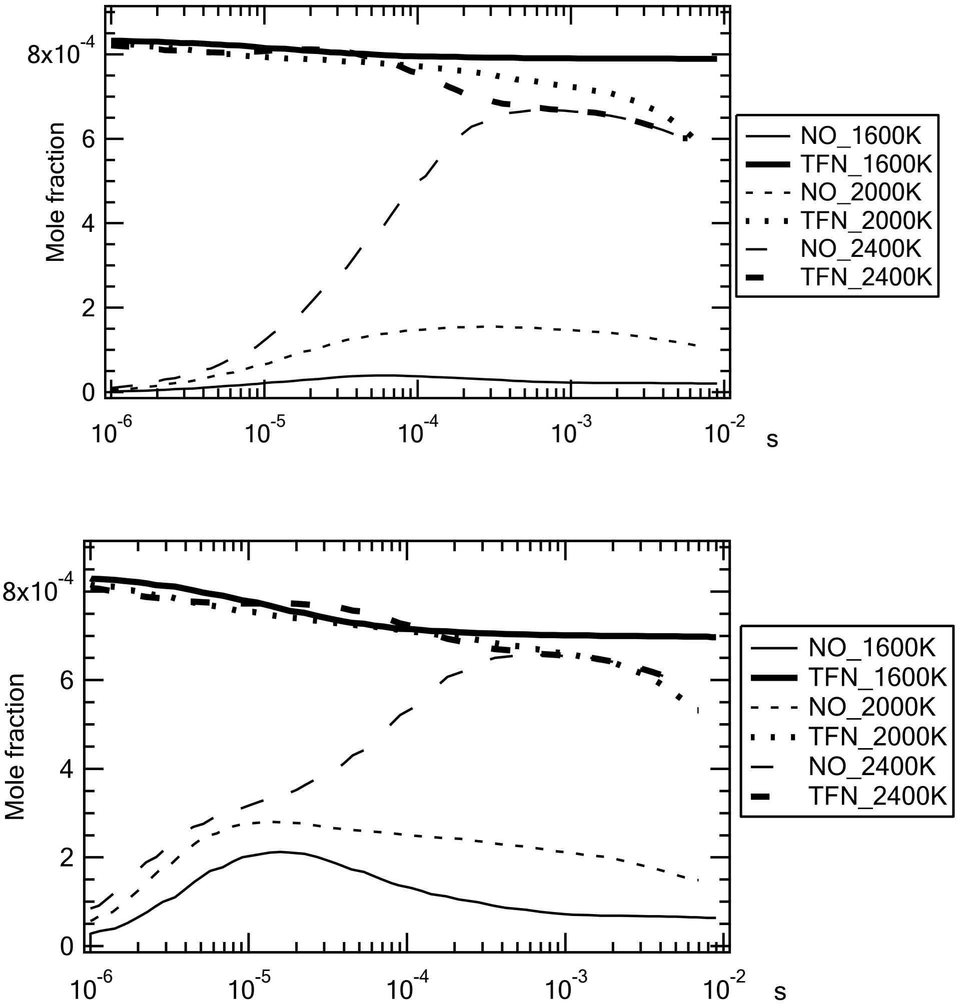

Figure 78 The profiles of TFN and NO from cases where only one type of NOx intermediate exists in the initial mixture, with lines representing results from HCN mixtures (Case 2) and markers denoting NH3 blends (Case 3) with the Kilpinen 97 mechanism.

4.1.5 Summary

This information is summarized as follows. More practical and succinct summaries of design and operating guidelines for cofired low-NO_x burners appear later.

Low-grade fuel combustion in the swirl-stabilized burner

The BFR capably operates during both dedicated biomass firing and cofiring biomass with coal in addition to pure coal tests for which it was previously used. Under the conditions studied, all low-grade fuel combustion in the swirling flow burner develops a stabilized combustion zone near the inlet followed by a relatively flat reacted-gas zone. Under overall fuel-lean conditions, intrusive measurements reveal the existence of a transient fuel-rich eddies. The existence of an instantaneous fuel-rich region is evident by the detection of HCN/NH_3 and high amounts of CO in the swirling flow region even though the average O_2 concentration is greater than zero. Notably, no region exists in any test in which average O_2 concentrations are zero. The data sets collected are generally repeatable and consistent, and provide excellent validation criteria for future development of comprehensive combustion models.

Biomass firing and cofiring compared to coal combustion in swirling flows
Predictions show that here are no dramatic qualitative changes in flow patterns in the swirling flow during biomass tests compared to coal test, though details differ. All flows show centerline and corner recirculation zones that stabilize the flame near the burner outlet. However, biomass combustion in swirling flows has an expanded combustion region resulting from more particle penetration and high volatile yield. The small and dry biomass particles (compared to commercial fuels) penetrate the flame further into reactor to complete devolatilization and oxidation. High-volatile yields contribute to the larger and more intense fuel-rich (CO-laden) regions.

NO formation from the cofiring cases
In the gas species 1-D and axisymmetric profiles, NO follows a similar pattern to that of CO_2, indicating that NO formation is more mixing limited than kinetically controlled under the conditions studies. Combustion of sawdust shows significant lower NO production on an energy basis primarily because of its low nitrogen content.

Biomass and coal have different stable NO_x precursors. HCN is the prevailing fuel-NO_x intermediate in coal flames, and NH_3 is predominant in the straw and possibly sawdust flames. The form of nitrogen impacts NO formation mechanisms and emission concentration. Biomass generates more NH_3 and less HCN than coal, and the dominance of NH_3 in biomass combustion increases the amount of fuel-N converted to NO under swirling flow conditions. Kinetic calculations show that NH_3 is more thermally stable than HCN in the combustion region and more reactive within the flame fronts. Both HCN and NH_3 show similar conversion efficiency to NO in the reacted-gas region.

4.2 Subtask 4.2: Verification of CFD model against existing full-scale data and application to advanced plants

Focus in this task was put on the comparison of model predictions with existing data from the full-scale testing at the Midtkraft power station unit 1 (MKS1) (Hansen, et al. 1996) (Andersen 1998). During 1996-1997 experimental data was collected during operation at 50%, 75% and 100% loads and biomass shares (thermal basis) of 0%, 10% and 20%. Temperatures as well as main gas species were collected at the locations indicated in Figure 79.

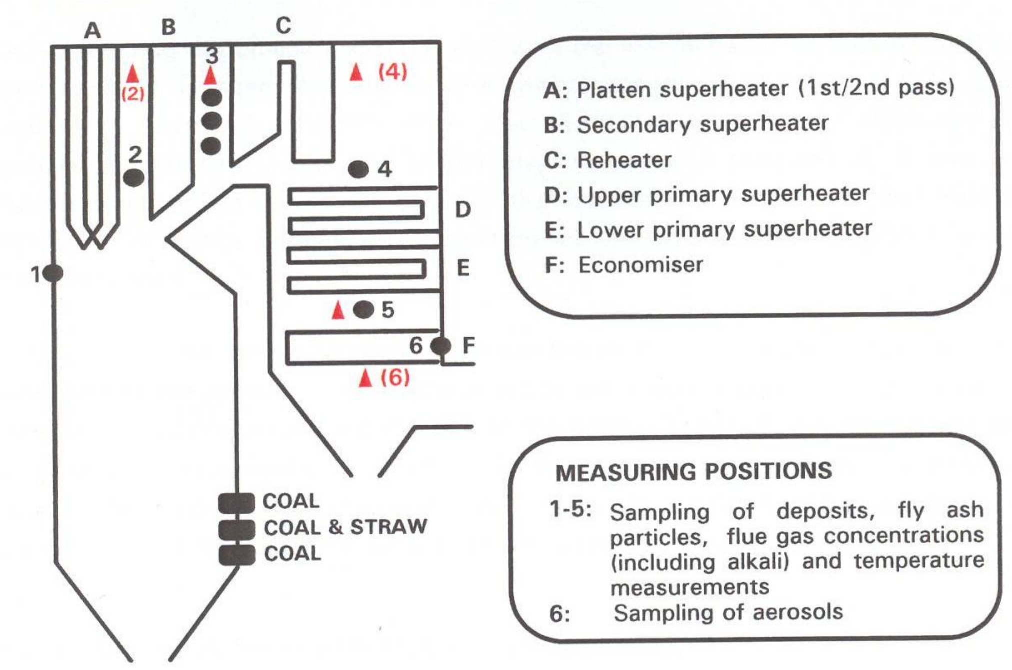

Figure 79 Illustration of MKS1 showing measurement locations

In addition fly ash particles were sampled, deposits collected and aerosol and alkali measurements performed. Although useful for the overall assessment of deposition behavior, the data available is insufficient for comparison with CFD predictions to be meaningful.
The measured temperatures at points 1 through 5 shows very limited variation with straw share within the range investigated (see Figure 85). The variation with load is slightly more pronounced in particular at locations 1 through 3. Based on these observations it was decided to limit the CFD simulations to the following three cases:

Case 1 representing 100% load and 100% coal firing

Case 2 representing 50% load and 100% coal firing

Case 3 representing 100% load and 20% straw (thermal basis) cofiring

The combination of these cases ensures that the CFD model is tested in the broadest range of operational conditions possible and the ability to capture part load and cofiring conditions demonstrated.

4.2.1 Model setup

The full-scale simulations of the MKS1 boiler were made based on a computational grid consisting of 1.4 mio. hexahedral volumes. The platen and secondary super heaters were modeled as slabs with a thickness corresponding to the tube diameter. The remaining tube banks were included as porous regions with a prescribed pressure drop and heat uptake. An outline of the modeled geometry appears in Figure 80.

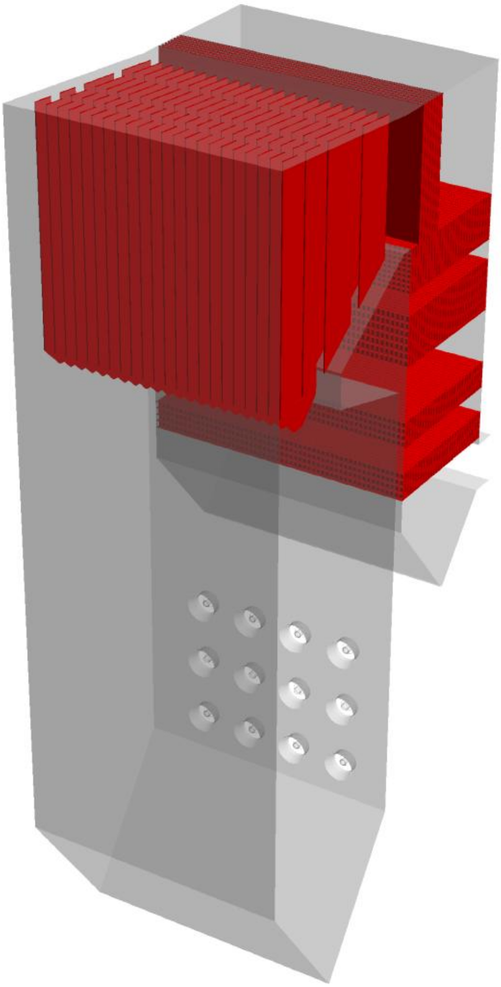

Figure 80 Outline of the MKS1 CFD model

The simulations were based on standard models including the k-ε model for turbulence closure, the SIMPLE algorithm and the Second Order Upwind differencing scheme. Gas phase reactions were modeled using the Eddy Dissipation Model available in FLUENT™ including O_2, H_2, CO, CO_2, CH_4, H_2O and N_2 as species. The reaction between CH_4 and O_2 was assumed to form CO as an intermediate species. H_2 and CO were assumed to react with O_2 forming H_2O and CO_2, respectively.

The solid particle transport and conversion was modeled using a Lagrangian approach with particle compositions based on the proximate and ultimate fuel analyses. The particle size distributions were based on previous experience and measurements (Rosendahl, et al. 2007) following the same approach as previously reported in (Larsen 2004). The straw particles were approximated with a Rosin-Rammler distribution as shown in Figure 81 and a separate fraction with a higher density accounting for the straw “knees”.

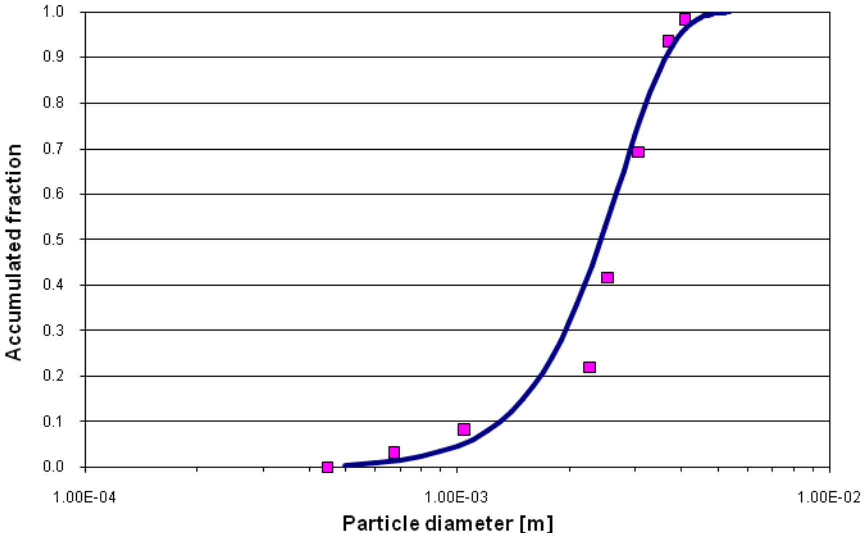

Figure 81 Straw particle size distribution with fitted Rosin-Rammler distribution

The chemical composition of the volatile gases was based on chemical equilibrium. Figure 82 shows the composition for a typical coal as function of temperature.

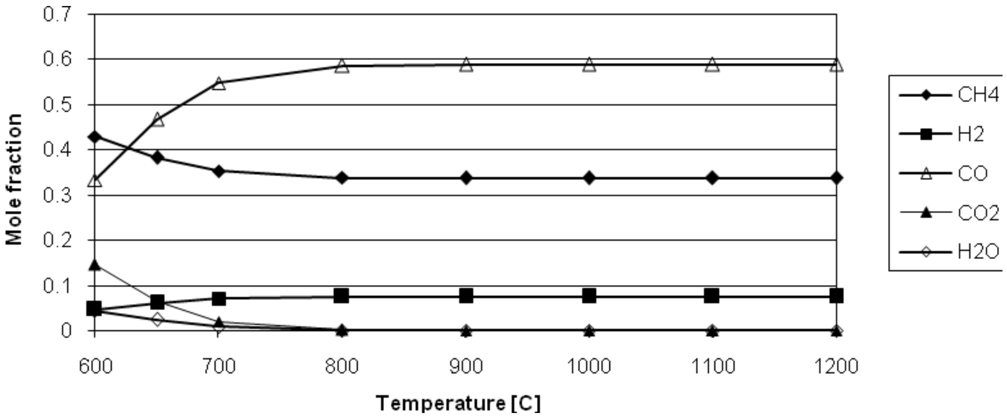

Figure 82 Chemical equilibrium compositions of coal volatiles

As seen, the equilibrium composition does not change as the temperature exceeds approximately 800°C. In the calculations reported here this composition was used for coal volatiles. As straw volatiles are released at lower temperatures than coal volatiles, a similar calculation was made for straw at 550°C leading to a composition with the following mass fractions:

Table 14 Straw volatiles composition estimated from equilibrium

Species	CH_4	H_2	*CO*	CO_2	H_2O
Mass fraction	0.215	0.02	0.250	0.465	0.05

It is not possible to specify multiple volatile species in the standard FLUENT™ particle combustion model. As a workaround, instead of using just one single particle stream 5 streams were defined each representing one of the volatiles species. The flow rate of the injection was set based on the fraction given in Table 14 multiplied by the total particle flow rate.

For solid walls, the thermal boundary conditions were estimated from available steam data. For the porous regions representing tube banks heat sinks were calculated from the steam data. For the 50% load case these heat sinks were also reduced to 50% of the full load data.

Flow rates of fuel and air were based on data retrieved from the boiler operation log files. These are reported in appendix A.

One important note to be made on the boundary conditions is the fact that the direction of swirl is similar for all burners. In most boilers, the direction of swirl is alternating between neighbor burners both horizontally and vertically. This fact that all burners have the same swirl direction has a pronounced influence on the flow and temperature patterns in the furnace as will be shown below.

4.2.2 Thermal conditions

In this section, the overall temperature pattern in the boiler will be illustrated first followed by a more detailed comparison with measurements. The predicted temperature fields for pure coal firing at full load and 50% load are illustrated in Figure 83 by cross-sections at three vertical locations. The first location is in the middle of the cofired burner level, the third is at the level of measurement port 1 and the second is approximately halfway between the first and the third planes.

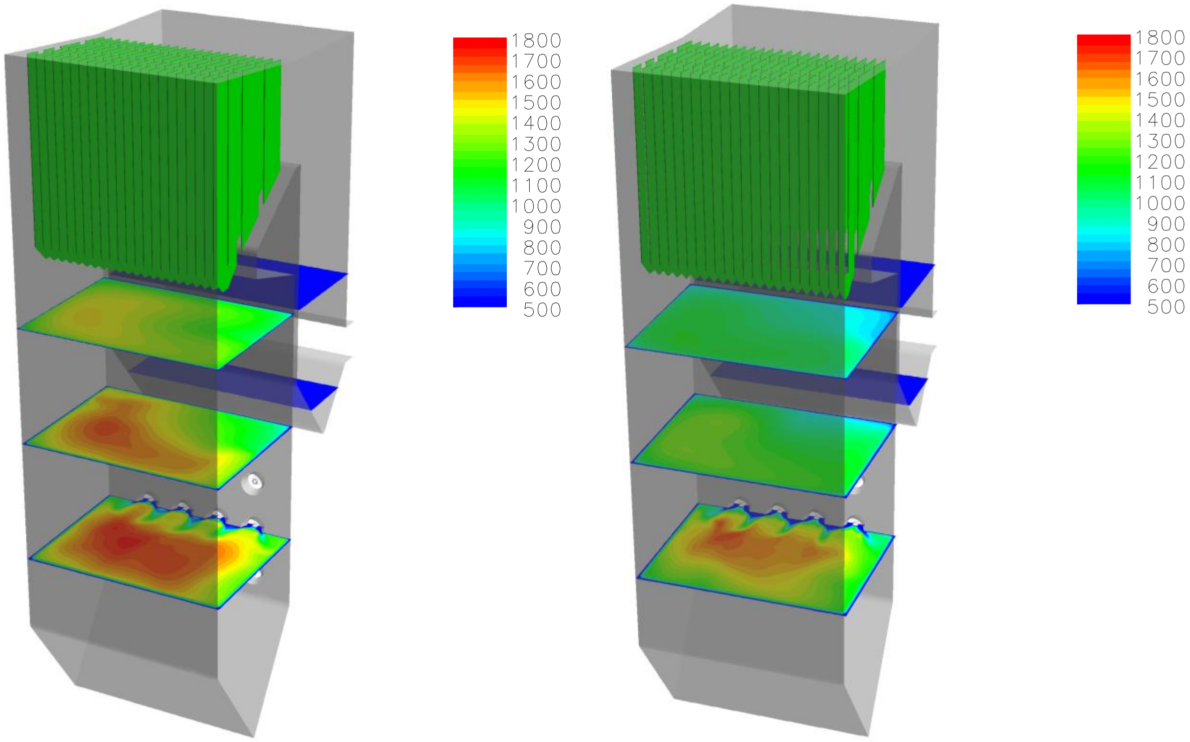

Figure 83 Predicted temperature fields (centigrade) for pure coal firing at 100% load (left) and 50% load (right)

Seen from the front wall, the temperature is significantly higher in the left hand side of the furnace. As mentioned above, the highly skewed temperature distribution in the furnace is caused by the burner swirl pattern. Comparison of the full load with the part load case reveals significantly lower temperatures in the latter. The peak temperature in the near burner region is approximately the same but the extent of this high temperature region is smaller and the temperature level has dropped significantly at the second plane.

The temperature patterns for the coal firing and the straw-coal cofiring are compared in Figure 84. At the two upper levels there is almost no difference in predicted temperatures. From the lower cross-section that cuts through the cofired burners a very significant difference is evident. The significantly larger biomass particles combined with the centre air used for pneumatic transport has a pronounced impact on the near burner zone. The relatively cold stream of straw and air penetrates the internal recirculation zone in front of the burner as seen by the blue color in the quarl regions. The influence on the near burner zone will be investigated in further detail in Section 4.2.3 in terms of predicted oxygen concentrations.

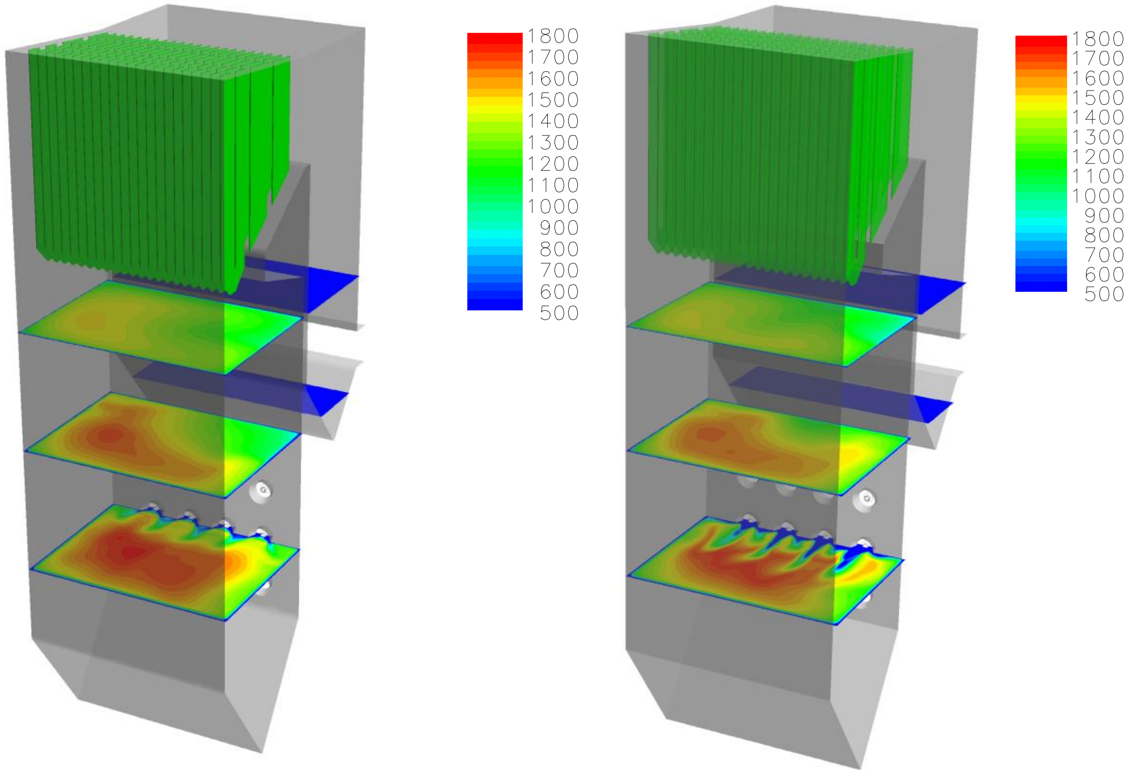

Figure 84 Predicted temperature fields (centigrade) for coal firing (left) and straw-coal cofiring (right)

A quantitative comparison of predicted and measured flue gas temperatures for the three cases considered is presented in Figure 85.

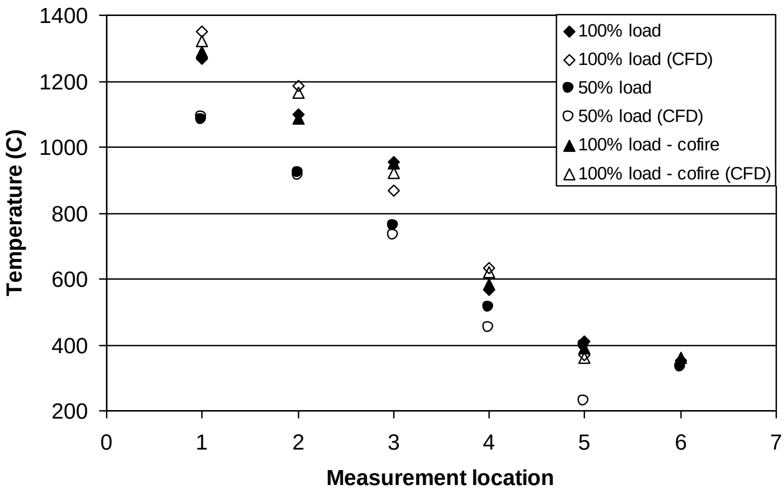

Figure 85 Comparison of measured and predicted flue gas temperatures

Overall very good agreement between measurements and predictions is found at all locations. For the two full load simulations the predictions are slightly higher than the measurements at locations 1, 2 and 4 whereas the opposite is the case at location 3. The variation between the coal firing and the cofiring cases is negligible in both the measurements and the predictions. For the 50% load case the agreement is even better in particular at locations 1 through 3 and the considerable difference compared to full load is well captured in the simulation. The excellent agreement between measured and predicted temperatures found in these three cases is better than can be expected from CFD simulations in general. There is a significant local variation in predicted temperatures around the expected measurement locations which alone suggests that the uncertainties related to the probe locations may exceed the uncertainty level suggested by Figure 85. Similar points can be made with respect to the experimental uncertainty that is likely to exceed the difference between measured and predicted temperatures.

Considering local temperature variations an interesting feature can be seen from the temperatures in the region of the pendant super heaters. Online temperature measurements are reported for the two locations indicated by open symbols in Figure 86.

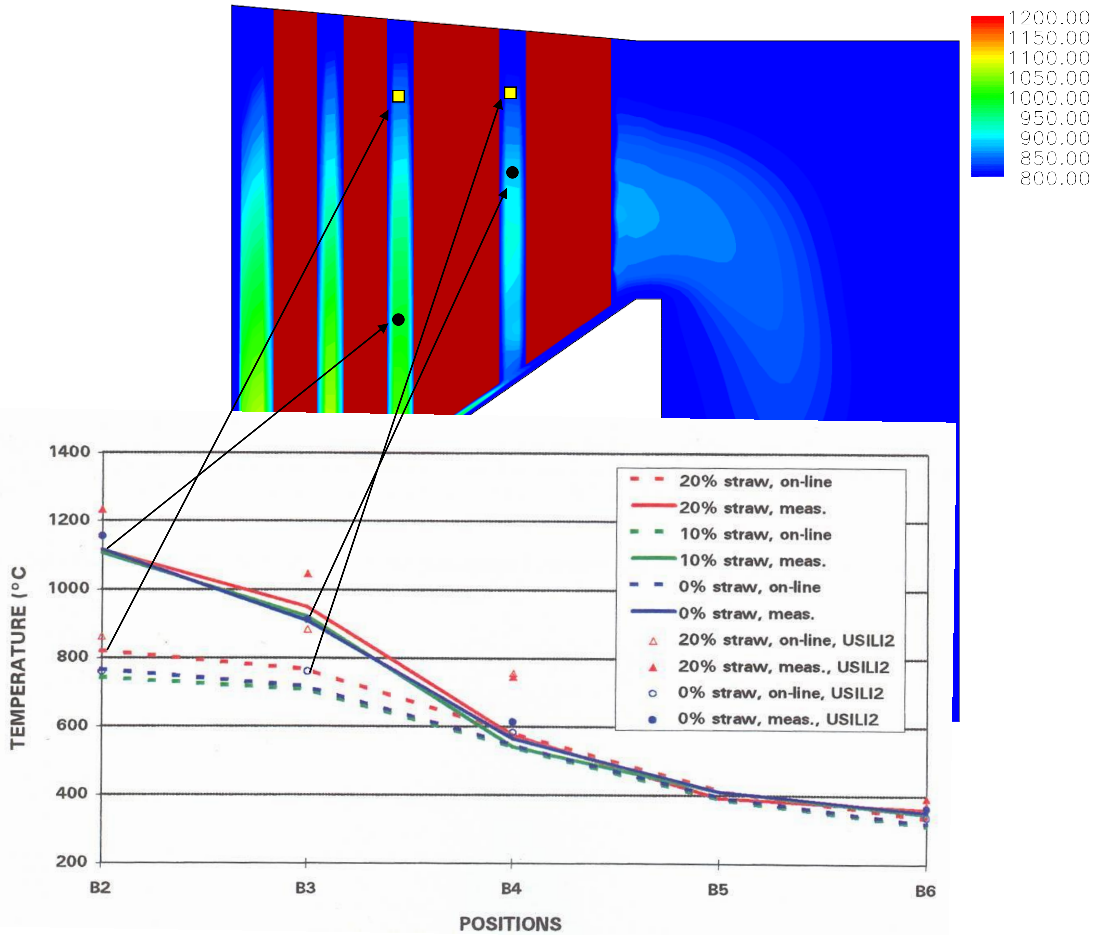

Figure 86 Temperature cross-section in the upper part of the boiler

When comparing the temperatures at these locations with only a relative small distance between them a noticeable difference is seen. This was also pointed out by (Andersen 1998). From the simulation this difference can be explained as being caused by the overall flow pattern in this region. The ability to capture this feature of the temperature patterns brings further confidence to the predictive capabilities of the model.

The overall heat flux to the heating surfaces is another parameter of significant interest. A comparison between predicted heat fluxes and corresponding data calculated from the boiler steam data is presented in Table 15.

Table 15 Comparison of heat fluxes calculated from steam data and CFD predictions

	Boiler data	CFD – coal firing	CFD - cofiring
Platen super heater	58 MW	57 MW	56 MW
Secondary super heater	27 MW	20 MW	19 MW

The model is found to predict the heat uptake by the platen super heater very well. There is no significant difference in predicted values between the coal and the straw-coal cofiring cases. For the secondary super heater the predicted heat uptake is too low for both full load cases. This difference is closely related to the wall temperature and emissivity specified in the simulation. It has not been attempted to adjust this value to obtain better agreement with the steam data.

4.2.3 Gas species

An interesting feature of the near burner fields can be seen from Figure 87 showing the mole fraction of oxygen in cross sections through a coal burner (upper) and a cofired burner (lower). The coal burners in the upper level show the reducing zone in the near burner region typical for swirl burners. The cofired burners on the other hand are characterized by high oxygen concentrations in front of the burner mouth followed by a reducing zone relatively far from the quarl. This pattern was also found in previous investigations of cofired burners (Larsen 2004).

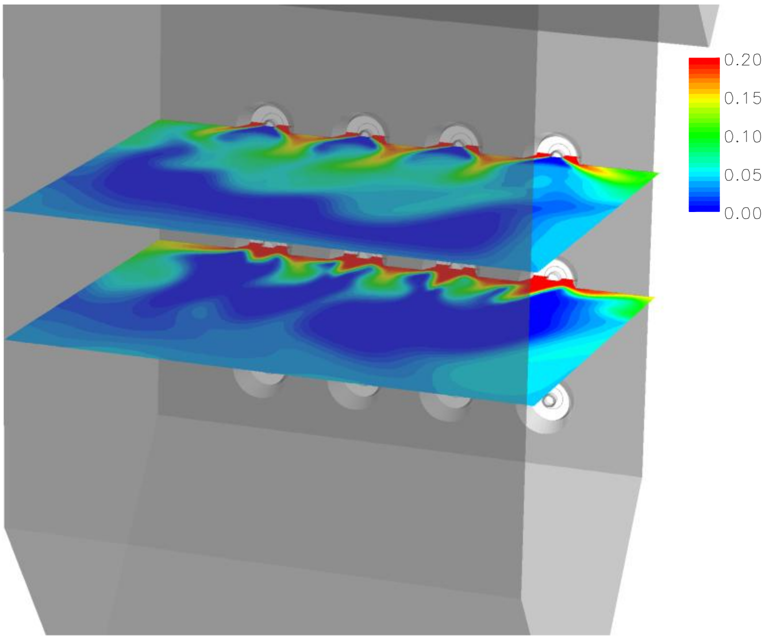

Figure 87 Illustration of oxygen mol fractions in the near fields of coal (upper) and straw-coal cofired (lower) burners

A quantitative comparison of CO_2 concentrations appears in

Figure 88 for the first three measurement locations during coal firing at full and 50% loads.

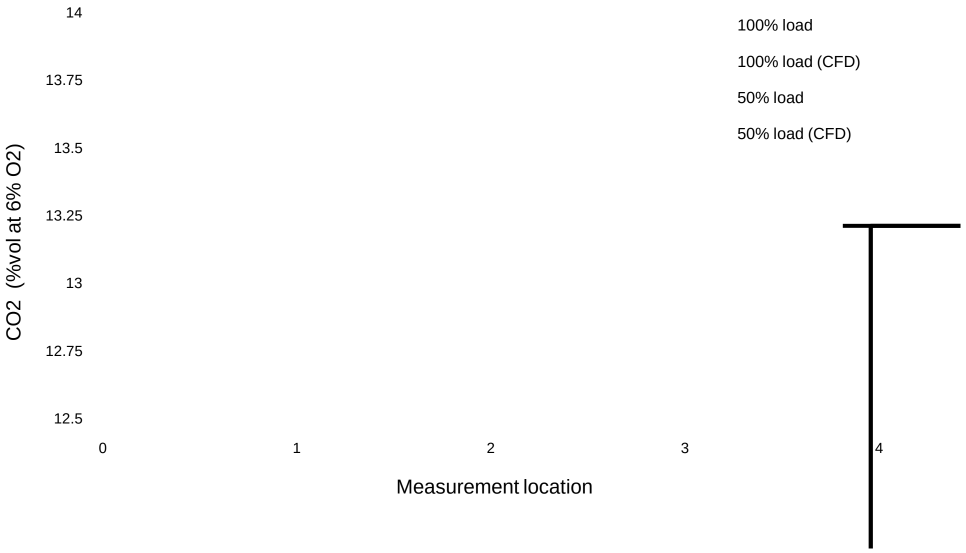

Figure 88 Comparison of measured and predicted CO2 concentrations

The agreement between measured and simulated CO_2 concentrations is good (please note the relatively narrow range on the y-axis) in particular for the 50% load case. The small difference of about 0.25 %vol that does exist in both cases is most likely due to a small difference in stoichiometry between the simulation and the actual operation of the boiler at the time of the measurements. At all measurement locations the burnout is almost completed and the CO_2 concentration is almost solely given by stoichiometry as is also indicated by the very limited variation with location.

Although the ability of CFD to predict CO quantitatively is questionable a comparison between measured and predicted values is shown in Figure 89 for the full load coal firing case.

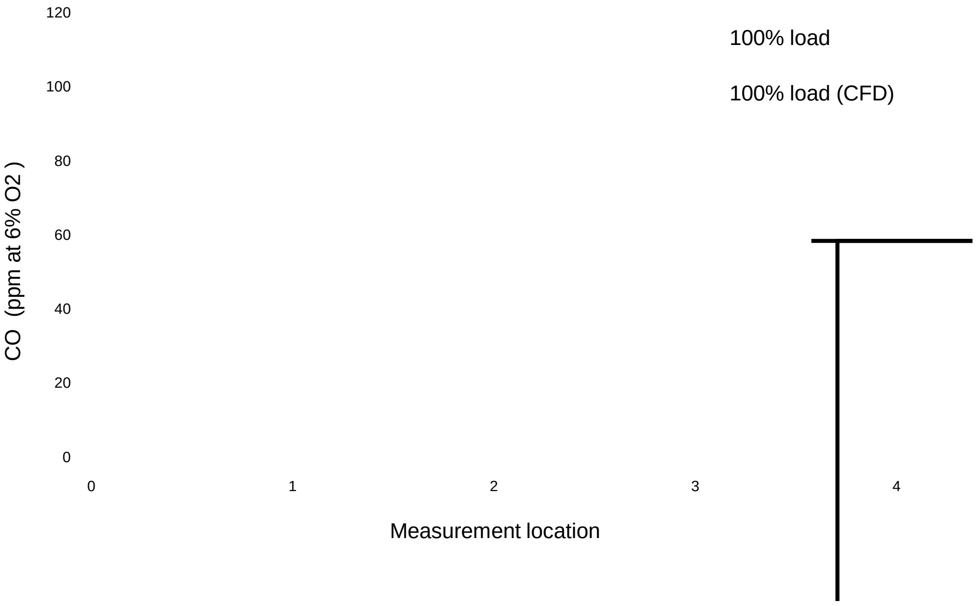

Figure 89 Comparison of measured and predicted CO concentrations

Given the uncertainty in both measurements and simulation, the agreement is strikingly good at the three measurement locations included. As an overall conclusion, the ability to predict the decrease from point 1 to point 2 is worth noticing. This gives some indication that the approximate location of the CO burnout region can be captured by the model.

4.2.4 Ash deposition rates

Local ash deposition rates were predicted based on the model framework described in Section 2.1.2 assuming the walls are clean i.e. there is not an existing deposit at the walls that contribute to the stickiness as particles arrive at the heating surfaces and the wall temperature was based on the steam data. The accumulation rates of solid particles (non-volatile ash species) were based on 427200 predicted particles trajectories. In addition, the straw potassium content was allowed to vaporize from the particles with a fraction corresponding to typical findings from chemical fractionation analyses. Figure 90 shows the local gas phase potassium mass fraction. The concentration is seen to attain its maximum close to the burner mouth were the high temperature levels causes the potassium to be released from the fuel particles.

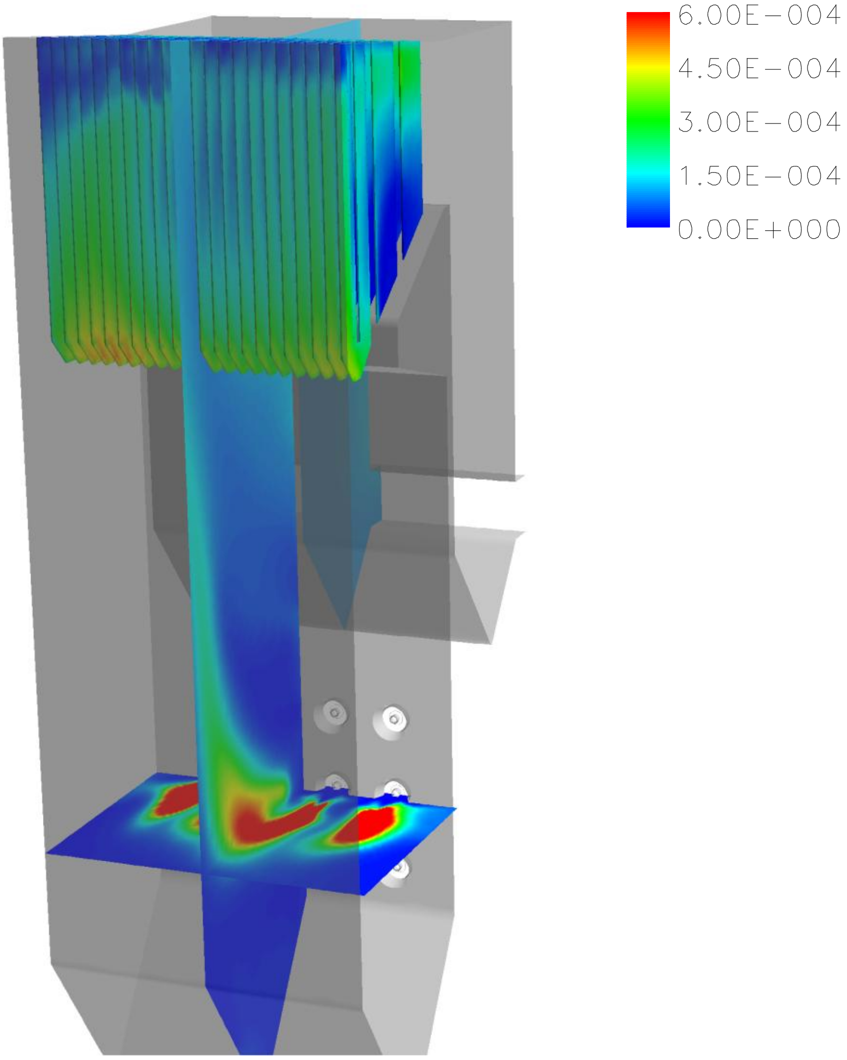

Figure 90 Gas phase potassium mass fraction

Based on the particle trajectory calculations, the contribution from inertial impaction to the local particle deposition rates was calculated. The highest rates are found at the furnace wall opposite the burners and at the lower part of the pendant super heater located in the furnace region. Figure 91 show the inertial impaction rates on the primary pendant super heater.

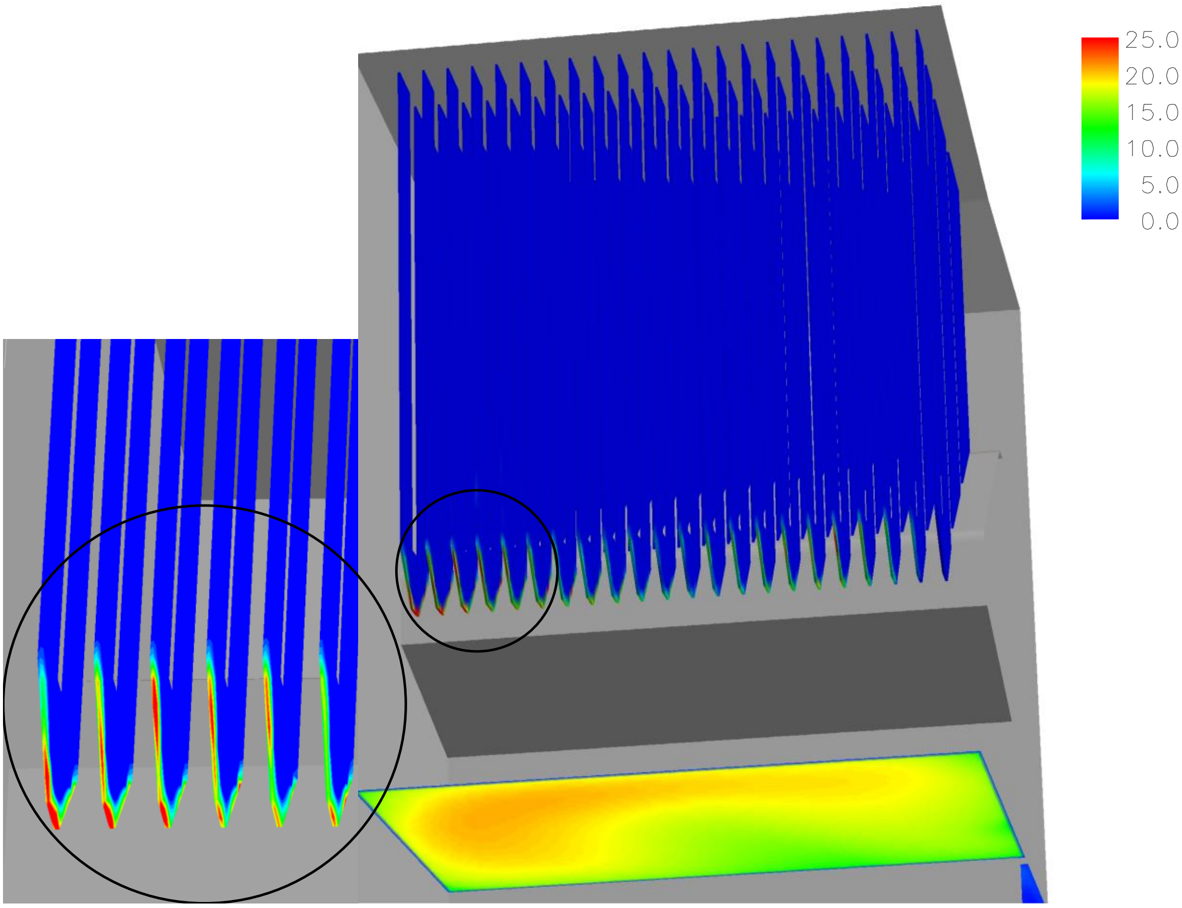

Figure 91 Local ash deposition rates due to inertial impaction [g/m2/s]

As expected, the inertial impaction onto the pendant super heater is highly localized in the bottom bend part perpendicular to the main flow direction. The particles follow as main flow path directed towards this region. When compared to inertial impaction rates predicted for grate fired boilers (Kær, Rosendahl and Baxter, 2006) these values are significantly higher due to the higher temperature and the fact that a significant portion of the ash in grate fired boilers is not entrained in the gas. Another interesting feature that can be seen from Figure 91 is the fact that the higher gas temperature (seen from the temperature cross-section) in one side of the furnace influences the stickiness of the ash particles causing more rapid deposit accumulation in this side of the furnace compared to the other.

The deposition rates resulting from turbulent and themophoretic deposition are shown in Figure 92 and Figure 93.

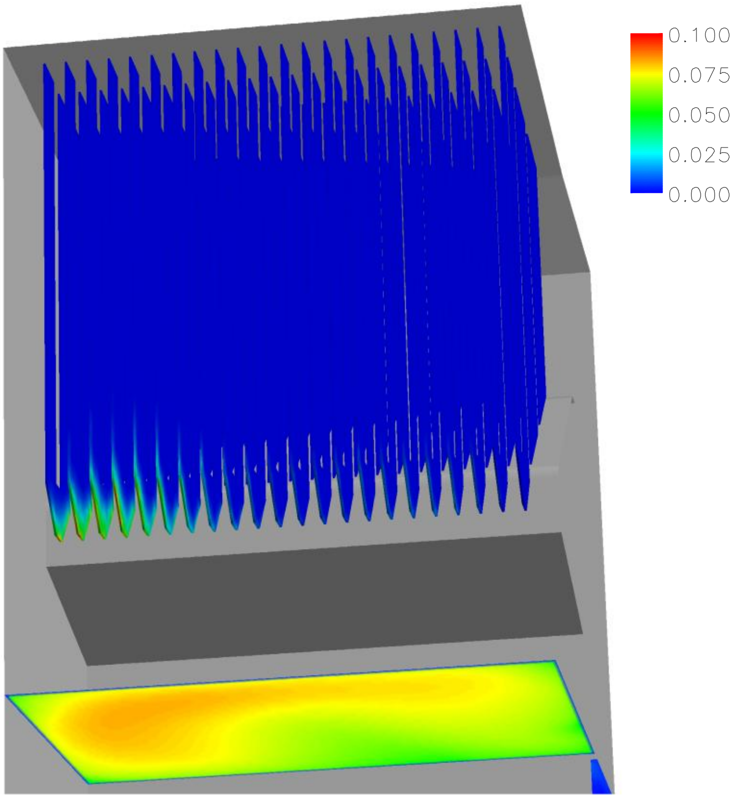

Figure 92 Turbulent impaction rates [g/m2/s]

In general, the deposition rates caused by mechanisms resulting from transport processes in the boundary layer are much slower than that of inertial impaction. The same influence from the gas phase temperature profile is seen from these predictions. It should also be noted that the deposition is not as localized on the bottom section of the super heater when compared to the inertial impaction rates. Although the deposition growth rate by the boundary layer mechanisms is relatively slow, over time it causes a sticky surface that contribute to the capture of impinging particles during the later stages of deposit build-up.

When compared to previous predictions for grate fired boilers (Kær, Rosendahl and Baxter, 2006) there is a very good correspondence - again taking into account that the entrained ash fraction in suspension fired boilers is larger.

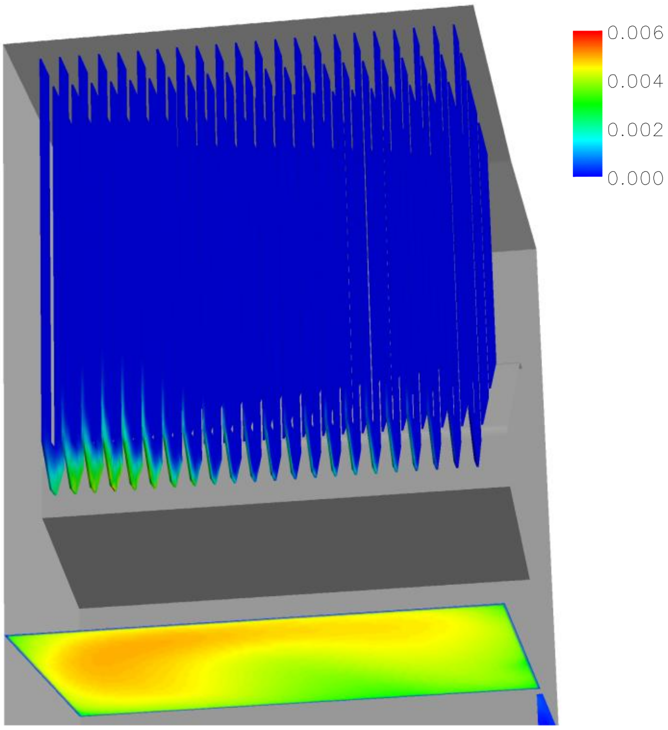

Figure 93 Thermophoretic deposition rates [g/m2/s]

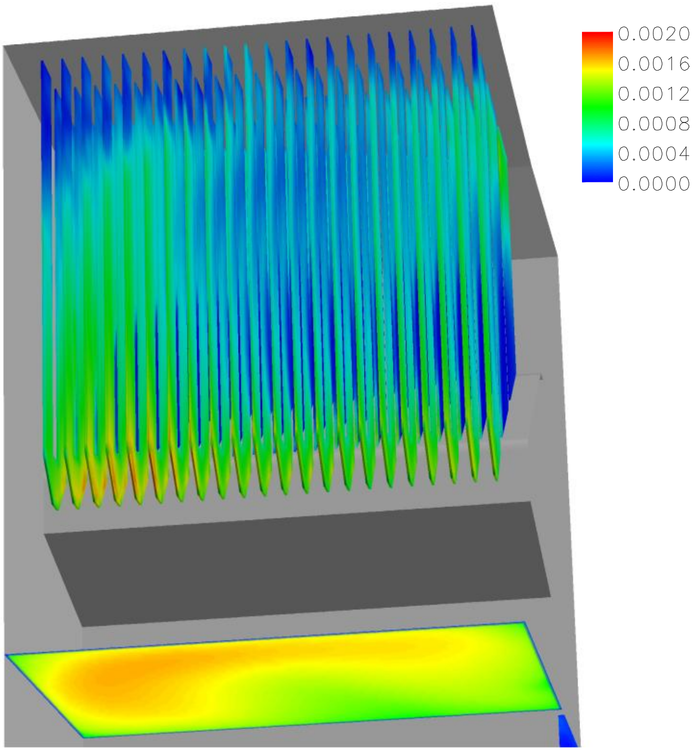

Figure 94 Deposition of vapor species released from the straw particles [g/m2/s]

The deposition of species released during combustion is shown in Figure 94 exemplified by potassium chloride. As for the rates in Figure 92 and Figure 93, the vapor deposition rate is very slow with a maximum of about 5-10 g/m2/h. Again, this is comparable to similar predictions made for grate fired boilers in the past (Kær, Rosendahl and Baxter, 2006). The fraction of potassium released to the gas phase in suspension fired boilers is expected to somewhat higher than in grate fired boilers as reactions in the fuel bed of grate fired boilers capture some of the released potassium. In relations to the discussion of the mechanisms of potassium capture it should be noted that reactions between the released potassium and other solid ash species in suspension is not accounted for. In particular the reaction with coal ash may be of some importance and the inclusion of this process in the models should be considered in future work.

4.2.5 Application to advanced plants

The original intention to apply the models developed in the course of this project to more advanced plants (e.g. Esbjerg Unit 3 or Skærbæk Unit 3) has been postponed and is now carried out in the ongoing PSO project 4881. The reason for this change in project objectives is primarily the late stage at which the models have become available. It has taken a considerable amount of time and effort to generate the experimental data upon which to base these models and likewise a substantial effort to implement these in a CFD framework.

5. Task 5: Design guidelines for low-NO_x burner operation when co-firing coal and straw

The following practical guidelines and one observation arise from the experimental and modeling work performed during this project**.**

5.1 Guidelines

1. As with dedicated coal burners, cofired burners exhibit a minimum NO_x emission as a function of swirl number, with this minimum commonly occurring near a swirl number of 1 (±½). This minimum is often more than 30% lower than the performance on either side of the minimum. Burners with dedicated biomass-coal streams should be readjusted to operate at this minimum.

2. Straw contains relatively large and dense particles that presumably originate from straw knees and that burn at much later residence times than the remainder of the straw or the coal. This creates an elongated flame with potential for particle impaction on walls during oxidation. Burners should be operated to avoid such impaction or other deleterious consequences from the large particles.

3. Biomass forms more NH_3 as an NO precursor than does coal, and NH_3 does not thermally decompose as rapidly as HCN at temperatures common to most boilers. Therefore, straw with significant nitrogen loading (most straw) should be fired in the center and coal in an annulus in a split-feed burner to minimize NH_3 conversion to NO and to maximize NH_3 reactions with coal-derived NO.

4. Cofiring straw with coal may decrease, increase, or not change overall NO emissions depending on relatively complex interactions of fuel, fluid dynamics, turbulent chemistry, and particle reactions. Generally, slight reduction should be possible when using low-N fuels.

5.2 Observation

1. Cofired (and pure coal) flames include large, sometimes dominant, regions of many small flamelets that burn intermittently, with oxygen and fuel-rich species such as CO occurring transiently nearly everywhere in the flame. This differs distinctly from a large flame with a fuel-rich core and a wrinkled interface with the oxidizer that is commonly imagined.

6. Bibliography

Albrecht, H. E., M. Borys, N. Damaschke, og C. Tropea. *Laser Doppler and Phase Doppler Measurement Techniques.* Springer Verlag, 2003.

Andersen, Karin Hedebo. "Co-firing Coal and Straw - In-situ Measurements at Studstrup Power Station Unit 1." Report, 1998.

Ballester, J., J. Barroso, L. M. Cerecedo, and R. Ichaso. "Comparative Study of Semi-industrial-scale Flames of Pulverized Coals and Biomass." *Combustion and Flame*, 2005: 204-215.

Baxter, L. "Personal Communication." 2002.

Berg, Steve. »Biomass Cofiring in Suspension Fired Power PLants.« PhD Dissertation (draft), 2006.

Bryden, K. M., and M. J. Hagge. *Fuel*, 2003: 1633-1644.

Bryden, K. M., K. W. Ragland, and C. J. Rutland. "Modeling thermally thick pyrolysis of wood." *Biomass & Bioenergy*, 2002: 41-53.

Damstedt, B., et al. "NOx Formation in an Independently Fed, Cofired, 140 KWth, Swirl Stabilized Burner." *Proceedings of the Combustion Institute*, 2005.

Dayton, D. "A Summary of NOx Emissions Reduction from Biomass Cofiring." NREL/TP-510-32260, National Renewable Energy Laboratory, 2002.

Dean, A. M., and J. W. Bozzelli. *"Combustion Chemistry of Nitrogen", in Gas-Phase Combustion Chemistry.* Edited by W. C. Gardiner. Springer Verlag, 2000.

Di Blasi, C. "Heat, momentum and mass transport through a shrinking biomass particle exposed to thermal radiation." *Chemical Engineering Science*, 1996: 1121-1132.

Hansen, L., Flemming J. Frandsen, Per G. Kristensen, Christian E. Nielsen, and Kim Dam-Johansen. "Gas Analyses and Alkali Measurements at MKS1 - Final Report." Report 9620, Dept. of Chemical Engineering, Tech. Univ. Denmark, 1996.

Kær, S. K., L. A. Rosendahl, and L. Baxter. "Towards a CFD-based Mechanistic Deposit Formation Model for Straw-fired Boilers." *Fuel*, 2006: 833-848.

Kær, S. K., L. Rosendahl, C. Yin, S. Berg, and H. Junker. "Co-firing Biomass and Coal - Progress in CFD Modelling Capabililties." *In: 30st International Technical Conference on Coal Utilization & Fuel Systems*, April 16-22, 2005.

Kilpinen, P., M. Hupa, M. Aho, and J Hämäläinen. *Download Area.* 2007. http://web.abo.fi/fak/ktf/cmc/research/r_schemes.html.

Larsen, E. "Halmtilsatsfyring i Naturgasfyret Kraftværkskedel." Report ELTRA-PSO 3149, 2004.

Leppalahti, J. L. "Formation of NH3 and HCN in Slow-heating-rate Inert Pyrolysis of Peat, Coal and Bark." *Fuel*, 1995: 1363-1368.

Lu, Hong. "Experimental and Modeling investigations of biomass particle combustion." Ph.D. dissertation, Brigham Young University, 2006.

Marschner, H. *Mineral Nutrition of Higher Plants.* Academic Press, Inc., 1990.

Næss, Leif, Susan Brown, Lars Erik Øi, and John Arild Svendsen. *Dynamisk Prosessmodellering.* 1989.

Nelson, P. F., A. N. Buchley, and M. D. Kelly. "Functional Forms of Nitrogen in Coals and the Release of Coal Nitrogen as NOx Precursors (HCN and NH3)." *Proceedings of the Combustion Institute*, 1992: 1259-1267.

Pershing, D. W., and J. O. L. Wendt. "Pulverized Coal Combustion: The Influence of Flame Temperature and Coal Composition on Thermal and Fuel NOx." *Proceedings of the Combustion Institute*, 1977: 389-399.

Pickett, Lyle M., Robert E. Jackson, and Dale R. Tree. "LDA Measurement in a Pulverized Coal Flame at Three Swirl Ratios." *Combustion Science and Technology*, 1999: 79-107.

Rosendahl, Lasse A., C. Yin, Søren Knudsen Kær, Klaus Friborg, and Peter Overgaard. "Physical Characterization of Biomass Fuels Prepared for Suspension Firing in Utility Boilers for CFD Modelling." *Biomass and Bioenergy*, 2007: 318-325.

Smith, G. P., et al. *gri_mech.* 2000. http://www.me.berkeley.edu/gri_mech/.

Tree, Dale R., and A. W. Clark. "Advanced Reburning Measurements of Temperature and Species in a Pulverized Coal Flame." *Fuel*, 2000: 1687-1695.

Walsh, P., A. Sayre, D. Loehden, D. Monroe, J. Beér, and A. Sarofim. "Deposition of Bituminous Coal Ash on an Isolated Heat Exchanger Tube: Effects of Coal Properties on Deposit Growth." *Progress in Energy and Combustion Science*, 1990: 327-345.

Widmann, J. F., S. R. Charagundla, and C. Presser. "Benchmark Experimental Database for Multiphase Combustion Model Input and Validation: Characterization of the Inlet Combustion Air." NISTIR 6370, National Institute of Standards and Technology, 1999.

Wu, Chunyang. "Fuel-NOx Formation During Low-grade Fuel Combustion in a Swirling-flow Burner." PhD dissertation, Brigham Young University, 2006.

Zhang, J., and S. Nieh. "Swirling, Reacting, Turbulent Gas-particle Flow in a Vortex Combustor." *Powder Technology*, 2000: 70-78.

A. Appendix A. Boundary Conditions for CFD Simulation of MKS Unit 1 during coal-straw co-firing.

Boundary conditions for the simulation of the coal-straw co-firing trials performed at the Studstrup Unit 1 power plant are determined based on control data from the test periods. Test conditions and trial dates are described in the report *“Cofiring Coal and Straw, In-Situ Measurements at Studstrup Power Station Unit 1”,* dated 07.01.1998, which has been prepared by Industrial Ph.D. Karin Hedebo Andersen. An overview of combinations of plant load and straw shares is given in the report (see Table A- 1 below):

Table A- 1. Experiment numbering for combustion trials at MKS1.

Load (% / MW_{th})	Straw share (thermal)		
	20 %	10 %	0 %
Coal 1: COCERR			
50% / 190 MW_{th}	1		7
75% / 285 MW_{th}	2	E3	6
100% / 380 MW_{th}	3 & 3B	4	5
100% / 380 MW_{th}	E2	(E3)	E1
Coal 2: SAKLEI	(Exp. 8 and 9 were not executed!)		
100% / 380 MW_{th}	9		8
Coal 2B: USILI2			
100% / 380 MW_{th}	9B		8B

Table A- 2. Test periods for the combustion trials.

Exp. no.	Load	Straw share	Week no./Year	Test Period
1	50 %	20 %	12/1996	18/3 13:30 – 20/3 13:30
2	75 %	20 %	15/1996	10/4 11:00 – 12/4 11:00
3	100 %	20 %	13/1996	26/3 13:30 – 29/3 13:30
3B	100 %	20 %	5/1997	
4	100 %	10 %	16/1996	
5	100 %	0 %	17&22/1996	22/4 06:00 – 23/4 18:00
6	75 %	0 %	19/1996	8/5 12:00 – 10/5 10:00
7	50 %	0 %	18/1996	29/4 20:00 – 3/5 12:00
8	100 %	0 %	20/1996	
8B	100 %	0 %	6/1997	
9B	100 %	20 %	6/1997	
E1	100 %	0 %	3/1997	
E2	100 %	20 %	4/1997	
E3	75 %	10 %	4/1997	

The periods quoted in column 5 in Table A- 2 are the periods during the testing weeks where the unit has been in stable operation at the indicated load for a substantial amount of time. Average data for these selected periods are used to determine boundary conditions suitable for steady state simulations. Only the experiments during 1996 (harvest of 1995) and co-firing at 0% and 20% share with Columbian coals (COCERR) has been considered for this work, i.e. experiments no.’s 1,2,3,5,6 and 7.

The available historic data are stored as 6 minute averages and include secondary air flows (for each individual burner) and coal mill shares of the total coal consumption. These data are useful in determining the actual load distribution during trials. These data do not facilitate determination of coal feed rates for individual burners just as straw shares are not available for the individual burner. Accordingly, an equal fuel share between the burners on a row is the only reasonable assumption. For this reason also, it would be unreasonable to apply the actual measured values for the combustion air on an individual burner resolution, and an equal distribution of air (on a row by row level) is therefore applied.

Full load steam production for MKS1 is 139 kg/s.
Burner data: Nominal/Max. burner load: 31.7 / 38.0 MW_{th}
Max. burner load at 20% straw share: 38.0 MW_{th} (equally distributed between coal and straw)

20% Straw Share

Table A- 3. Secondary air and Coal mill data for trials at 20% straw share.

	Unit	Exp. No. 1	Exp. No. 2	Exp. No. 3
Load	%	50	75	100
Steam production	Kg/s	72,1	103,4	135,4
Mill 10 share	%	0,0	0,0	35,2
Mill 20 share	%	49,9	42,7	29,9
Mill 30 share	%	50,1	57,3	34,9
Sec. Air Row 10	Nm^3/s	0,1	1,0	25,1
Sec. Air Row 20	Nm^3/s	28,4	28,9	26,5
Sec. Air Row 30	Nm^3/s	19,3	30,4	25,5

Table A- 3 shows that the top burner level (Row 10) has not been in operation at 50% and 75% load. At 50% load the coal is distributed evenly between rows 20 and 30 whereas the coal share at 75% load is increased more on row 30 because the maximum burner load is reached on row 20 due to the straw loading. The same tendency is seen at 100% load where rows 10 and 30 both receive a higher coal share than row 20 which, again, is at max. burner load.

Thermal loads for coal and straw are assumed to be a linear function of steam production, where 139 kg/s corresponds to a total thermal load of 380 MW_{th}. In all cases, it is assumed that the straw share is exactly (!) 20% of the total thermal load as there is no data on mass flow of straw into the boiler. The amount of coal is then determined as the remaining 80% of the thermal load, and this is then distributed between the burner rows according to the mill shares denoted in Table A- 3.

This approach yields the following distribution of coal and straw for the three experiments shown in Table A- 4 below:

Table A- 4. Thermal load of fuels per burner row for experiments 1, 2 and 3.

Experiment No.	1	2	3
Load:	50 %	75 %	100 %
Row 10 (coal)	0,0 MW_{th}	0,0 MW_{th}	104,0 MW_{th}
Row 20 (coal)	78,8 MW_{th}	96,4 MW_{th}	88,0 MW_{th}
Row 20 (straw)	39,4 MW_{th}	56,4 MW_{th}	74,0 MW_{th}
Row 30 (coal)	78,8 MW_{th}	129,6 MW_{th}	104,0 MW_{th}

0% Straw Share

Utilizing the same approach as for the 20% straw share data yields the boundary conditions for pure coal firing shown in Table A- 5 below:

Table A- 5. Secondary air and Coal mill data for trials during pure coal firing.

	Unit	Exp. No. 7	Exp. No. 6	Exp. No. 5
Load	%	50	75	100
Steam production	Kg/s	66,2	102,5	139,1
Mill 10 share	%	0,0	34,3	33,5
Mill 20 share	%	50,3	32,7	32,2
Mill 30 share	%	49,7	33,1	34,3
Sec. Air Row 10	Nm^3/s	1,1	22,3	26,3
Sec. Air Row 20	Nm^3/s	22,0	20,8	25,9
Sec. Air Row 30	Nm^3/s	21,7	21,4	28,2

This yields the following distribution of coal and straw for the three experiments shown in Table A- 6:

Table A- 6. Thermal load of fuels per burner row for experiments 7, 6 and 5.

Experiment No.	7	6	5
Load:	50 %	75 %	100 %
Row 10 (coal)	0,0 MW_{th}	96,0 MW_{th}	127,3 MW_{th}
Row 20 (coal)	91,0 MW_{th}	91,6 MW_{th}	122,4 MW_{th}
Row 20 (straw)	0,0 MW_{th}	0,0 MW_{th}	0,0 MW_{th}
Row 30 (coal)	90,0 MW_{th}	92,4 MW_{th}	130,3 MW_{th}